# Optimization Of Three-Terminal Perovskite/Silicon Tandem Module Energy Yield Simulations In Real-world Conditions

## Wenang Suprayogi

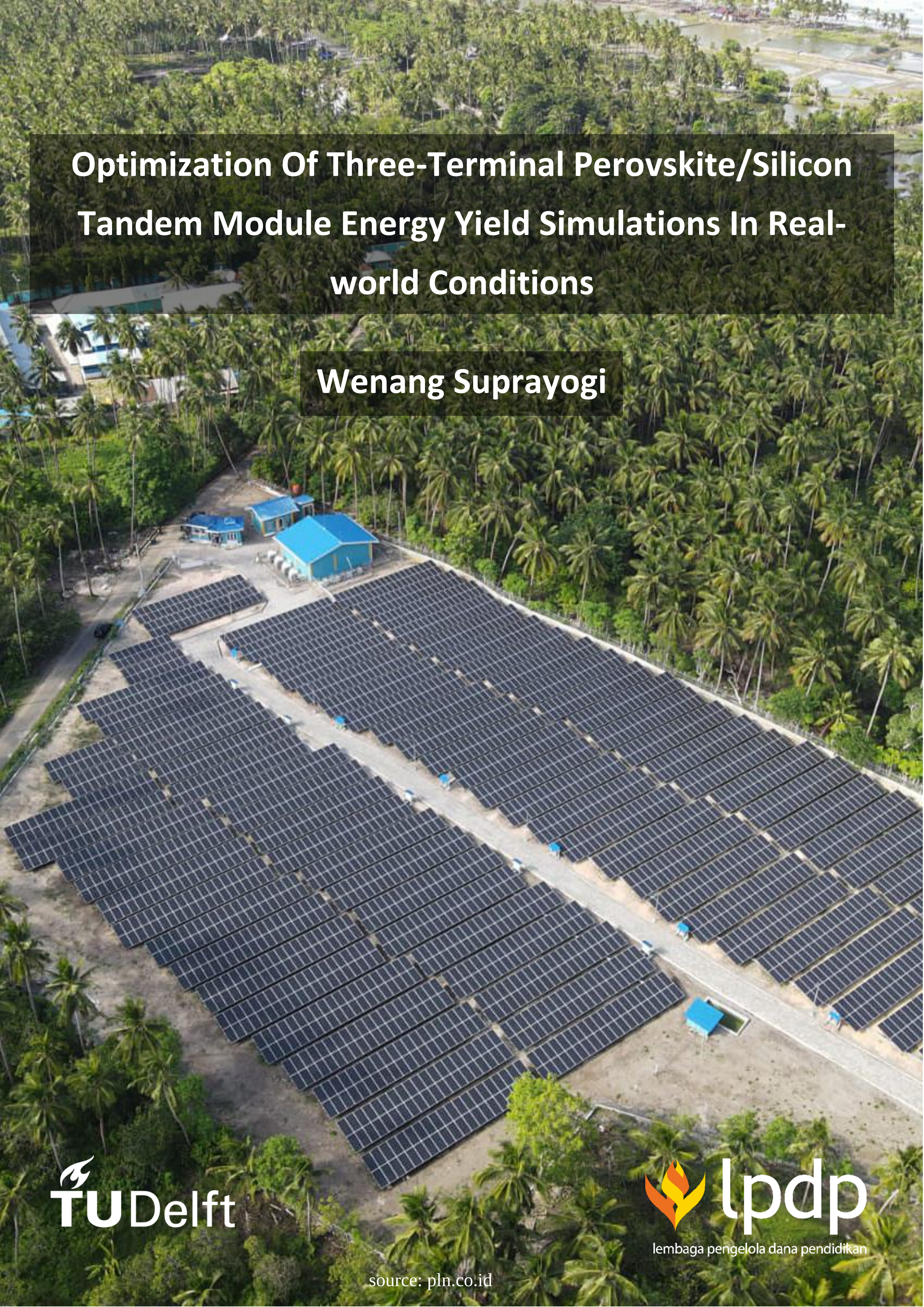

TU Delft

lpdp

lembaga pengelola dana pendidikan

source: pln.co.id

# OPTIMIZATION OF THREE-TERMINAL PEROVSKITE/SILICON TANDEM MODULE ENERGY YIELD SIMULATIONS IN REAL-WORLD CONDITIONS

by
**Wenang Suprayogi**
**5861918**

In partial fulfillment of the requirements for the degree of
**Master of Science**
Sustainable Energy Technology

**Supervisors:**
ir. Youri Blom
Dr. ir. Rudi Santbergen

To be defended publicly on Wednesday, August 28th, 2024, at 03.00 PM

**Thesis committee:**
Dr. Rene van Swaaij
Dr. ir. Rudi Santbergen
Dr. ir. Wenli Shi
ir. Youri Blom

**DELFT UNIVERSITY OF TECHNOLOGY**
**FACULTY OF ELECTRICAL ENGINEERING, MATHEMATICS, AND COMPUTER SCIENCE**
**SUSTAINABLE ENERGY TECHNOLOGY PROGRAMME**

# ABSTRACT

The transition to renewable energy sources is essential to mitigate the impacts of climate change, with solar energy playing a pivotal role in this shift. Photovoltaic (PV) technology. However, the traditional single-junction cells are reaching their theoretical efficiency, which currently stands at 29.43%. Through the use of tandem solar cells, this efficiency limit can be surpassed. The tandem cell is being researched further to increase the power conversion efficiency (PCE). However, the conventional two-terminal (2T) and four-terminal (4T) tandem configurations face challenges related to current matching and optical losses, respectively.

This project addresses these challenges by focusing on the development and optimization of a three-terminal (3T) perovskite/silicon tandem module. The research aims to enhance the energy yield of 3T module under real-world conditions by developing a comprehensive 3T model within the Photovoltaic Material and Devices (PVMD) Toolbox, bridging the gap between cell-level and module-level optimization, which has been underexplored in existing studies.

The first step involved the development of the 3T model, which incorporates independent connections for each sub-cell and utilizes an interdigitated back contact (IBC) on the bottom cell as the third terminal. The 3T model is developed and simulated in MATLAB to be validated, showing close alignment of IV curves compared to the existing literature. The 3T model is then used to simulate a 72-cell module to be validated with a widely used electrical simulator called LTspice. The validation of the developed MATLAB 3T model against LTSpice simulations demonstrated a close match, with an RMSE result of 0.02% errors, confirming the model's accuracy in predicting the IV curves and energy yield for various operating conditions.

The second phase of the research involved detailed comparisons between the performances of 2T and 3T modules, each consisting of 72 cells, under both standard test conditions (STC) and real-world conditions in Delft as a sample. The simulations revealed that the 3T module provides less annual energy yield than 2T. However, the 3T module performs better than 2T at handling spectral irradiance variations and current mismatch situations under real-world conditions. At a certain hour, 3T outperforms 2T by yielding 220.75 W compared to 219.1 W. The loss analysis confirms that the 3T module produces less mismatch loss under real conditions than the 2T module. The simulations at four different locations also show that 3T has a certain number of times when 3T yields more energy than 2T. This shows the potential of 3T to outperform 2T by optimizing the perovskite bandgap energy and thickness.

The optimization of the 3T module focused on adjusting the perovskite layer's bandgap energy and thickness. The optimal bandgap energy is identified as 1.64 eV, and the ideal thickness is 600 nm for 2T, yielding 588.79 kWh. On the other hand, 3T has optimal perovskite bandgap energy and thickness of 1.82 eV and 600 nm, respectively, yielding lower energy of 583.24 kWh. Then, the modules are expanded into 144-cell modules, which results in 3T consistently yielding around 0.4% to 0.8% more energy at its optimum perovskite bandgap energy and thickness at 4 location samples compared to the 2T. For example, at Delft, the 3T yields more annual energy of 1172 kWh than 2T of 1167 kWh. This is due to the reduced end loss produced by 3T at a larger number of cells in the module. These results show that the 3T outperforms 2T at its respective optimum perovskite bandgap energy and thickness at every location sample and at a larger number of cell modules. Although the current 3T technology with IBC is still expensive, it is expected to become competitively priced in the future. These findings highlight the importance of ongoing optimization and development of 3T modules to fully unlock their potential in various environmental conditions.

# ACKNOWLEDGEMENT

This thesis represents the results of my eight-month Thesis Project, with modelling conducted within the Photovoltaic Material and Devices (PVMD) research group at the Technical University of Delft. First and foremost, I express my deep gratitude to Allah SWT, the Almighty God, for granting me the strength, patience, and wisdom to complete this project. I also extend my heartfelt thanks to everyone in the PVMD group for fostering a supportive environment throughout my project.

I would like to thank my family and friends for their unwavering support over the past eight months and the entirety of my master's program. They celebrated my successes and stood by me during challenging times. These past two years have been memorable, and I am grateful to everyone who shared this journey with me. A special note of gratitude to my wife, Fadhila Nastiti, and my children, Razan Ibrahim Suprayogi and Arumaisha Tsabita Suprayogi, for their endless love and support. Thank you for believing in me, praying for me day and night, and standing by me despite the challenges.

I am especially indebted to my supervisors, ir. Youri Blom and Dr. ir. Rudi Santbergen. Their unwavering support, insightful knowledge, and constructive feedback were instrumental in the successful completion of this project. Their inspiration and motivation sustained me throughout this journey.

My sincere thanks also go to Dr. Rene van Swaaij and Dr. ir. Wenli Shi for being willing to be on my thesis committee.

Lastly, I express my deepest gratitude to the Ministry of Finance of the Republic of Indonesia, which provided me with the Indonesia Endowment Fund for Education (LPDP) scholarship. This scholarship covered all my expenses from the start of my master's degree until the day I return to Indonesia. Without their financial support, realizing my dream would not have been possible.

# TABLE OF CONTENT

# LIST OF TABLES

# LIST OF FIGURES

# NOMENCLATURE

**Parameters**

| | |
|---|---|
| $E$ | Energy (Wh) |
| $FF$ | fill factor |
| $I$ | Current (A) |
| $I_0$ | Saturation current (A) |
| $I_{bot}$ | Bottom cell current (A) |
| $I_{min}$ | Minimum current (A) |
| $I_{module}$ | Module current (A) |
| $I_{mpp}$ | Maximum power point current (A) |
| $I_{out}$ | Output current (A) |
| $I_{PV}\ or\ I_{ph}$ | Photogenerated current (A) |
| $I_{rpt}$ | Repeat unit current (A) |
| $I_{sc}$ | Short-circuit current (A) |
| $I_{top}$ | Top cell current (A) |
| $k$ | Boltzmann constant (C) |
| $m, n$ | VM rasio (integers) |
| $n$ | Ideality factor (-) |
| $N$ | Number of cells |
| $n_{cell}$ | Number of cell |
| $N_{cell}$ | Number of cell |
| $N_{rpt}$ | Number of repeating unit |
| $P$ | Power (W) |
| $P_{mpp,bot}$ | Maximum power point power of bot cell (W) |
| $P_{mpp,top}$ | Maximum power point power of top cell (W) |
| $P_{mismatch}$ | Mismatch losses power (W) |
| $P_{module}$ | Module power (W) |
| $P_{mpp}$ | Maximum power point power (W) |
| $P_{tandem}$ | Tandem power (W) |
| $q$ | Electron charge (J/K) |
| $R_{intercon}$ | Interconnection resistance (Ω) |
| $R_s$ | Series resistance (Ω) |
| $R_{sh}$ | Shunt resistance (Ω) |
| $RMSE$ | Root mean square error |
| $T$ | Temperature (K) |
| $V$ | Voltage (V) |
| $V_{out,bot}$ | Output voltage of the bottom cell (V) |
| $V_{out,top}$ | Output voltage of the top cell (V) |
| $V_{bot}$ | Bottom cell voltage (V) |
| $V_{module}$ | Module voltage (V) |

| | |
|---|---|
| $V_{mpp}$ | Maximum power point voltage (V) |
| $V_{oc}$ | Open-circuit voltage (V) |
| $V_{out}$ | Output voltage (V) |
| $V_{rpt}$ | Repeat unit voltage (V) |
| $V_T$ | Thermal voltage of diode (V) |
| $V_{top}$ | Top cell voltage (V) |
| $W$ | Lambert function |
| $X$ | Benchmark value [LTSpice] |
| $x$ | Predicted value [MATLAB] |

**Abbreviations**

| | |
|---|---|
| 2T | Two Terminal |
| 3T | Three Terminal |
| 4T | Four Terminal |
| AC | Alternating Current |
| AF2400 | Aclar Film 2400 |
| Ag | Argentum/Silver |
| AM | Air Mass |
| ASA | Advanced Semiconductor Analysis |
| a-Si(i) | Intrinsic Amorphous Silicon |
| a-Si(p) | P-doped Amorphous Silicon |
| AZO | Aluminum-Doped Zinc Oxide |
| C60 | Fullerene |
| c-Si | Crystalline Silicon |
| DC | Direct Current |
| ETL | Electron Transport Layer |
| EVA | Ethylene Vinyl Acetate |
| GlassARC | Anti-Reflective Coated Glass |
| HTL | Hole Transport Layer |
| ITO | Indium Tin Oxide |
| IV | Current-Voltage |
| IZO | Indium Zinc Oxide |
| JB | Junction Box |
| MPP | Maximum Power Point |
| MPPT | Maximum Power Point Tracking |
| n-SiOx-ncSi | N-doped Silicon Oxide with Nanocrystalline Silicon |
| PC | Personal Computer |
| PCE | Power Conversion Efficiency |
| PTAA | Poly(Triarylamine) |
| PV | Photovoltaic |
| PVMD | Photovoltaic Materials and Devices |

| | |
|---|---|
| R | R Contact |
| SBDART | Santa Barbara DISORT Atmospheric Radiative Transfer |
| SM | Sensitivity Map |
| SnO2 | Tin Oxide |
| STC | Standard Test Condition |
| T | T Contact |
| VM | Voltage -Matched |
| Z | Z Contact |

# CHAPTER I
# INTRODUCTION

The need for a significant energy transition from fossil fuels to renewable energy sources is necessary[1]. This is due to the countries's commitment to preventing climate change as a result of the Paris Agreement, which aims to limit global temperature increases to well below 2°C and pursue efforts to limit them to 1.5°C [2]. Solar energy is one of the renewable energy options in this energy transition. It is abundant, low-cost, and environmentally friendly [3]. Solar energy in the form of photovoltaic solar cells, has been identified as a promising renewable energy source with the potential to meet future energy demands [4].

To realize the objective, maximizing the efficiency of photovoltaic (PV) modules is crucial in order to minimize the quantity of required PV systems. The research on tandem solar cells is crucial due to the maximum theoretical efficiency of crystalline silicon (c-Si) solar cells, which currently stands at 29.43% [5]. Extensive research and development activities have been prompted by the stagnation of silicon-based solar cell efficiency, leading to the exploration of perovskite silicon-based tandem solar cells [6] [7] [8]. They have been proven to have a certified power conversion efficiency (PCE) of 32.5% [9] .Tandem cells, traditionally arranged in two-terminal (2T) and four-terminal (4T) configurations, encounter issues with current-matching and optical losses, respectively. The integration of three-terminal designs in tandem cells is a promising approach to address these challenges, which could result in a higher energy yield [10] [11] [12] [13].

Additionally, the performance of photovoltaic devices, particularly perovskite/silicon tandem solar cells, can be significantly affected by the differences between standard test conditions (STC) and real outdoor conditions. The ideal bandgap energy for perovskite in tandem cells may not necessarily be ideal under real conditions due to the interplay between temperature and bandgap energies [7]. This discrepancy between STC and real conditions is a critical consideration as STCs often do not accurately represent the real outdoor conditions experienced in most regions of the world[14]. Moreover, assessing the outdoor performance of perovskite/silicon tandems has been challenging due to limited reported tests and rare experimental data available for validating their performance under actual outdoor conditions [15]. Furthermore, many research studies aimed at optimizing the energy yield of 3T have predominantly been conducted at the cell level rather than at the module level. This focus on cell-level research means that potential improvements at the module level remain underexplored [16]. As a result, it is important to conduct research and optimize the performance of 3T solar modules to account for variations in environmental conditions, ensure their efficiency under different scenarios, and provide more comprehensive results at the module level.

This chapter explores the major topics researched in the literature study for this project. First, photovoltaic technology will be briefly introduced. This will be followed by explanations about the tandem technology needed to increase the solar cell's efficiency. Moreover, the PVMD Toolbox will be introduced, a tool that provides a detailed and accurate simulation of complex solar cell configurations [17]. Following this, the chapter will explain the specific knowledge gap that this project aims to address. Finally, it will outline the objectives of this thesis, providing a clear framework for the research conducted.

## 1.1 Photovoltaic technology

Photovoltaic technology involves converting sunlight into electricity using photovoltaic cells or solar panels. These cells are made of semiconductor materials that exhibit the photovoltaic effect, where the absorption of photons from sunlight generates an electric current. This section will provide a brief description of photovoltaic technology.

### 1.1.1 Solar energy

Solar energy is a form of renewable energy derived from the sun's radiation[18].It is abundant, low-cost, and environmentally friendly, making it an attractive option for addressing the world's energy needs[4] while reducing greenhouse gas emissions and dependence on fossil fuels[19]. The solar energy that reaches the upper atmosphere is approximately 1367 W/m$^2$, but by the time it reaches the earth's surface, the average energy that can be harnessed is about 300 W/m$^2$. Thus, the total power that can be generated on earth's land area is 45 PW [20]. In 2022, annual global primary energy consumption reached around 604 EJ [21], which is equal to 167.78 PWh. It means that if 45 PW is absorbed by 32.5% [9] of solar cell efficiency, it would take only around 0.13% of the land area to power the global demand. This shows that a tiny fraction of solar energy that hits the land area can serve the entire world's demand. The amount of solar energy received by the earth's surface can be seen in the AM1.5 spectrum [22] in Figure 1.1 below. It shows the spectral irradiance that can be yielded at every wavelength of light.

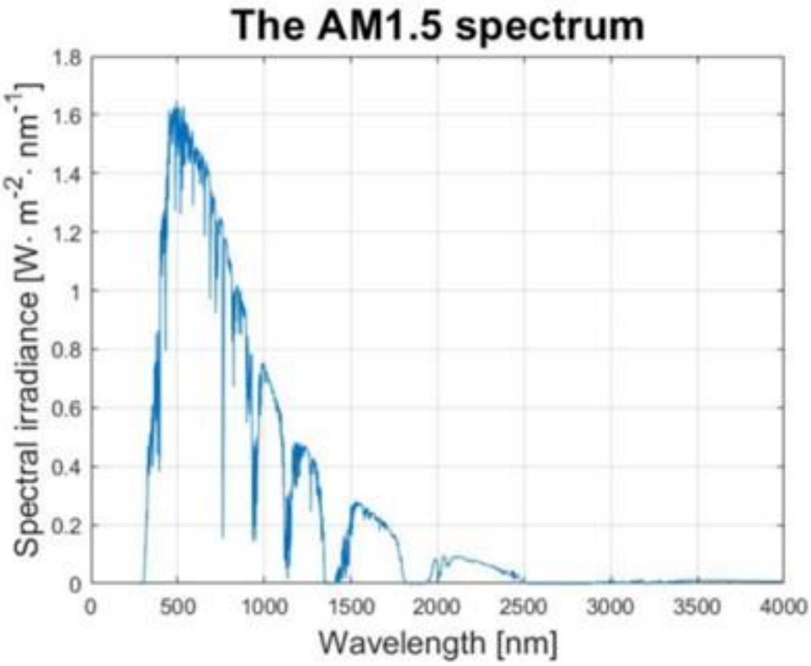

Figure 1.1 AM 1.5 Spectrum [23]

### 1.1.2 Working principle of solar cells

A solar cell is composed of p-type and n-type silicon semiconductors. P-type silicon is created by adding elements like boron, which have one less electron than silicon, creating "holes". N-type silicon contains atoms like phosphorus, which have an extra electron, providing free electrons within the silicon structure [24].

When these two layers are joined in a solar cell, the excess electrons in the n-type layer move to fill the holes in the p-type layer near their junction, forming a depletion zone. In this zone, the filled holes create negatively charged ions in the p-type region and positively charged ions in the n-type region. This separation of charges establishes an internal electric field that prevents further movement of electrons from the n-type to the p-type layer [24].

In a semiconductor, there are two key bands: the valence band, filled with electrons, and the conduction band, typically empty [25]. The bandgap energy (Eg) is the energy difference between these two bands [23]. The size of the bandgap determines how easily electrons can be excited from the valence to the conduction band, which is crucial for the material’s electrical and optical properties [24]. Figure 1.2 below express the bandgap energy and the photon from the sun or light source that excites the electron from the valence band to the conduction band through the bandgap energy.

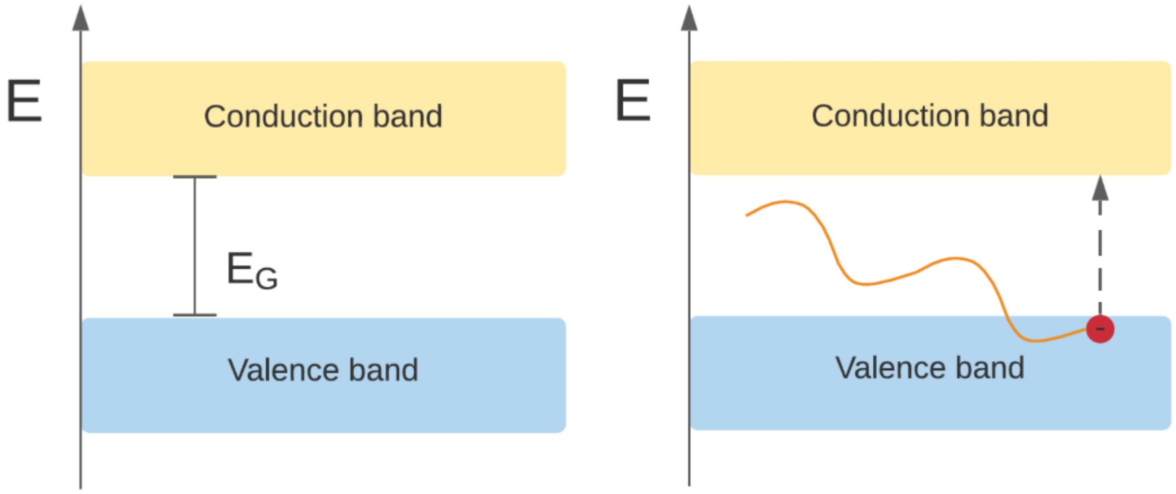

(a) Bandgap Energy (b) Electron excites to conduction band

Figure 1.2 The bandgap energy and the movement of the electron [23]

When solar cells are exposed to sunlight (photons), electron-hole pairs are created [25]. If the energy from the photon is higher than the energy bandgap, the electron will move to the conduction band as shown in Figure 1.2b, leaving a hole behind in the valence band. In the presence of an electric field, this movement results in electrons being pushed toward the n-type layer and holes toward the p-type layer. By connecting these layers with a metallic wire, electrons are able to travel from the n-type to the p-type layer across the depletion zone and then flow through the wire back to the n-type layer, thus generating an electrical current [26].

## 1.2 The IV curve of solar cell

The current-voltage (IV) curve of a solar cell is a critical characteristic that describes the electrical behavior and performance of the solar cell [27]. It illustrates the relationship between the generated current and the voltage of the solar cell across the terminals of the solar cell. The generated current is measured from different voltages; hence, the power of each point can be determined. Therefore, the maximum power ($P_{mpp}$) can also be obtained along with the maximum current ($I_{mpp}$), maximum voltage ($V_{mpp}$) and fill factor ($FF$). The IV curve and PV curve can be seen in Figure 1.3 below.

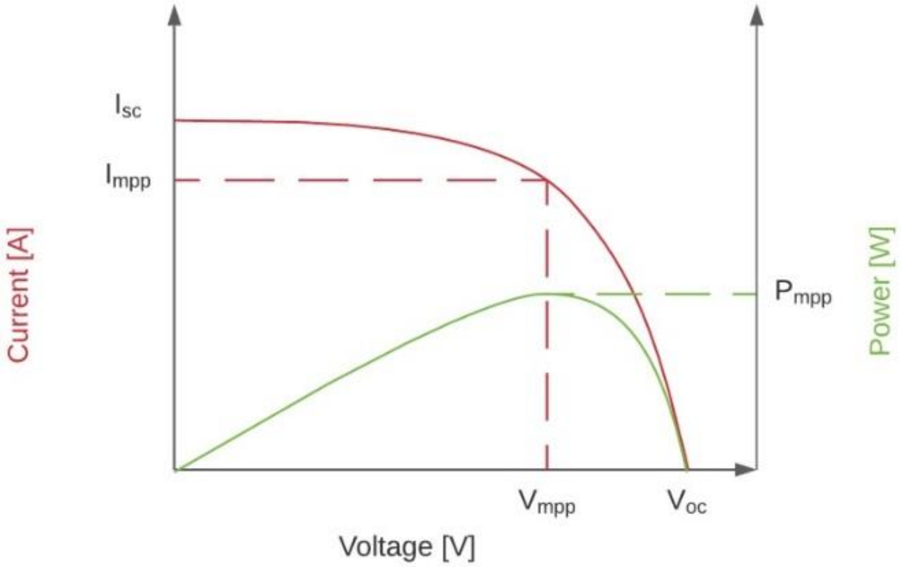

Figure 1.3 IV Curve and PV Curve of Solar Cell

Several essential parameters characterize the IV curve of a solar cell. The first is the short-circuit current ($I_{sc}$), which is the current flowing when the voltage across the solar cell is zero. Next is the open-circuit voltage ($V_{oc}$), defined as the voltage across the cell when there is no current output. Then, the maximum power point ($P_{mpp}$) represents the highest power output the solar cell can achieve. Associated with $P_{mpp}$ are the maximum power point voltage ($V_{mpp}$) and current ($I_{mpp}$), which are the voltage and current values at which this maximum power is obtained. Lastly, the fill factor ($FF$) is a crucial parameter that indicates the ratio of the maximum power to the product of $I_{sc}$ and $V_{oc}$ [28].The fill factor can be calculated using Equation 1.1 below:

$$FF = \frac{V_{mpp} \times I_{mpp}}{V_{oc} \times I_{sc}} \tag{1.1}$$

## 1.3 The equivalent circuit of solar cell

It is commonly understood that ideal solar cells can be represented as a combination of a current source and a diode in parallel [29]. This basic model is enhanced by adding resistors to simulate losses and, in certain cases, extra diodes to account for additional effects. The most widely accepted equivalent circuit for a solar cell or panel, as depicted in Figure 1.4, comprises a current source, a single diode, and two resistors (one arranged in series and another in parallel) to represent the complete behavior of the cell.

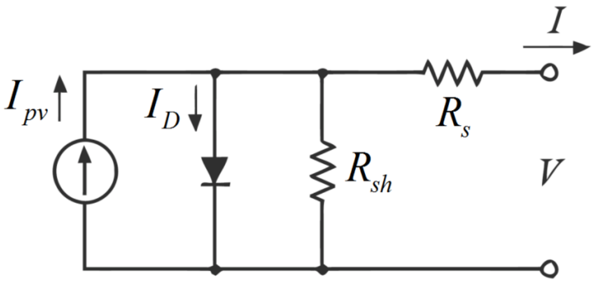

Figure 1.4 Equivalent circuit of the solar cell [29]

The circuit model's current-voltage (IV) characteristics, which include a diode and two resistors, as shown in Figure 1.4, are described by Equation 1.2 below.

$$I = I_{pv} - I_0 \cdot \left( e^{\frac{(V+I\cdot R_S)}{n\cdot V_T}} - 1 \right) - \frac{V + I \cdot R_s}{R_{sh}} \tag{1.2}$$

Equation 1.2 shows a clear formula for calculating the current that can be extracted. However, there are parameters that are unknown, which are:

- Photo Generated Current ($I_{pv}$): This represents the current generated by the solar cell due to sunlight. It represents the total generated electron-hole pairs within a solar cell.
- Saturation Current ($I_0$): The diode's reverse saturation current accounts for the recombination losses within the solar cell.
- Ideality Factor ($n$): This parameter, also characteristic of the diode, indicates the dominant recombination mechanism.
- Series Resistance ($R_s$): This represents the ohmic losses in the bulk material and contacts of the solar cell. It accounts for losses due to the resistance of the cell's material and connections. In an ideal solar cell, it has 0 value.
- Shunt Resistance ($R_{sh}$): This parameter represents the losses due to leakage currents through the cell. Ideally, the $R_{sh}$ value would be infinite, implying no leakage

While $V_T$, the thermal voltage of the diode, is a known parameter calculated based on the electron charge ($q$), the Boltzmann constant ($k$), the number of cells in series ($N$), and the temperature ($T$) shown in Equation 1.3 [29].

$$V_T = N \frac{k \cdot T}{q} \tag{1.3}$$

## 1.4 Tandem cell technology

Tandem solar cell technology combines different types of solar cells, such as silicon and perovskite cells, to create multi-junction devices with the potential to achieve higher power conversion efficiencies. Combining silicon solar cells with metal halide perovskite cells has shown promise in surpassing the efficiency limits of single cells [30]. This approach is particularly attractive due to its potential to achieve power conversion efficiencies above 30% at reasonable costs [31]. Additionally, bifacial monolithic perovskite/silicon tandem solar cells have been explored to increase performance by exploiting albedo, the diffuse reflected light from the environment [15].

### 1.4.1 Principle of tandem solar cells

The principle of a tandem solar cell involves integrating multiple absorber layers with carefully determined bandgaps to minimize intrinsic losses and achieve higher conversion efficiency compared to single-junction solar cells [32]. In a tandem solar cell, two distinct materials featuring varying bandgap energies are stacked, allowing each layer to capture different light spectrums. The material with the larger bandgap is positioned above to absorb high-energy photons. Below, the material with the smaller bandgap captures lower-energy photons that the upper layer cannot absorb. This design enhances the efficiency of tandem solar cells compared to conventional ones, as they can convert more energy from high-energy photons into electricity. Figure 1.5 below is the comparison of usable energy between a single junction cell and a tandem cell.

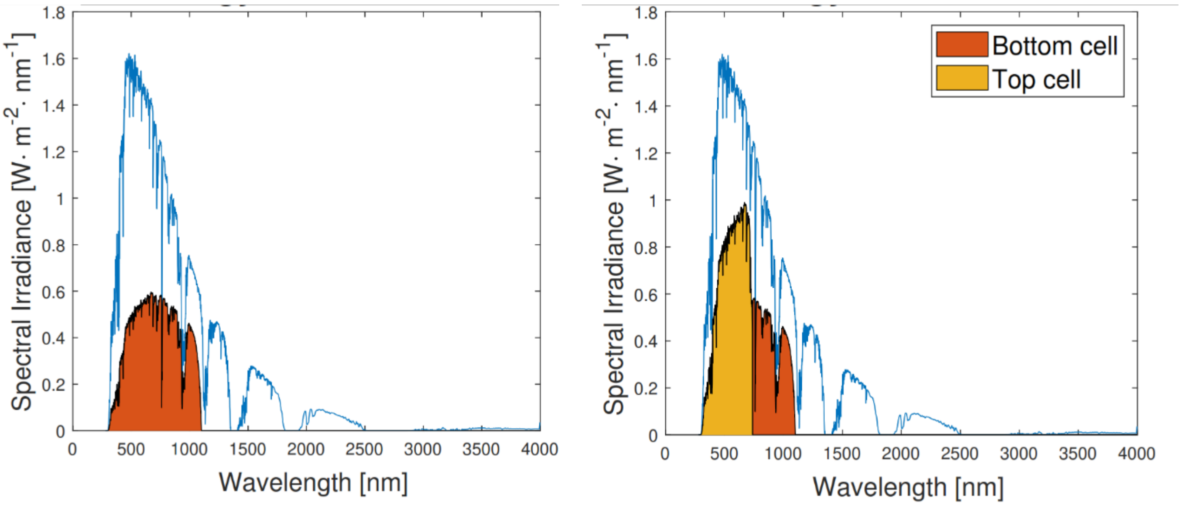

(a) Single junction cell

(b) Tandem Cell

Figure 1.5 Usable energy of different solar cell technologies [23]

### 1.4.2 Tandem cell configurations

Perovskite-silicon tandem solar cells have garnered significant attention in the past decade due to the rapid growth of perovskite photovoltaic (PV) technology. These tandem cells have demonstrated a certified power conversion efficiency (PCE) of 32.5% [9]. Despite notable advancements, the primary challenges associated with perovskite technology remain stability and scalability [33]. Researchers have extensively investigated two-terminal (2T) tandem designs, as well as four-terminal (4T) designs, aiming to address these challenges and enhance the overall performance of perovskite-silicon tandem solar cells [6], [31], [34], [35].

In the two-terminal (2T) configuration, two solar cells are integrally stacked and connected in series, as depicted in Figure 4a [36]. This design's power conversion efficiency (PCE) reaches its peak when the currents in both subcells are equal at the maximum power point. However, in actual operating conditions, the varying spectral composition of sunlight and changes in the angle at which light strikes the cells lead to substantial fluctuations in the photocurrent generation in each subcell. This results in considerable losses due to the current mismatch [13]. The 2T design is illustrated in Figure 1.6a.

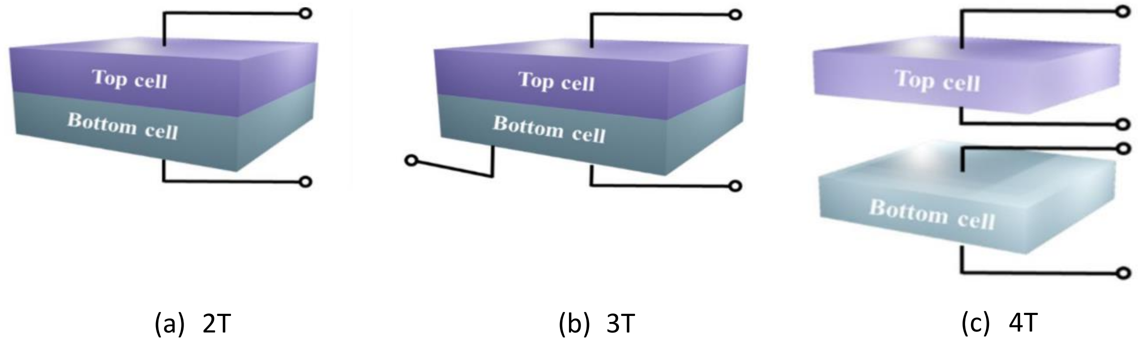

(a) 2T (b) 3T (c) 4T

Figure 1.6 The different configurations of tandem cells

On the other hand, the four-terminal (4T) configuration features two mechanically layered cells that function independently at their respective maximum power points (MPP) [36]. This design is not affected by the current mismatch issues seen in the 2T configuration. However, thick transparent electrodes are required for effective charge carrier extraction from both the upper and lower cells, minimizing ohmic losses. Additionally, a spacer layer is necessary to separate the two subcells. Unfortunately, these added layers cause significant losses due to absorption and reflection, as shown in Figure 1.6c.

In addition to the 2T and 4T configurations, a third double-junction tandem configuration, known as the three-terminal (3T) configuration, shown in Figure 1.6b, has recently been studied intensively [37]. A 3T solar tandem cell consists of two sub-cells with different semiconductor materials and bandgaps stacked together and connected via three electrical terminals. This design allows the top and bottom cells to function independently. When photons are absorbed, electron-hole pairs are generated in each sub-cell [13]. In the top subcell, separated electrons move towards its n-type layer and holes towards the p-type layer. These charges are collected by the electrodes connected to this subcell. Similarly, electrons and holes are separated in the bottom subcell and move toward their respective n-type and p-type layers. A detailed explanation of the dynamics of the electron and holes will be presented in Subsection 2.1 3T Configuration.

The analysis of the different tandem solar cell configurations (2T, 4T, and 3T) reveals distinct advantages and challenges for each design. The 2T configuration, while achieving optimal PCE under ideal conditions, suffers from significant power losses due to current mismatch caused by varying sunlight conditions. The 4T configuration eliminates current mismatch issues by allowing each subcell to operate independently at its maximum power point. However, it introduces losses due to the need for thick transparent electrodes and spacer layers, which cause absorption and reflection. The 3T configuration, emerging as a promising alternative, also enables independent operation of the subcells, thereby reducing current mismatch losses. It strikes a balance by potentially offering fewer additional losses compared to the 4T design because it does not require thick transparent electrodes. In summary, the 3T configuration is a promising alternative to overcome the disadvantages of the 2T and 4T configurations [13].

## 1.5 The PVMD Toolbox

The Photovoltaic Material and Devices (PVMD) group at Delft University of Technology has developed a PVMD Toolbox that can simulate the energy yield of photovoltaic technologies at a given location. It can be used to simulate the energy yield of different photovoltaic technologies, from the cell to the system level. This toolbox is always updated due to continuous development by researchers in this department [17].

### 1.5.1 PVMD Toolbox structure

The PVMD toolbox is organized in self-consistent models that simulate the various energy conversion steps, from calculating incident irradiance to the final AC yield. The toolbox has 9 simulation steps to simulate solar cell technology. However, in this study, only 5 simulation steps are used, including cell, module, weather, temperature, and electric.

**Cell simulation**

The optical properties data that are used in this simulation are obtained from GenPro 4 or other measurement data [38]. GenPro4 is an advanced optical model combining wave and ray optics to analyze light interaction with cell technologies. It views cells as 1D multilayer structures, using complex refractive indices ($n + ik$) and layer thickness ($d$) to compute reflectance ($R$), absorptance ($A$), and transmittance ($T$) for each layer and the overall cell [39]. The model factors in light interference and scattering on various surfaces, with calculations for reflectance and transmittance depending on wavelength ($\lambda$) and angle ($\alpha$), and absorption (A).

**Module simulation**

The toolbox simulates the module's mounting conditions and surroundings, assuming infinite boundary conditions and a free horizon, as mentioned in [38]. Users input cell geometrical properties, number of cells in rows and columns, azimuth, tilt angle, and height above ground. Customizable albedo reflects the environment. Upon setting these parameters, the toolbox visualizes a PV module within a larger plant, creating a hemisphere above it for computing the Sensitivity Map (SM). This map visually represents how the surface responds to incoming light by showing the ratio of absorbed to reflected light for each solid angle in the skydome. The most time-intensive part of the simulation is creating these sensitivity maps.

To establish the SM, the LUX software uses forward Monte Carlo ray tracing, dividing the skydome into 160 triangular segments, each representing a different light direction. Sensitivity is calculated by ray-tracing simulations projecting light from these directions. There is also a backward ray tracer, which models sunlight paths as they interact with urban surfaces, using irradiance models to decompose and combine irradiance components (direct, diffuse, and reflected) [40]. The software also computes average cell sensitivity. While individual cell sensitivity computation is more accurate, it significantly increases computational time.

### Weather simulation

The weather dataset from Meteonorm at the selected location is used as input to this simulation step. Using the input data, the Perez model [41] calculates the distribution of sky luminance across sky elements at each specific time point. If a skyline profile of the location is available, the model can simulate the impact of nearby objects; otherwise, it assumes an unobstructed horizon. The toolbox then utilizes the SMARTS model to add the spectral details of the incoming irradiance and photon flux. The toolbox has also recently integrated with Santa Barbara DISORT Atmospheric Radiative Transfer (SBDART) [42]. It considers aerosol properties, cloud optical thickness, and solar zenith angle to model the radiative transfer in the atmosphere [43], making the real outdoor conditions more accurate. The model has been validated against ground station observations and satellite-based measurements, demonstrating its reliability in simulating surface solar radiation patterns and corresponding radiative effects [44]. By integrating the sky map with the sensitivity map, the toolbox computes the absorbed irradiance $G_{mod}$ ($n_{cell}$, $t$) and the photocurrent $I_{jnc}$ ($n_{cell}$, $t$) produced at each cell and the entire module for any selected time period.

### Thermal simulation

The toolbox uses Fuentes' fluid dynamics model to calculate cell temperatures ($T(n_{cell}, t)$) at any time [45]. This model determines module temperature by balancing energy interactions with the environment, considering solar irradiance, air convection on both sides of the module, convection with the mounting structure, and radiative heat exchange with the sky. Inputs include solar irradiance, ambient and sky temperatures, wind speed, mounting characteristics, and module emissivity. The model iteratively resolves this balance due to the temperature-dependent nature of these factors. Its mathematical foundation, based on non-empirical parameters, allows for analyzing the impact of temperature-sensitive properties on module temperature [17].

**Electrical simulation**

The primary focus of this study is on the simulation, which provides IV curves and calculates the energy yield over a specific period of time. This toolbox employs a calibrated lumped-element model (CLEM) for simulating module interconnections with bypass diodes, efficiently generating IV curves hourly for a year. It calculates time-resolved IV curves for each cell using the Lambert W function, which can process up to 100,000 curves per minute. Inputs include cell-generated currents, cell temperature, temperature-illumination-dependent parameters from the one-diode model, chosen electrical configuration, and the time period. To streamline the year-long simulation, it categorizes operating conditions into discrete temperature and current steps, significantly reducing the number of simulations [17]. This approach allows a 60-cell module's annual simulation to be completed in about 2 minutes on a standard desktop PC, reducing total IV curves by 86%. However, it slightly overestimates annual module yield by approximately 0.23% due to reduced current mismatch losses, indicating a balance between simulation speed and precision, with larger step sizes further reducing mismatch losses.

These simulations are done using different models in the existing PVMD Toolbox. Figure 1.7 shows the overview and the interaction between the models to run this toolbox.

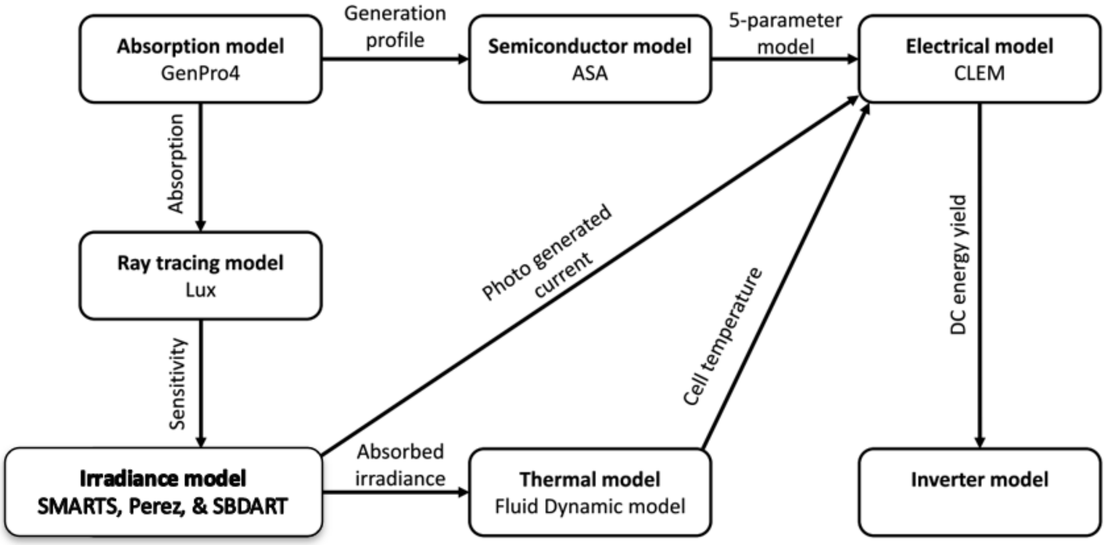

Figure 1.7 PVMD Toolbox models' overview

### 1.5.2 PVMD Toolbox limitation

The PVMD toolbox is a valuable resource for modeling photovoltaics from the cell level to the system level, offering both 2-terminal and 4-terminal models in the electrical simulation. However, a limitation of the toolbox is the absence of a developed and validated 3T model. This limitation restricts the toolbox's ability to accurately represent and analyze certain types of photovoltaic systems, such as multi-junction solar cells or tandem solar cells, which require a developed 3T model for comprehensive characterization. Therefore, the absence of this developed model in the PVMD toolbox hinders its applicability to a wide range of advanced photovoltaic technologies and limits its effectiveness in providing comprehensive modeling solutions for such systems.

## 1.6 Research gap and thesis objectives

This study aims to identify and resolve a specific gap in existing knowledge, as has been the case with all scientific investigations. This part will address this knowledge gap and then describe the thesis's objectives.

### 1.6.1 Research gap – motivation

This study is significant as it aims to fill a crucial research gap in the current PVMD Toolbox, particularly in the context of optimizing the energy yield of 3T solar modules. While the toolbox already contains basic models for 3T modules, these models require substantial developments and validation to accurately simulate and optimize realistic 3T tandem cell or module. The lack of detailed literature data on the energy yield of 3T modules in existing academic studies is a clear indication of this gap. Moreover, most research studies have focused on optimizing the energy yield of 3T at the cell level, neglecting the module level. By integrating a developed 3T model into the toolbox, researchers will be equipped to accurately optimize and analyze the behavior of the 3T module, thereby enhancing our understanding of its operational characteristics, contributing to the literature, and facilitating the development of more efficient and cost-effective solar energy solutions.

The motivation behind this research is comprehensive, with three distinct aspects driving the study. First, the research aims to enhance the capabilities of the PVMD toolbox. Second, it seeks to optimize the energy yield of the 3T configuration in the perovskite silicon tandem module. Third, it aims to contribute more data to the literature regarding 3T modules. By modeling the optimal 3T configuration PV modules, the research seeks to gain deeper insights into their performance and energy yield, thereby contributing to the advancement of PV technologies.

### 1.6.2 Thesis objectives

The main objective of this thesis is to optimize the energy yield of the 3T perovskite/c-Si tandem module by developing and simulating the 3T model using MATLAB, which will be integrated into the PVMD Toolbox. This thesis, therefore, has the primary research objective:

**Optimization of three-terminal perovskite/silicon tandem module energy yield simulations in real-world conditions**

Three sub-objectives have been identified to achieve the main objective, serving as essential steps towards the final goal. The following sub-objectives can be explained to reach the final goal.

**Sub-objective 1: Implement and validate the developed three-terminal (3T) model**

This step is crucial for accurately simulating and understanding the behavior of an advanced photovoltaic system, in this case, a 3T module. Validation is needed to ensure that the 3T model has been successfully developed, so it can be implemented in the existing PVMD Toolbox. By validating the developed model with existing literature and actual electrical behavior, the model is guaranteed to get accurate results.

**Sub-objective 2: Analyze and compare the performance of the three-terminal (3T) module with the two-terminal (2T) module**

Evaluate the performance of the 3-terminal (3T) module compared to the 2-terminal (2T) module in the PVMD Toolbox using the newly developed 3T model and the existing 2T model. The 2T and 3T tandem cells, which will be expanded to form 72-cell 2T and 3T modules, have optimized 2T parameters with 1.68 eV bandgap energy and 575 nm thickness for the perovskite layer. This involves conducting simulations and analyses to identify differences in power output, efficiency under varying irradiance conditions, and overall energy yield. The goal is to determine each module's strengths and weaknesses and highlight which module may offer superior performance. Then, if the 3T module produces inferior performance, the optimization will be conducted to optimize its output.

**Sub-objective 3: Determine the parameters that optimize the energy yield of the three-terminal (3T) module**

Identify the specific parameters that maximize the energy yield of the three-terminal (3T) perovskite-silicon tandem module using the newly developed 3T model. In this study, the parameters are perovskite bandgap energies and thicknesses, which will be optimized through simulations and analyses to enhance the module's performance and efficiency under various conditions. The number of cells will also be expanded from 72 cells to 144 cells to analyze the energy yields of both 2T and 3T modules. Finally, the energy yield of these modules will be compared to determine the best specifications of the 3T module, which will outperform the 2T module.

## 1.7 Thesis outline

This thesis report is structured into five chapters, each addressing specific aspects and objectives of the study. Chapter 2 explains the development of the 3T model, which aims to address Sub-objective 1: Implement and validate the developed three-terminal (3T) model. Chapter 3 focused on the performance comparison of the 2T and 3T modules, which will be discussed to reach Sub-objective 2: Analyze and compare the performance of the three-terminal (3T) module with the two-terminal (2T) module. Chapter 4 focuses on optimizing the top subcell parameters to answer Sub-objective 3: Determine the parameters that optimize the energy yield of the three-terminal (3T) module. Finally, Chapter 5 concludes the report by revisiting and addressing the sub-objectives posed at the beginning of the thesis. This final chapter summarizes the key findings and provides recommendations for future research in this domain, suggesting potential areas for further study and exploration based on the insights gained from the current research.

# CHAPTER 2

# DEVELOPMENT OF A COMPREHENSIVE 3T TERMINAL MODEL FOR PVMD TOOLBOX

This chapter addresses the initial Sub-Objective 1: Implement and validate the developed three-terminal (3T) model. This is done by replacing the existing 3T model with the newly developed 3T model in the PVMD Toolbox to simulate tandem cells' IV curves and energy yields. Before diving into the outcomes of the IV curves and energy yield simulation of the 3T model, examining the process behind its integration is essential, as this sets the stage for understanding both outcomes' metrics. Further, the developed 3T model will be validated with existing literature, as well as a widely used electrical circuit simulator called LTSpice.

The chapter begins by detailing the theory of 3T configuration. The theory then calculates and generates the IV curves and the energy yield. Furthermore, the IV curves and energy yield results of the developed 3T model are detailed. The existing IV curves and energy yield formula are detailed in Appendix A.1. Finally, the validations of the developed model will be detailed. real application. In the end, the conclusion summarizes the results of this chapter's discussions.

## 2.1 3T configuration

In this study project, the 3T tandem configuration involves an independent connection for each sub-cell, with the addition of an interdigitated back contact (IBC) on the bottom cell as the third terminal. This setup allows each sub-cell to operate independently and does not require additional ITO layers, thereby mitigating the current matching and optical loss issues typically seen in 2T and 4T configurations, respectively. This configuration will be explained and explored in the subsections.

### 2.1.1 3T tandem cell

The 3T tandem cell is a complex configuration that needs to be explained thoroughly to be understood. This innovative design integrates a perovskite top cell with an IBC at the bottom cell. The schematic representation of the 3T tandem cell is shown by Figure 2.1 below.

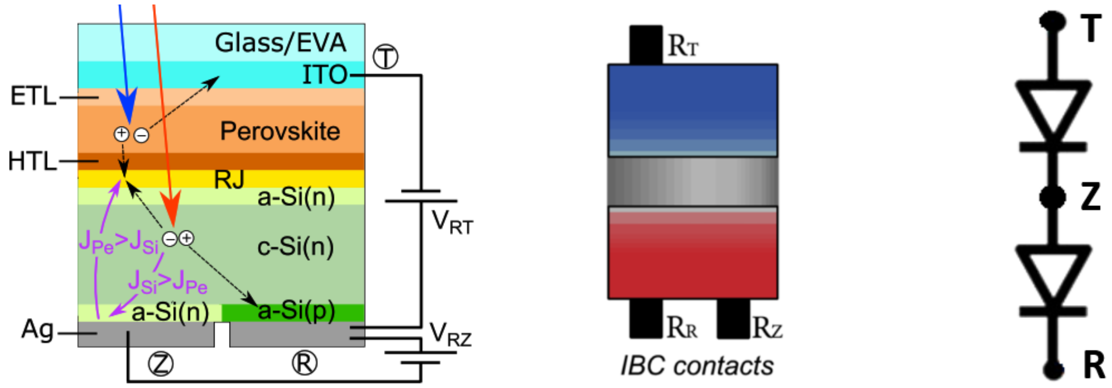

(a) (b) (c)

Figure 2.1 3T configuration (a) schematic cross-section [13] (b) schematic illustration [46] (c) series-type 3T diode representation (c) reverse-type 3T diode representation

Figure 2.1 illustrates the 3T configuration through four representations. Figure 2.1(a) shows a schematic cross-section detailing the layers, including the Glass/EVA, ITO, ETL, HTL, Perovskite, recombination junction (RJ), amorphous and crystalline silicon layers, and the Ag back contact [13]. This configuration includes an interdigitated back contact (IBC) at the bottom cell, providing the third terminal. To understand this configuration, the schematic cross-section is translated into a simplified schematic illustration [46], presented in Figure 2.1(b), highlighting the top cell and bottom cell with IBC contacts and independent electrical pathways. Finally, Figure 2.1(c) presents a diode representation, illustrating the electrical behavior of the s-type 3T configuration with separate circuits for each cell using T, Z, and R contacts. These setups allow each sub-cell to operate independently without requiring additional ITO layers, thereby mitigating current matching and optical loss issues seen in 2T and 4T configurations.

### 2.1.2 3T configuration types

The 3T configuration can be either series-type (s-type) or reverse-type (r-type). In the s-type configuration, the doping sequence of the top and bottom subcells align in the same direction. Conversely, in the r-type configuration, the doping sequence of the bottom cell is reversed relative to that of the top cell [47]. Figure 2.2 below clearly shows the difference of both types.

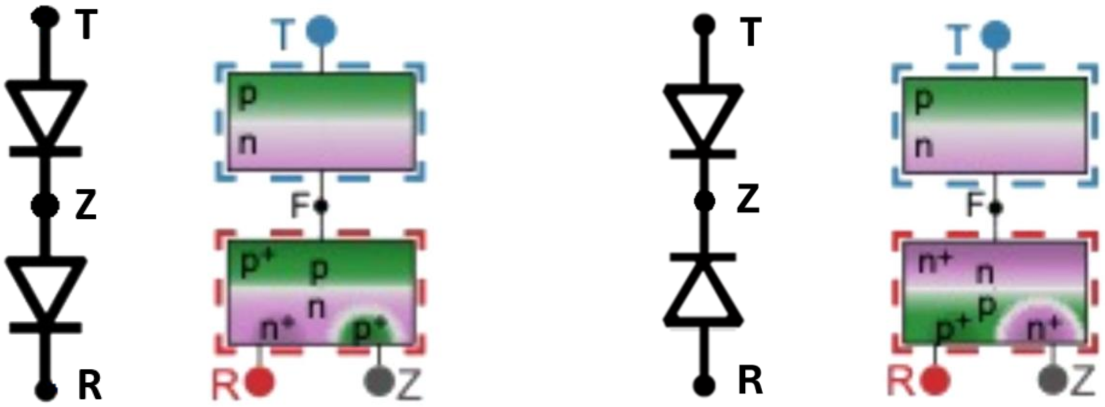

(a) (b) (c) (d)

Figure 2.2 3T Tandem Cell (a) s-type diodes (b) s-type schematic p-n map [47]
(c) r-type diodes (d) r-type schematic p-n map [47]

Figure 2.2 illustrates the 3T tandem cell configuration in both series-type (s-type) and reverse-type (r-type) variations. In the s-type configuration (Figure 2.2a & b), the doping sequence of the top and bottom subcells matches, with diodes oriented in the same direction. The top cell has a p-type layer on an n-type layer, while the bottom cell has an n-type layer on a p-type layer, with a floating contact (F) connecting the subcells. Conversely, the r-type configuration (Figure 2.2c & d) features a reversed doping sequence in the bottom cell, indicated by the opposite diode direction. Here, the bottom cell has a p+ layer on a p-type layer, followed by an n-type layer, differing from the S-Type's sequence and impacting the overall current flow and operation. Because this 3T configuration is more complex than 2T and 4T, it is essential to explain the electron and hole dynamics to better understand how the 3T system works.

### S-type 3T configuration

When the top cell generates the highest current, it absorbs the majority of incident photons, creating electron-hole pairs within its pn-junction. In this structure, electrons generated in the upper p-region move towards the lower n-region due to the built-in electric field, then flow to the connection point F and into the bottom cell. The generated holes in the top cell move in the opposite direction, from the lower n-region towards the upper p-region and are collected at the T contact. In the bottom cell, additional electron-hole pairs are generated from photons passing through the top cell. These additional electrons with the electrons from the top cell move towards the n+ region near the R contact, where they are collected. Simultaneously, holes generated in the bottom cell move towards and are collected by the Z contact, contributing to the overall current. The dynamics of the electrons and holes of this type are presented in Figure 2.3 below.

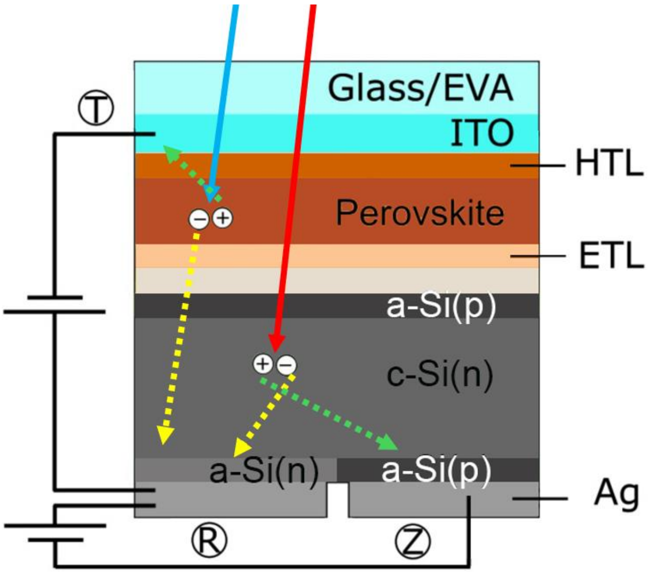

Figure 2.3 Electron-hole movements in the s-type tandem cell

In the diagram, the blue arrow represents the incident light that generates electron-hole pairs in the top cell, and the red arrow represents the incident light with a longer wavelength that generates electron-hole pairs in the bottom cell. The green-dashed arrow represents the movement of electrons, and the yellow-dashed arrow represents the movement of holes.

When the bottom cell generates the highest current, it absorbs more photons, creating more electron-hole pairs. Electrons generated in the bottom cell move towards the n region near the R contact, where they are collected. Simultaneously, holes move towards the p region near the Z contact, where they are collected. In the top cell, although fewer electron-hole pairs are generated, electrons also move into the bottom cell. Holes in the top cell move towards the T contact. This ensures that both cells efficiently collect and contribute to the overall current flow.

### R-type configuration

When the top cell generates the highest current, it absorbs most of the incident photons, creating electron-hole pairs within its pn-junction. Electrons generated in the top cell flow to the bottom cell. Concurrently, the holes generated in the top cell move toward are collected at the T contact. In the bottom cell, additional electron-hole pairs are generated by photons that pass through the top cell. Electrons generated in the bottom cell move towards the n region near the Z contact, where they are collected, while holes generated move towards the lower-left p region and are collected by the R contact. The dynamics of the electron-hole of r-type are presented in Figure 2.4 below

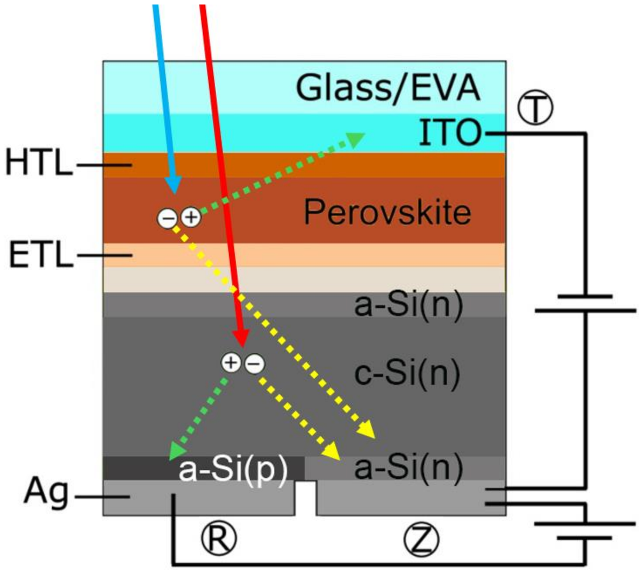

Figure 2.4 Electron-hole movements in the r-type tandem cell

In the diagram, the blue arrow symbolizes the incident light that creates electron-hole pairs in the top cell, while the red arrow signifies the incident light with a longer wavelength that forms electron-hole pairs in the bottom cell. The green-dashed arrow depicts the movement of electrons, and the yellow-dashed arrow illustrates the movement of holes.

When the bottom cell generates the highest current, it absorbs more photons, creating a larger number of electron-hole pairs within its regions. Electrons generated in the bottom cell move towards the n region near the Z contact, where they are collected. Simultaneously, holes generated towards the lower-left p region and are collected by the R contact. Despite generating fewer electron-hole pairs, the top cell continues to function by moving electrons into the bottom cell. Holes in the top cell move towards the T contact, maintaining the circuit's continuity and contributing to the overall current flow.

In both the S-type and R-type tandem solar cells, and in both scenarios where either the top or bottom cell generates the highest current, the efficient collection and movement of charge carriers ensure optimal current generation from both cells. This coordination between the top and bottom cells maximizes the solar cell's efficiency and overall current output. However, in this study, the s-type is chosen to do the calculation and simulation.

This study uses the s-type configuration over the r-type for tandem solar cells due to its simplicity in integration and reduced complexity in design. S-type configurations avoid the need for additional isolation layers and complex current collection systems required by R-type cells. This leads to lower interconnection losses and better overall efficiency. The S-type also allows for more flexible subcell material choices and better management of spectral and thermal sensitivities, making it a more practical and efficient option for real-world applications (McMahon, 2023).

### 2.1.3 3T tandem module

This complex s-type 3T tandem cell is connected with other tandem cells to form a tandem module. The complexity of the cell continues at the module level. An example of a 3T tandem module is shown in Figure 2.5 below.

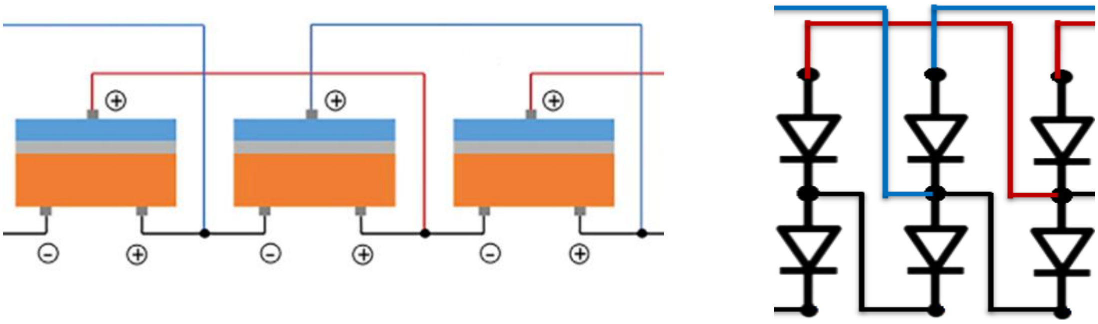

(a) (b)

Figure 2.5 3T Tandem Module (a) schematic illustration [48] (b) s-type diode representation

Figure 2.5 illustrates a complex 3T tandem module through two representations. Figure 2.5(a) shows a schematic illustration of the 3T tandem module, which consists of multiple tandem cells connected in series. Each tandem cell includes independent connections for the top and bottom cells, with the addition of an interdigitated back contact (IBC) for the bottom cell, providing the third terminal. The schematic details how these cells are interconnected to form the module, with separate pathways for the top and bottom cells, facilitating independent operation. Figure 2.5(b) simplifies this structure into a diode representation, illustrating the electrical behavior of the module. Each tandem cell is represented by a pair of diodes, one for the top cell and one for the bottom cell, connected in series. The blue and red lines indicate the independent electrical pathways for the top and bottom cells, respectively.

To simplify the connection of 3T tandem cells, the Voltage-Matched (VM) method is introduced [47]. This voltage-matching reduces sensitivity to variations in the solar spectrum and ensures that both the top and bottom subcells are operating close to their optimal power points. It allows for greater flexibility in the design and interconnection of these solar cells, making them more adaptable to different environmental conditions and improving their overall performance. Equation 2.1 below details the VM ratio.

$$\frac{V_{top}}{V_{bot}} = \frac{m}{n} \tag{2.1}$$

Equation 2.1 describes the relationship between the voltages of the top ($V_{top}$) and bottom subcells ($V_{bot}$) in a VM string, where m and n are integers. There are two VM ratios that are commonly used in existing literature which are 2/1 and 3/2. Higher integers for voltage ratios would result in significantly longer and more complex interconnect paths, requiring additional insulation layers and increased series resistance, leading to higher string-end losses and inefficiencies. These complexities would make the module design less practical and more expensive, thus reducing the overall performance and cost-effectiveness of the solar cells [49]. Therefore, in this study, VM ratio 2/1 is chosen because it is favored for its simplicity and robust performance under varying conditions, while the 3/2 ratio can offer better alignment with certain subcell characteristics but requires careful consideration of end losses and interconnection complexity [46]. The VM ratio in a module can be understood with Figure 2.6 below.

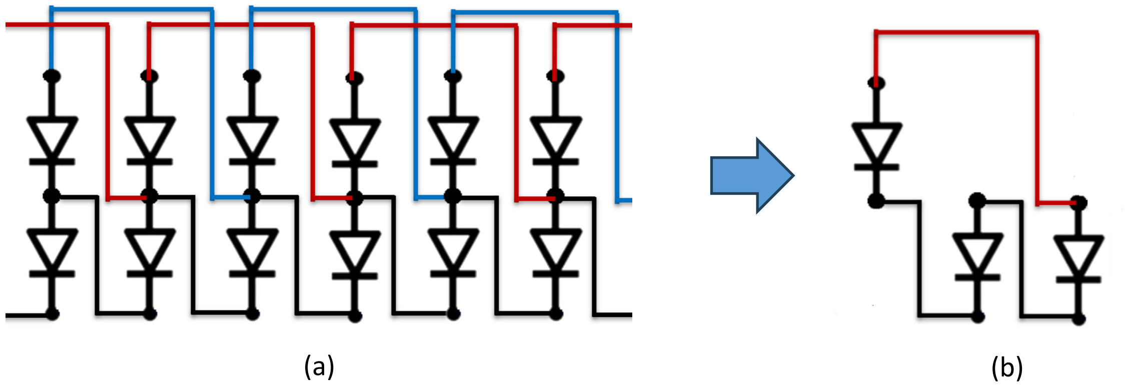

Figure 2.6 3T Configuration (a) string configuration (b) single segment of 2/1 VM ratio

Figure 2.6 depicts the configuration of a 3T tandem module setup using a 2/1 VM ratio. Figure 2.6(a) shows a string configuration with its complex connections. Figure 2.6(b) zooms in on a single segment of this string, demonstrating one top subcell connected in parallel with two series-connected bottom subcells, clearly depicting the 2/1 VM ratio. Thus, the VM ratio can be translated into n top cells being connected in parallel to m bottom cells.

### 2.1.4 3T model development

Once the VM ratio is fully understood, a complete module can be constructed. Before diving into larger scale cell modules, it is helpful to start by explaining smaller scale module to build a foundational understanding. In this subsection, it is assumed that this 8-cell string is forming a module. Figure 2.7 below shows the s-type 3T 8-cell module with VM ratio of 2/1.

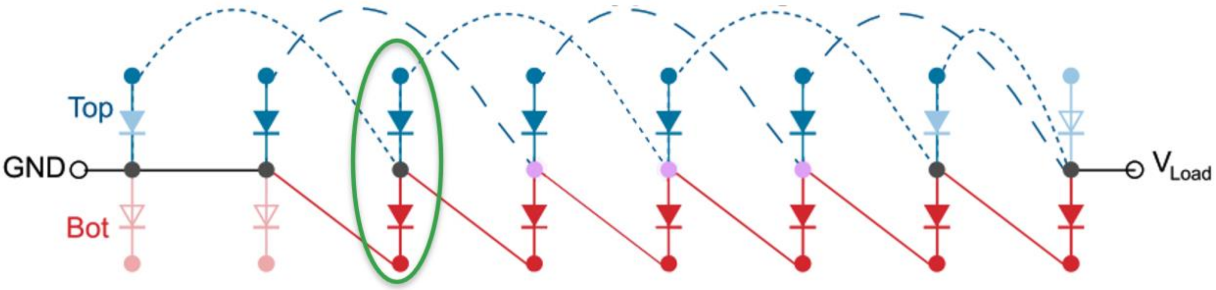

Figure 2.7 S-type 3T 8-cell module with VM ratio 2/1 [47]

Figure 2.7 shows that the blue diodes are the top cells, the red diodes are the bottom cells with GND serving as the ground and the $V_{load}$ point is where the generated power is delivered. The green-circled tandem cell represents a parameter called the repeat unit. This parameter is key to calculating the output parameters of the 3T configuration. From the graph, the blue lines represent the m top-cell current paths, and the red lines represent the n bottom-cell current paths. The black lines indicate the wires carrying multiple current paths. In the entire module system, these lines are intertwined. Thus, the formula to calculate a single repeat unit current can be known as shown in Equation 2.2 below [47].

$$I_{module} = I_{rpt} = m \cdot I_{top} + n \cdot I_{bot} \tag{2.2}$$

The equation describes how the total current flowing through a module ($I_{module}$) is determined by the sum of the currents through the top and bottom subcells. In this context, the total current of the module is equal to the current through each repeat unit. The currents through the top and bottom subcells are combined, where VM ratio is considered. With this ratio, the voltage of each repeat unit can be calculated also. Equation 2.3 below shows the formula to calculate it.

$$V_{rpt} = \frac{V_{top}}{m} = \frac{V_{bot}}{n} \tag{2.3}$$

The equation describes the voltage across each repeat unit in a 3T module. The voltage of the repeat unit ($V_{rpt}$) is equal to the voltage of the top subcells ($V_{top}$) divided by the number of top-cell current paths ($m$), which is also equal to the voltage of the bottom subcells ($V_{bot}$) divided by the number of bottom-cell current paths ($n$). With the formulas to get $I_{rpt}$ and $V_{rpt}$ have been identified by multiplying Equation 2.2 and 2.3 the formula to get the power, thus.

$$P_{tandem} = P_{rpt} = I_{top} \cdot V_{top} + I_{bot} \cdot V_{bot} \tag{2.4}$$

The equation represents the power output of a tandem 3T configuration ($P_{tandem}$). It states that the power output of each tandem is equal to the power output of each repeat unit ($P_{rpt}$). Therefore, to get the power output of the module ($P_{module}$), $P_{rpt}$ needs to be multiplied by number of repeating units ($N_{rpt}$). Equation 2.5 below shows the formula.

$$P_{module} = N_{rpt} \cdot P_{rpt} = N_{rpt} \cdot P_{tandem} \tag{2.5}$$

The equation can be identified as the module being configured in a series connection. Therefore, the formula to get the module voltage ($V_{module}$) can be determined. Equation 2.6 shows it.

$$V_{module} = N_{rpt} \cdot V_{rpt} \tag{2.6}$$

However, due to the red, green, and black lines that are intertwined, they will introduce end losses related to the current extraction. Thus, the $N_{rpt}$ will always be less than number of cells ($N_{cell}$). Equation 2.7 presents the calculation of $N_{rpt}$ of s-type 3T module.

$$N_{rpt} = N_{tot} + 1 - (m + n) \tag{2.7}$$

With $m$ and $n$ are from the VM ratio. Therefore, the power loss of the module due to end losses ($P_{endloss}$ ) can be obtained. The formula to calculate $P_{endloss}$ is shown by Equation 2.8.

$$P_{endloss} = P_{rpt} \cdot \left(N_{cell} - N_{rpt}\right) \tag{2.8}$$

This end loss can be seen in Figure 2.16 as they are fully colored, half-shaded, and unshaded diodes. Each represents the diode that delivers full, half, and no power, respectively. Moreover, when the current generated by the subcells in a tandem configuration is not perfectly matched, this leads to suboptimal performance and reduced overall efficiency of the solar module. Thus, this introduces another loss called mismatch losses. Equation 2.9 explains the power loss due to mismatch ($P_{mismatch}$).

$$P_{mismatch} = \left( \sum_{i=1}^{N_{cell}} P_{mpp,top,i} + P_{mpp,bot,i} \right) - I_{module} \cdot (V_{module} + I_{module} R_{intercon}) \tag{2.9}$$

The formula for $P_{mismatch}$calculates the difference between the sum of the maximum power points (MPP) of the top ($P_{mpp,top}$) and bottom ($P_{mpp,bot}$) cells for all cells in a module and the product of the $I_{module}$ and $V_{module}$, including the voltage drop due to the interconnection resistance. Equations 2.2 through 2.9 will be the fundamental formulas for the development of the 3T model. These equations lay the groundwork for understanding the electrical behavior and performance metrics of 3T tandem cell and module, allowing for accurate modeling and optimization of their design and operation. Thus, the 3T model can be developed by translating these equations into a MATLAB model, which will be integrated into the existing PVMD Toolbox.

## 2.2 Implementation of developed 3T model

The equations from the previous section are translated into MATLAB to create a 3T model. This model is then integrated into the PVMD Toolbox, which can be expanded into a module consisting of a certain number of cells that the user desires. The toolbox has an existing 3T prototype model but has not yet been thoroughly completed or validated. Therefore, in this study, the 3T model will be developed from scratch to ensure the project's independence and that the new 3T developed model is consistent with the equations used. The developed model will be integrated into the Electrical Model, as previously shown in Figure 1.7. The implementation of the equations into the Electrical Model inside the PVMD Toolbox can be seen in APPENDIX E.1 Flowchart of the 3T model implementation

The Electrical Model uses inputs from Cell, Module, Weather, and Thermal simulation results. These results are used to generate the $V_{top}$ and $V_{bot}$ of each tandem cell in the existing Electrical model. Then, the users can choose the electrical configuration they desire. If the users pick the 3T configuration, the model that this project built will be started. The users need to input the $m$ and $n$ ratios and the type, either series or reverse. The $N_{rpt}$ will be calculated based on these inputs. Then, the generated $V_{top}$ and $V_{bot}$ is divided by $m$ and $n$ ratios, respectively. The $I_{top}$ and $I_{bot}$ are obtained by interpolating currents to the $V_{top}/m$ and $V_{bot}/n$. Once these parameters are obtained, the $I_{string}$ and $V_{string}$ can be calculated. Thus, the $I_{module}$ and $V_{module}$ can be acquired, which are then used to plot the IV curves in the existing Electrical model. Furthermore, with these 2 parameters, the $P_{module}$ can be obtained as well. These results are then used to calculate the annual energy yield by integrating the maximum value of $P_{module}$ times its respective daylight hours for a year; thus, the annual energy yield can be plotted. The $P_{endloss}$ and $P_{mismatch}$ can be integrated into the existing Loss Analysis model in the existing toolbox also to complete this developed 3T model. The developed 3T model needs validation to ensure its accuracy and robustness, which will be explained in the next section.

## 2.3 Model validation

Model validation is a critical step in developing this 3T model. By comparing the model's predictions with the literature and simulations, we can identify discrepancies and refine the model to improve its accuracy. Model validation aims to build confidence in the model's predictive capabilities, ultimately leading to a more reliable and efficient 3T model.

### 2.3.1 Validation with existing literature

The fundamental formulas used in this study are derived from the work of McMahon (2021) [47]. Consequently, the model built for this study will be validated against the results presented in McMahon's work. The parameters that are used in this validation are shown in Table 1 below.

Table 1 Validation parameters

| Parameters | Value |
|---|---|
| $V_{top}$ (V) | 1.51 |
| $V_{bot}$ (V) | 1.0 |
| $I_{top}$ (mA) | 3.1 |
| $I_{bot}$ (mA) | 3.0 |

Since the original sample data used by McMahon (2021) [47] is not publicly available, these voltages and currents are iterated and adjusted to align with the published results. However, the method to calculate the parameters stated in previous sections is the same as McMahon's. Then, these input data are used to generate the IV curve, which is calculated using Equations 2.1 to 2.3. The IV curve comparison between McMahon's and the developed 3T model is shown in Figure 2.8 below.

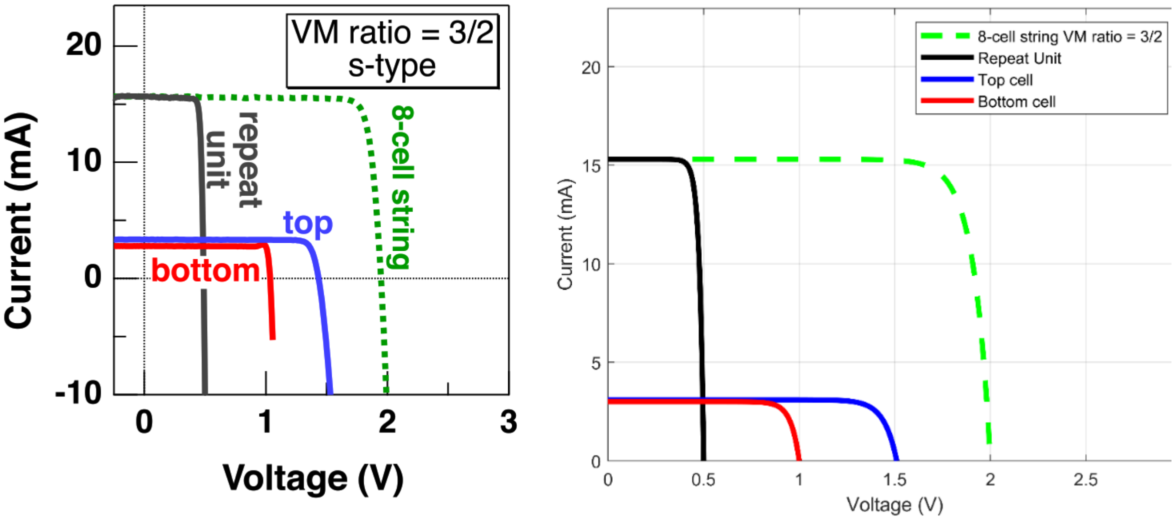

(a)

(b)

Figure 2.8 IV curves of (a) McMahon model (b) developed 3T model

Figure 2.8 contains two plots comparing IV curves for 8-cell VM 3/2 using 3T configuration. As mentioned before, this 8-cell string is assumed to form a module in this validation. The different VM ratio was also used only to validate and match McMahon's plot. The developed model is designed to align closely with the McMahon model, as demonstrated by the current-voltage IV curves presented in the image. Both models exhibit similar overall shapes and trends in their IV curves for the top cell, bottom cell, repeat unit, and the entire 8-cell string. The general shapes of the IV curves for the top cell (blue line), bottom cell (red line), repeat unit (black line), and 8-cell string (green dashed line) are similar in both models. This indicates that the developed model accurately captures the essential electrical behaviors of the three-terminal tandem solar cell configuration as represented in the McMahon model. The small differences observed in the IV curves may be due to different assumptions or improvements in the modeling approach, but overall, the developed model provides a reliable representation of the performance predicted by the McMahon model.

### 2.3.2 Validation with LTSpice

LTSpice is a widely used electrical simulation software that finds applications in various fields, such as physics, computer science, materials science, and electrical engineering. Researchers have utilized LTSpice for tasks ranging from circuit simulation and noise signal generation [50] to predict the electrical behavior of devices like p-n junctions [51]. Thus, LTSpice is reliable software for accurately simulating the output of real electrical devices. The developed 3T model using MATLAB in the PVMD Toolbox will be validated against the LTSpice model to ensure its accuracy, leveraging LTSpice's robust simulation capabilities to compare the model's predictions with practical electrical behavior.

### The LTSpice vs real device output.

In Ahmet Toprak's (2018) study [52], the comparison between LTspice simulations and experimental measurements shows high accuracy. The threshold voltage ($V_{th}$) obtained from the LTspice simulation is 4.25 V, while the experimental measurement yields a $V_{th}$ of 4.2 V. This close agreement, with a minor difference of just 0.05 V, demonstrates the precision of the simulation. Furthermore, the simulation's on/off ratio ($I_{on}/_{off}$) is 106, compared to the experimental value of 107, showing a negligible difference of 1. The subthreshold swing (SS) is another critical parameter where the simulation value is 0.030 V/decade, and the experimental measurement is 0.033 V/decade, differing by only 0.003 V/decade. These results collectively illustrate that LTspice accurately represents the MOSFET's behavior, closely matching the real device outputs.

In the paper by Liu et al. (2020) [48], the LTspice simulations are compared with experimental measurements of quantized resistance in graphene Corbino p-n junction devices. Both the simulation and experimental results show a quantized resistance (RH) of approximately 12906 Ω at the $\nu = 2$ plateau. This exact match between the simulated and measured values highlights the effectiveness of LTspice in modeling complex quantum Hall phenomena in graphene devices. The consistency between the simulation and experimental data validates the numerical model used and confirms the reliability of LTspice in predicting the behavior of graphene-based quantum devices under specific conditions.

The comparisons in both papers demonstrate the high accuracy of LTspice simulations when compared to real device outputs. These findings collectively affirm that LTspice is a robust tool for accurately predicting electronic device behaviors, closely aligning with empirical data.

### Validation setup

The validation is done on the existing tandem cell model in PVMD Toolbox. The model is adapted from Mariotti et al. (2023) [9] which has 1.68 eV of perovskite layer and 32.5% efficiency at STC as the foundational structure. A limitation of the PVMD Toolbox is that the cell structure for GenPro4 must be one-dimensional, making it impossible to implement an IBC (Interdigitated Back Contact). To simulate a 3T tandem cell with an IBC contact, we assume that the optical results are identical for both contacts. The schematic stack of the tandem cell can be seen in Figure 2.9 below.

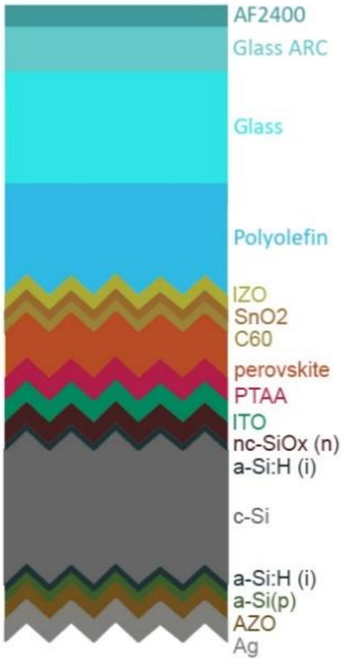

Figure 2.9 Schematic stack of the perovskite/silicon tandem cell model

Figure 2.9 shows the existing schematic stack tandem cell model by Mariotti et al. (2023) adapted into the PVMD Toolbox. The thickness of each material is detailed in Table 2 below.

Table 2 Thickness of each layer's tandem cell

| Material | Thickness (μm) |
|---|---|
| AF2400 | 0.093 |
| GlassARC | 0.053 |
| Glass | 3200 |
| Polyolefin | 450 |
| IZO | 0.085 |
| SnO2 | 0.005 |
| C60 | 0.007 |
| perovskite | 0.575 |
| PTAA | 0.023 |
| ITO | 0.063 |
| n-SiOx-ncSi | 0.111 |
| a-Si(i) | 0.009 |
| c-Si | 160 |
| a-Si(i) | 0.006 |
| a-Si(p) | 0.012 |
| AZO | 0.055 |
| Ag | 0.3 |

The structure incorporates advanced materials, such as IZO and AZO, to enhance electrical conductivity and light absorption. Essential layers include a SAM or PTAA hole transport layer, SnO2 and C60 electron transport layers, and intrinsic amorphous silicon (a-Si) layers for passivation. The validation will be carried out on this tandem cell under STC, including 1000 W/m2 irradiance and a temperature of 25°C, to ensure a reliable comparison between the LTSpice model and the developed 3T model results. Specifically, the LTSpice model is built on the equivalent circuit of the 3T tandem cell and will be scaled up to a 72-cell module. The equivalent circuit of 3T is shown in Appendix B.1.

The LTSpice model shown in Appendix B.2 represents a 3T tandem solar cell. This tandem cell is then expanded into a 72-cell module using an s-type connection. After this expansion, the module will be simulated. The parameters used by the LTspice model are the same as those used by the developed 3T MATLAB model to simulate this module. Table 3 below shows the parameters that are used for both simulations.

Table 3 Parameters used for LTSpice validation

| Parameters | Top Cell | Bottom Cell |
|---|---|---|
| $R_{sh}$ (Ohm) | $1.216408 \times 10^{-5}$ | $1.244995 \times 10^{-5}$ |
| $R_s$ (Ohm) | 7.19 | 7083.75 |
| $I_{ph}$ (A) | 4.52 | 4.88 |
| $I$ (A) | $1.731628 \times 10^{-11}$ | $1.389943 \times 10^{-9}$ |
| $n$ | 1.78 | 1.27 |

Table 3 shows the parameters employed for simulating a 3T module using both the LTspice model and the developed model in MATLAB for the PVMD Toolbox. These parameters ensure that both simulations are conducted under the same conditions, allowing for a reliable comparison between the LTSpice and MATLAB models.

### Developed model vs LTspice model results

The validation process begins by comparing the simulation results of the developed 3T model and the LTspice model to see how closely the top and bottom cell IV curves match when they operate independently. By isolating the performance of each subcell, we can directly compare the simulated results from LTSpice and MATLAB. This approach ensures that the comparison is free from interdependencies or coupling effects between the cells, providing a clear and accurate assessment of each model's performance. Figure 2.10 below is the IV curves comparison of individual top and bottom cells using both models.

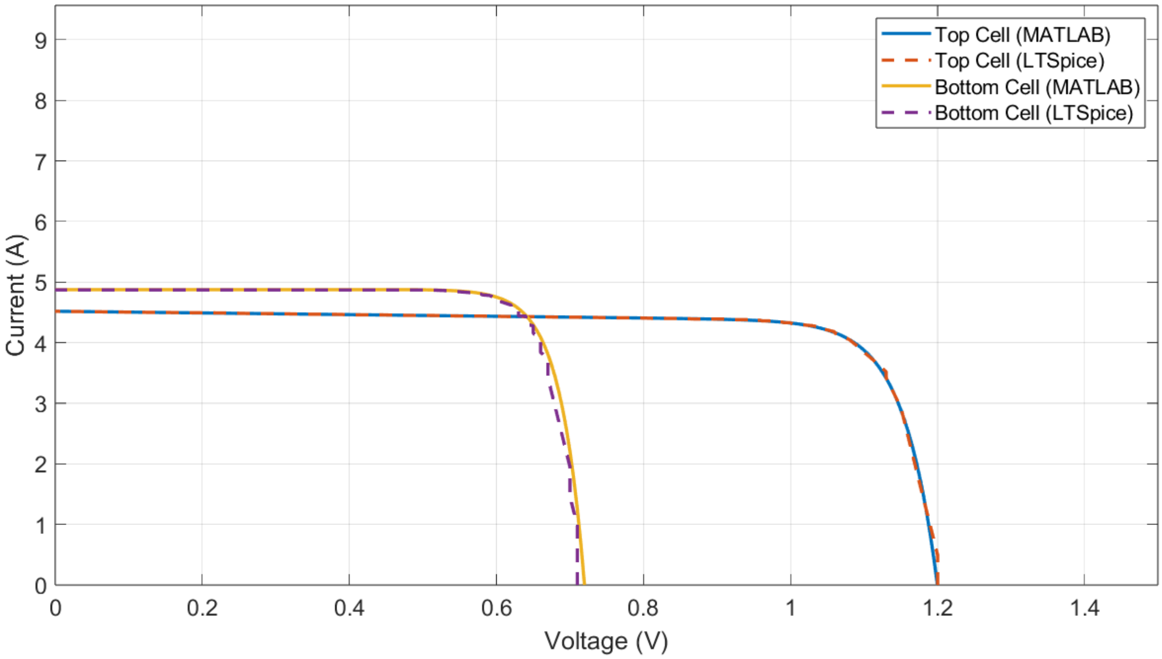

Figure 2.10 IV curves comparison of developed 3T model vs LTSpice model

Figure 2.10 compares the IV curves of the top and bottom cells of a 3T tandem module, simulated using MATLAB and LTSpice models under STC. The MATLAB simulation curves (solid blue for the top cell and solid red for the bottom cell) closely match the LTSpice simulations (dashed orange and dashed purple, respectively). This close alignment across the voltage range indicates that the MATLAB model produces results consistent with the LTSpice model. Figure 2.11 below shows the simulation results for the expanded 72-cell module.

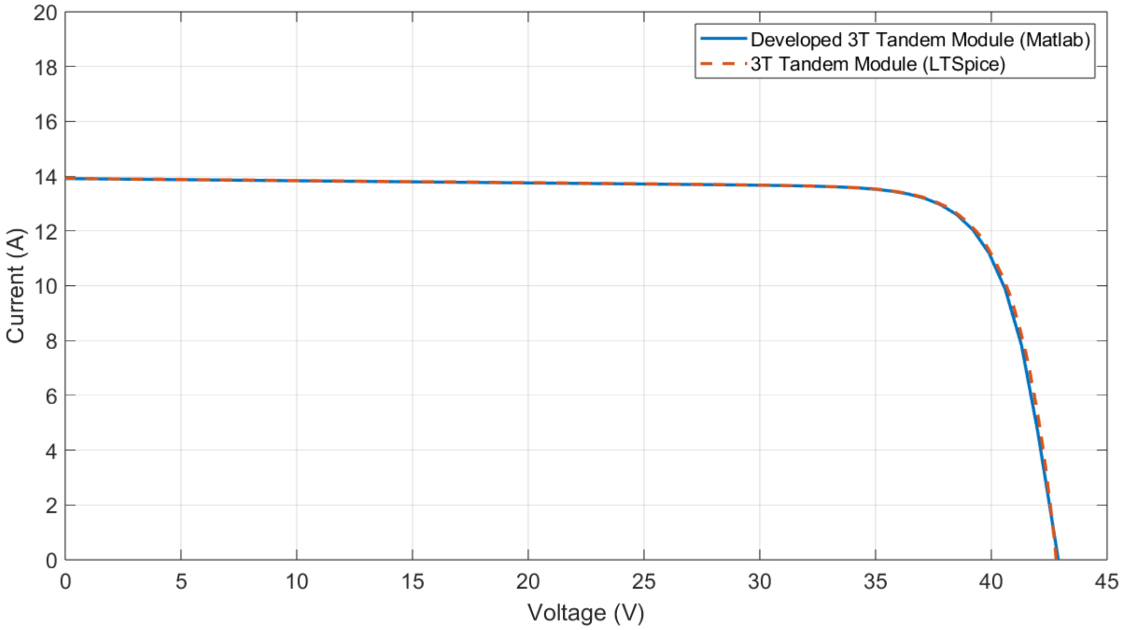

Figure 2.11 IV curves comparison of developed 3T vs LTSpice module models

Figure 2.11 This figure compares the IV curves of a 72-cell 3T tandem module simulated using both MATLAB and LTSpice models. The IV curve from the developed 3T MATLAB model simulation (solid blue line) closely aligns with the IV curve from the LTSpice model simulation (dashed orange line), indicating that both models produce highly similar results.

The root mean square error (RMSE) analysis ensures that the comparison is legitimate. RMSE is a widely used metric in various fields to evaluate the accuracy of predictive models by measuring the differences between predicted values and actual observations [53]. In this case, the predicted values are MATLAB data, and the actual observations are LTSpice data. The RMSE formula can be seen in Equation 2.20 below.

$$RMSE = \sqrt{\frac{1}{n}\sum_{i=1}^{n}(X_i - x_i)^2} \tag{2.20}$$

Equation 2.20 presents the formula for calculating the Root Mean Square Error (RMSE) to compare LTSpice output with MATLAB output. In this context, $n$ is the number of samples, $X_i$ is LTSpice data, and $x_i$ is the MATLAB data. The RMSE is determined by taking the square root of the mean of the squared differences between the LTSpice and MATLAB data points, which results in 0.10146 W. An RMSE of 0.10146 W compared to the maximum power of the IV curve of around 490 W is considered very good, as RMSE value of 0 indicates a very accurate [54]. It suggests that the developed 3T MATLAB model is highly accurate, with errors being only about 0.02% of the data's range. This validation confirms that the developed 3T model is reliable for further analysis and development of the 3T tandem module.

## 2.4 Conclusion

This chapter presents that the initial Sub-Objective 1: Implement and validate the developed three-terminal (3T) model, has been successfully addressed. The successful validation instills confidence in the predictive capabilities of the new 3T model, setting a solid foundation for subsequent research and development efforts in optimizing tandem solar cell technology.

In this chapter, we developed and validated a comprehensive 3T model for the PVMD Toolbox. The model enhances the 2T and 4T models by incorporating an additional contact in the bottom cell, allowing for independent operation of each sub-cell without additional ITO layers. This configuration mitigates current matching and optical losses observed in 2T and 4T models.

We detailed the process for generating IV curves and energy yield, which is crucial for understanding the performance metrics of photovoltaic cells. The validation of the developed 3T model involved comparing its predictions with existing literature and simulations using

LTSpice. The developed 3T model closely aligns with McMahon's work and LTSpice simulations, demonstrating its accuracy and reliability.

The validation with LTSpice showed a high degree of accuracy, with an RMSE of 0.02% errors, confirming the model's reliability for further analysis and development. In conclusion, the developed 3T model provides a more efficient and accurate tool for simulating the performance of tandem solar cells.

# CHAPTER III

# COMPARING THE PERFORMANCES OF 2T AND 3T MODULES

This chapter specifically addresses Sub-objective 2: Analyze and compare the performance of the three-terminal (3T) module with the two-terminal (2T) module, as introduced in Section 1.5.2 Thesis Objectives. The existing 2T and developed 3T models are used to simulate the 2T and 3T tandem cells, both having the same optimized 2T parameters, such as perovskite bandgap energy of 1.68 eV and thickness of 575 nm. Then, these tandem cells are expanded to form 2T and 3T modules, each consisting of 72 cells. To simulate a three-terminal tandem cell with an IBC contact, we assume that the optical results are identical for both contacts in all simulations in this study. The interconnection resistance is also assumed to be 0 to simplify the simulations. The simulation outcomes provide a foundation for further optimization of the 3T module's energy yield by modifying the perovskite bandgap energy and thickness. Through a detailed examination of the simulation data, strategies for enhancing the performance and efficiency of the 3T module can be identified and implemented.

The chapter begins with the IV curve simulation results, allowing for a comparative analysis between the IV curves generated using the existing 2T and developed 3T models. Subsequently, the chapter delves into the energy yield simulation results. Additionally, the model is simulated across four distinct locations, each representing a different climate, to evaluate its performance under varied environmental conditions comprehensively.

## 3.1 IV curve simulation under STC

This section provides simulation results of the 2T and 3T cells and modules under Standard Test Conditions (STC). First, the explanation of the IV curves of a single tandem cell for 2T and a single repeating unit for 3T explains how the existing 2T and developed 3T models work. Afterward, the IV curves of 2T and 3T modules are described. The 2T and 3T tandem cell and module are first simulated under STC, which includes a light intensity of 1000 W/m², a cell temperature of 25°C, and an air mass of 1.5. These idealized conditions provide a consistent and controlled environment, making it easy to compare the performance of the two configurations.

### 3.1.1 Existing 2T model

The existing 2T model within the PVMD Toolbox serves as a foundational benchmark for evaluating the performance enhancements of the developed 3T model. By establishing the performance metrics of the 2T model, we create a reference point that facilitates a comprehensive comparison with the 3T model. The symbolized 2T tandem cell and IV curves generated using the existing 2T model are shown in Figure 3.1 below.

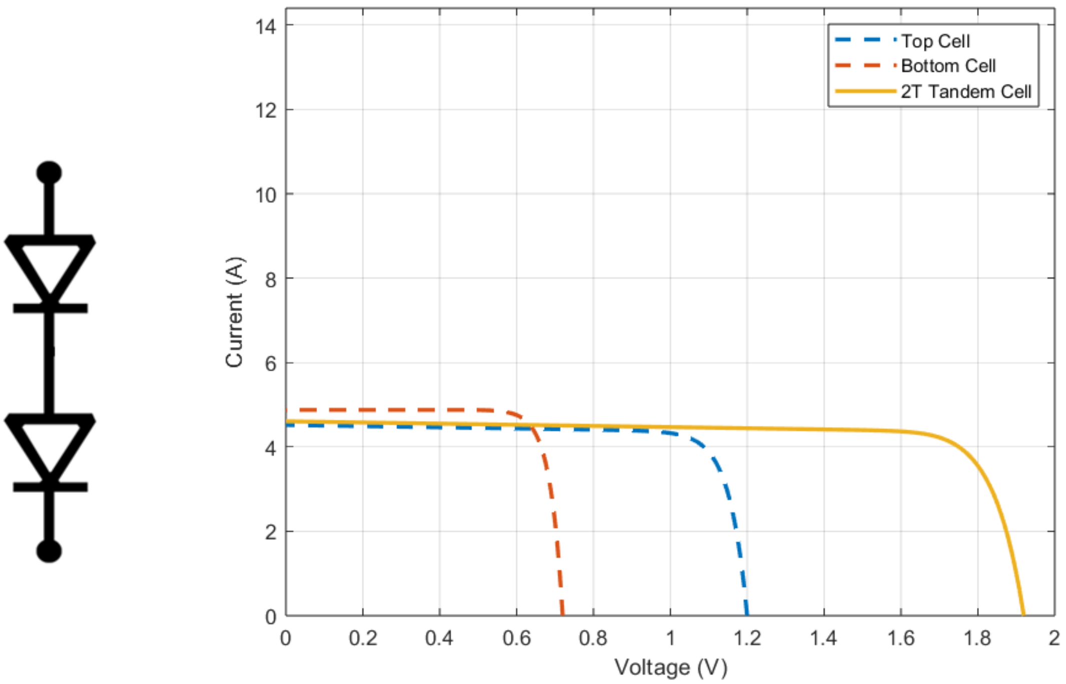

(a)

(b)

Figure 3.1 2T Tandem Cell (a) diode symbol (b) IV Curves

The IV curve in Figure 3.1b illustrates the IV curves of a 2T tandem solar cell simulated using the existing 2T model, which serves as a benchmark for 3T configuration. The dashed blue and red lines represent the I-V curves of the top and bottom cells, respectively, while the solid orange line corresponds to the tandem cell's IV curve. The $I_{sc}$, $I_{mpp}$, $V_{mpp}$, and $V_{oc}$ of each IV curve are shown in Table 4 below.

Table 4 Detailed parameters of 2T IV curves

| | Top Cell | Bot Cell | 2T Tandem Cell |
|---|---|---|---|
| $I_{sc}$ (A) | 4.52 | 4.88 | 4.60 |
| $I_{mpp}$ (A) | 4.19 | 4.64 | 4.25 |
| $V_{mpp}$ (V) | 1.05 | 0.62 | 1.69 |
| $V_{oc}$ (V) | 1.20 | 0.72 | 1.92 |
| $P_{mpp}$ (W) | 4.42 | 2.88 | 7.18 |

Table 4 above shows that the tandem cell's $I_{sc}$ and $I_{mpp}$ are close to those of the top cell. This limited current is due to the nature of tandem cells in the 2T configuration, where the overall current is constrained by the lower current-producing subcell in the tandem structure. The tandem configuration is symbolized by the two diodes in series in Figure 2a, representing the top and bottom cells connected in series, which collectively contribute to the overall voltage while being limited by the lower current of the two cells.

### 3.1.2 Developed 3T model

The developed 3T model is then used to simulate the 3T tandem cell with similar optimized 2T parameters such as perovskite bandgap energy of 1.68 eV and thickness of 575 nm, allowing for a direct comparison of performances. By employing the same material properties, layer configurations, and STC conditions as the 2T tandem cell, the 3T simulation ensures consistency and reliability in the evaluation process. This approach enables a clear assessment of the benefits offered by the 3T configuration. The symbolized 3T repeat unit and IV curves generated using the developed 3T model are shown in Figure 3.2 below.

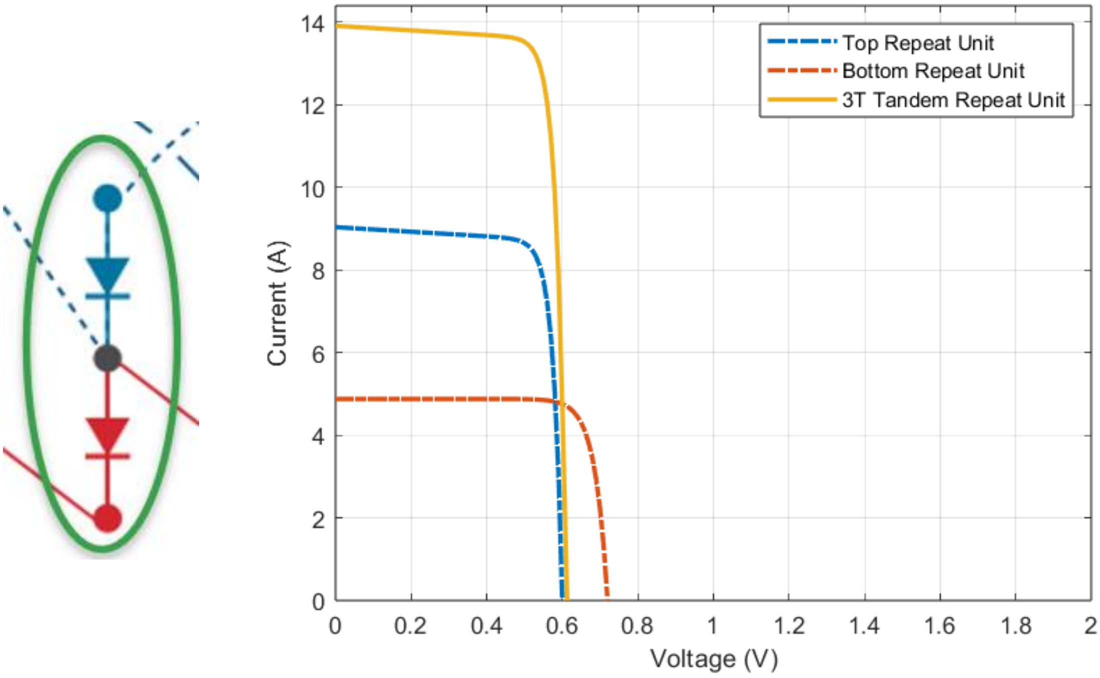

(a) (b)

Figure 3.2 3T Tandem repeat unit (a) diode symbol (b) IV Curves

The graph illustrates the IV curves of the 3T tandem solar cell repeat unit, highlighting the individual performance of the top and bottom repeat units as well as the combined 3T repeat unit. The top repeat unit, the bottom repeat unit, and the 3T repeat unit are represented by the blue dash-dot, the red dash-dot, and the solid orange lines, respectively. Due to the 2/1 VM ratio, the top cell depicted only represents half of its voltage but with doubled current, reflecting the voltage-matched method used in this 3T configuration. The $I_{sc}$, $I_{mpp}$, $V_{mpp}$, and $V_{oc}$ of each IV curve are shown in Table 5 below.

Table 5 Detailed parameters of 3T IV curves

| | Top Repeat Unit | Bot Repeat Unit | 3T Repeat Unit |
|---|---|---|---|
| $I_{sc}$ (A) | 9.04 | 4.88 | 13.92 |
| $I_{mpp}$ (A) | 8.33 | 4.65 | 12.96 |
| $V_{mpp}$ (V) | 0.53 | 0.62 | 0.54 |
| $V_{oc}$ (V) | 0.60 | 0.72 | 0.62 |
| $P_{mpp}$ (W) | 4.42 | 2.88 | 7.00 |

Table 5 shows the 3T tandem repeat unit's $I_{sc}$ and $I_{mpp}$, which are the additions of the top and bottom repeat units. This is because, conceptually, the top and bottom repeat units are connected in parallel in the VM method. The 3T repeat units $V_{mpp}$ is similar to the lower $V_{mpp}$ between the top and bottom repeat units due to the voltage-matched method used for this configuration.

### 3.1.3 Existing 2T vs developed 3T models

The existing 2T and the developed 3T models are used to simulate the 72-cell modules, expanding their application from a single tandem cell and a repeat unit to more complex and scalable structures. This transition leverages the foundational principles established in 2T and 3T, incorporating them into a larger, more practical solar cell configuration. This subsection delves into the specifics of the 72-cell module design and the simulation results of the models.

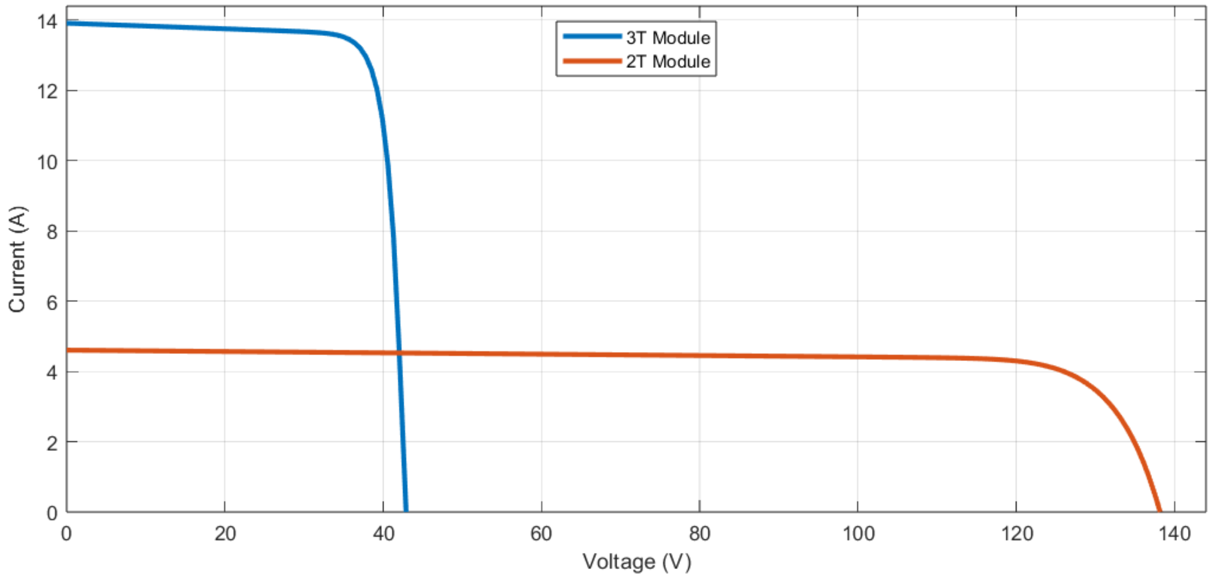

Figure 3.3 IV Curves comparison between 2T and 3T modules under STC

Figure 3.3 illustrates the key differences in the IV curves between 2T and 3T modules under Standard Test Conditions (STC). The IV curves of 2T and 3T modules are represented by red and blue curves, respectively. These curves show that 2T operates at a lower current but higher voltage, while 3T operates at a higher current but a lower current. The parameters are shown in Table 6 below.

Table 6 Detailed parameters of IV curves comparison

| | 2T Module | 3T Module |
|---|---|---|
| $I_{sc}$ (A) | 4.60 | 13.92 |
| $I_{mpp}$ (A) | 4.25 | 12.96 |
| $V_{mpp}$ (V) | 121.68 | 37.80 |
| $V_{oc}$ (V) | 138.24 | 44.64 |
| $P_{mpp}$ (W) | 517.14 | 490.00 |

Table 6 shows that the 2T module yields more power than the 3T module. This is due to the simulations using the optimized 2T perovskite bandgap energy and thickness. Moreover, the end losses also cause this to happen, as there are inactive subcells within the 3T module. Despite this, the 3T module still demonstrates significant potential by yielding a high-power output of 490 W. The higher $I_{sc}$ and $I_{mpp}$ of the 3T module indicates its efficiency in extracting photo-generated carriers.

### 3.1.4 Loss analysis

The loss analysis is essential to confirm that all potential sources of loss have been addressed. Equation 2.23 calculates the end losses, while other losses may occur as well. The loss details are shown in Table 7 below.

Table 7 Loss analysis results

| | 2T | 3T |
|---|---|---|
| Power Output (W) | 517.14 | 490.0 |
| End Losses (W) | 0 | 13.50 |
| Mismatch Losses (W) | 8.46 | 22.10 |
| Total | 525.6 | 525.6 |

Table 7 compares the power performance and losses of 3T and 2T modules under STC. For the 3T module, the actual power output is 490.0 W, affected by end losses of 13.50 W from inefficiencies in current extraction and mismatch losses of 22.10 W due to performance variations among individual cells. Despite these losses, the total power under ideal conditions is 525.6 W, indicating significant impacts from design inefficiencies. In contrast, the 2T module has a higher actual power output of 517.14 W with no end losses and significantly lower mismatch losses of 8.46 W, also totaling 525.6 W under ideal conditions. Since both cells have similar subcells, the total power has to be similar for both configurations. Therefore, all the losses have been addressed.

In conclusion, the simulations on the 2T and 3T modules with optimized 2T parameters, such as 1.68 eV perovskite bandgap energy and 575 nm thickness, show that 2T outperforms 3T. However, the 3T configuration has the potential to perform better under real-world conditions. The 3T design is inherently more flexible and can adapt to varying environmental conditions, such as spectral irradiance variation and temperature changes. This adaptability can lead to better performance and higher efficiency in actual operating conditions, where variability in solar irradiance and temperature affects power output. Consequently, while the 2T configuration may show superior performance under STC, the 3T configuration could potentially surpass it in real-world applications due to its ability to handle non-ideal conditions more effectively.

## 3.2 IV curve simulations under real conditions

This section presents the simulation results using the existing 2T model and the developed 3T model under real-world conditions. Initially, the IV curves of a single tandem cell using the 2T model and a single repeating unit using the 3T model are analyzed to illustrate the operational principles of these configurations. The IV curves of the 2T and 3T modules are then discussed to highlight their performance in practical scenarios. These simulations are conducted under realistic conditions to comprehensively compare the modules' effectiveness and reliability in real-world applications. The real condition simulations are performed on January 20th at 14:00 in Delft, the Netherlands, as the sample, using simulation results of the existing SBDART model as explained in section 1.4.1 Toolbox Structure.

On January 20th at 14:00 in Delft, the weather conditions typically include lower solar irradiance due to the winter season, resulting in reduced sunlight intensity. The temperature is relatively low, and the sun is positioned lower in the sky, leading to longer shadows and increased atmospheric scattering of sunlight. The SBDART model, which simulates the atmosphere's spectral radiative characteristics, considers these conditions to provide an accurate representation of the real-world solar irradiance and environmental factors affecting the solar cells' performance at that specific time and location.

### 3.2.1 Existing 2T model

The existing 2T model simulation results also provide a benchmark for assessing the simulation results of the developed 3T model under real conditions. The simulation results of the 2T tandem cell using the existing 2T model under real conditions are shown in Figure 3.4 below.

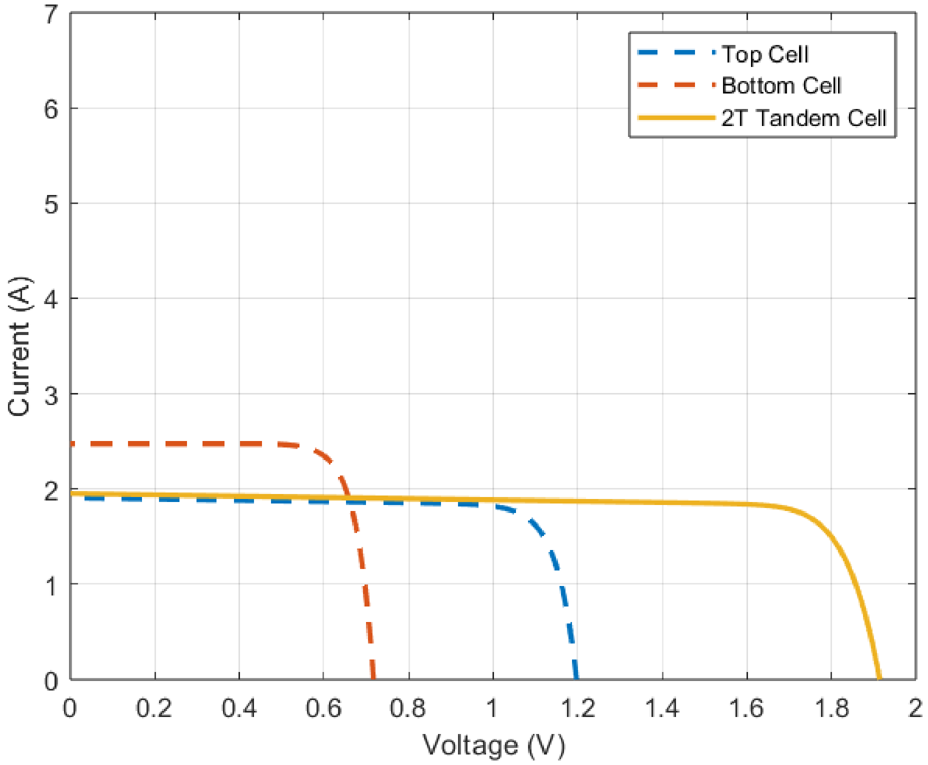

Figure 3.4 2T IV Curves (in real condition)

The dashed blue and red lines represent the IV curves of the top and bottom cells, respectively, while the solid orange line shows the IV curve of the tandem cell. Table 8 below shows the $I_{sc}$, $I_{mpp}$, $V_{mpp}$, and $V_{oc}$ of each IV curve.

Table 8 Detailed parameters of 2T IV curves

| | Top Cell | Bot Cell | 2T Tandem Cell |
|---|---|---|---|
| $I_{sc}$ (A) | 1.90 | 2.48 | 1.95 |
| $I_{mpp}$ (A) | 1.77 | 2.33 | 1.79 |
| $V_{mpp}$ (V) | 1.05 | 0.61 | 1.70 |
| $V_{oc}$ (V) | 1.20 | 0.72 | 1.92 |
| $P_{mpp}$ (W) | 1.85 | 1.41 | 3.04 |

Table 8 shows the values of each parameter of the top cell, bottom cell, and 2T tandem cell in real conditions. The tandem cell's $I_{sc}$ and $I_{mpp}$ are limited by the lower-performing cell, leading to an overall current that is close to the top cell's $I_{sc}$ and $I_{mpp}$. The voltages ($V_{mpp}$ and $V_{oc}$) of the tandem cell are nearly the sum of the individual voltages of the top and bottom cells. The table illustrates how the conceptually series connection in a 2T tandem cell combines the voltages while being constrained by the lower current of the two sub-cells, providing a comprehensive view of the tandem cell's performance characteristics.

### 3.2.2 Developed 3T model

The developed 3T model is used to simulate the 3T tandem cell with optimized 2T parameters. This time, the simulations are done under real conditions. The simulation result is shown in Figure 3.5 below.

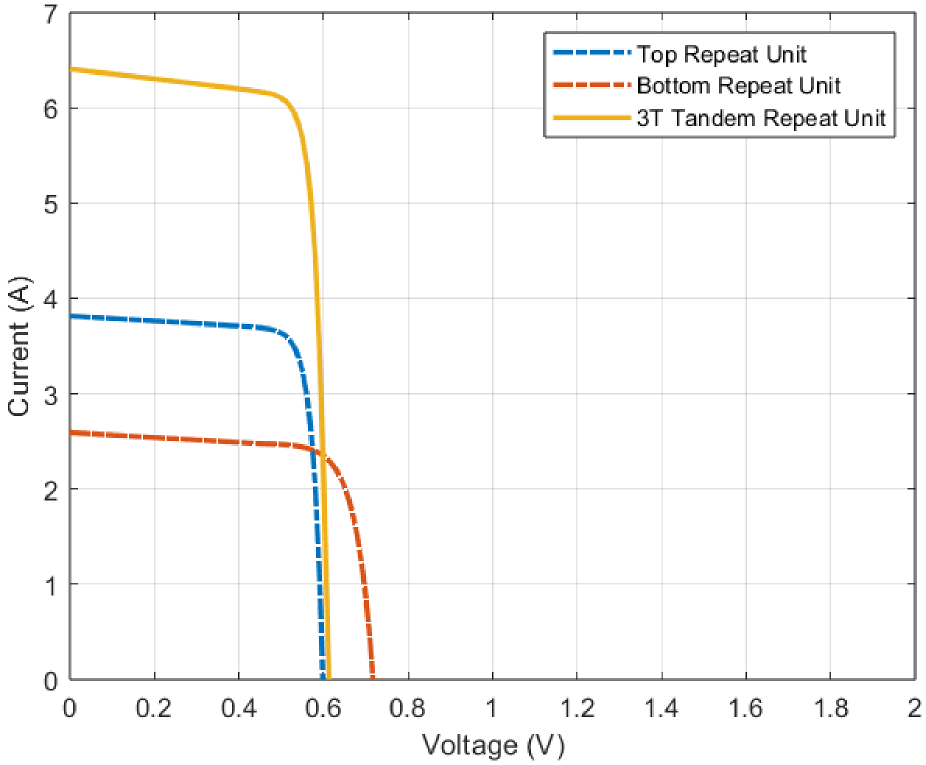

Figure 3.5 3T IV Curves (in real condition)

The blue-dashed, red-dashed, and solid orange lines in Figure 3.5 show the top, bottom, and 3 T tandem repeat units, respectively. Table 9 below shows the parameters of each IV curve.

Table 9 Detailed parameters of 3T IV curves

| | Top Repeat Unit | Bot Repeat Unit | 3T Repeat Unit |
|---|---|---|---|
| $I_{sc}$ (A) | 3.82 | 2.59 | 6.40 |
| $I_{mpp}$ (A) | 3.49 | 2.31 | 5.84 |
| $V_{mpp}$ (V) | 0.53 | 0.61 | 0.54 |
| $V_{oc}$ (V) | 0.60 | 0.72 | 0.62 |
| $P_{mpp}$ (W) | 1.85 | 1.41 | 3.15 |

Table 9 presents the same behavior as the results of STC. It illustrates that the 3T tandem repeat unit's $I_{sc}$ and $I_{mpp}$ are the sum of the top and bottom repeat units. This is due to the conceptual design in the voltage-matched (VM) method, where the top and bottom repeat units are connected in parallel. Consequently, the $V_{mpp}$ is close to the lower $V_{mpp}$ value of the two units, reflecting the voltage-matching configuration employed in this setup.

### 3.2.3 Existing 2T vs developed 3T models under real conditions

The existing 2T and the developed 3T models are then used to simulate the 2T and 3T modules consisting of 72 cells each. The tandem cells that are being simulated have optimized 2T parameters. The IV curves of the 2T and the developed 3T modules are compared and shown in Figure 3.6 below.

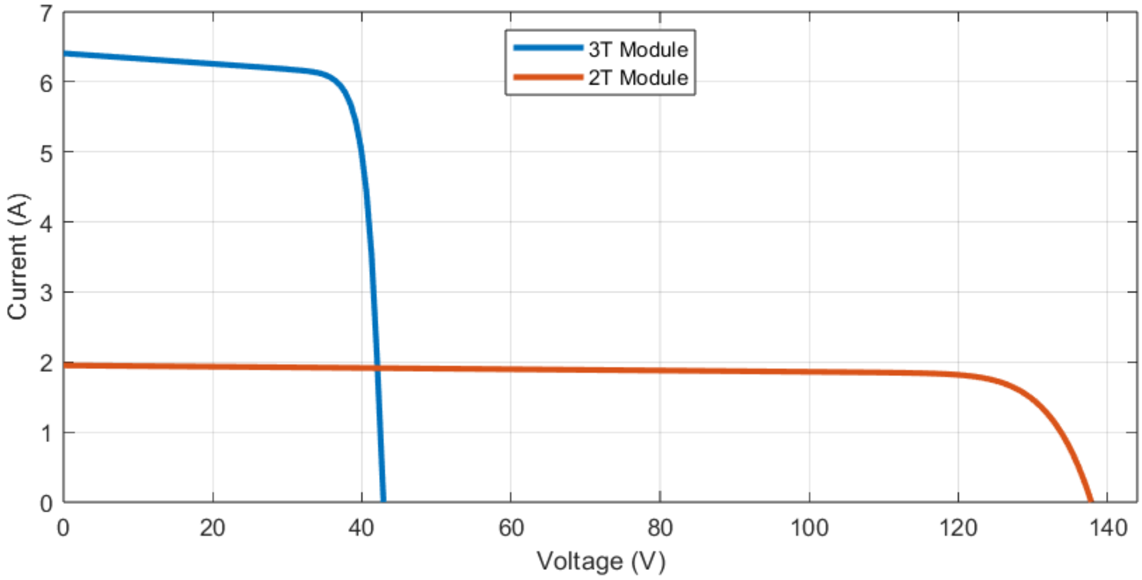

Figure 3.6 IV Curves comparison between 2T and 3T modules in real condition

Figure 3.6 shows the difference between the IV curves of 2T and 3T modules in real conditions. The blue and red lines depict the 3T module and 2T module IV curves, respectively. The 3T module also operates at a higher current and lower voltage, while the 2T module works at a lower current but higher voltage. The parameters of the above curve are shown in Table 10 below.

Table 10 Detailed parameters of IV curves comparison

| | 2T Module | 3T Module |
|---|---|---|
| $I_{sc}$ (A) | 1.95 | 6.40 |
| $I_{mpp}$ (A) | 1.79 | 5.84 |
| $V_{mpp}$ (V) | 122.40 | 37.8 |
| $V_{oc}$ (V) | 138.24 | 43.4 |
| $P_{mpp}$ (W) | 219.10 | 220.75 |

Table 10 compares the performance parameters of 2T and 3T modules under real conditions. The 3T configuration allows for independent operation of the top and bottom cells, optimizing the extraction of photo-generated carriers. Consequently, the higher currents in the 3T module more than compensate for the lower voltage, resulting in an overall higher power output of 220.75 W compared to 2T of 219.10 W. This higher $P_{mpp}$ in the 3T module is primarily due to its enhanced current capabilities. The 3T configuration allows for independent operation of the top and bottom cells, optimizing the extraction of photo-generated carriers and highlighting the potential efficiency benefits of the 3T module in real-world conditions.

### 3.2.4 Loss analysis

The loss analysis also be conducted in these real-world conditions. The detailed losses that occur and power generated are shown in Table 11 below.

Table 11 Loss analysis results

| | 2T | 3T |
|---|---|---|
| Power Output (W) | 219.10 | 220.75 |
| End Losses (W) | 0 | 6.31 |
| Mismatch Losses (W) | 15.62 | 7.66 |
| Total | 234.72 | 234.72 |

Table 11 presents a comparison of the power performance and losses for 3T and 2T modules under real-world conditions. The 3T module demonstrates an actual power output of 220.75 W, with end losses of 6.31 W due to inefficiencies in current extraction and mismatch losses of 7.66 W caused by performance variations among individual cells. Conversely, the 2T module shows a slightly lower actual power output of 219.10 W, with no end losses and higher mismatch losses of 15.62 W. Both 2T and 3T modules have similar top and bottom subcells. Therefore, they should have similar total power. A similar total power calculated of 234.72 W in this condition also suggests that all potential sources of loss have been adequately considered.

Although the 2T module exhibits higher efficiency under STC, the 3T module performs better in real-world scenarios at a certain hour. The 3T design is more flexible and can adjust to varying environmental conditions, such as fluctuations in spectral irradiance and temperature. This flexibility can result in better performance and increased efficiency in real operating conditions, where solar irradiance and temperature changes impact power output. Therefore, while the 2T configuration might appear more efficient under STC, the 3T configuration could potentially outperform it in real-world applications due to its superior adaptability to non-ideal conditions.

## 3.3 Energy yield simulations

This section comprehensively analyzes the energy yields of 2T and 3T modules, using existing 2T and developed 3T models, respectively. By simulating the performance of these modules throughout the year, we aim to evaluate their real-world energy production capabilities under various environmental conditions. The simulations incorporate climate data from different geographical locations, ensuring a robust assessment of the modules' efficiency and reliability across diverse climates. By comparing the results of the 2T and 3T modules, we seek to determine whether the 3T module can surpass the 2T module in energy yield over time. The following subsections delve into the details of the energy yield simulations, including specific analyses for the first two months, a year-long comparison, and performance evaluations across different climates. This approach provides a detailed understanding of the potential advantages and improvements the 3T module offers in practical applications.

### 3.3.1 Energy yield: 2T vs 3T

This section delves into a comparative analysis of the energy yields of 2T and 3T modules in a year. A comprehensive evaluation of their real-world energy production capabilities can be provided by simulating the performance of these modules. The simulation results of both modules using their respective models in the first 2 months are shown in Figure 3.7 below.

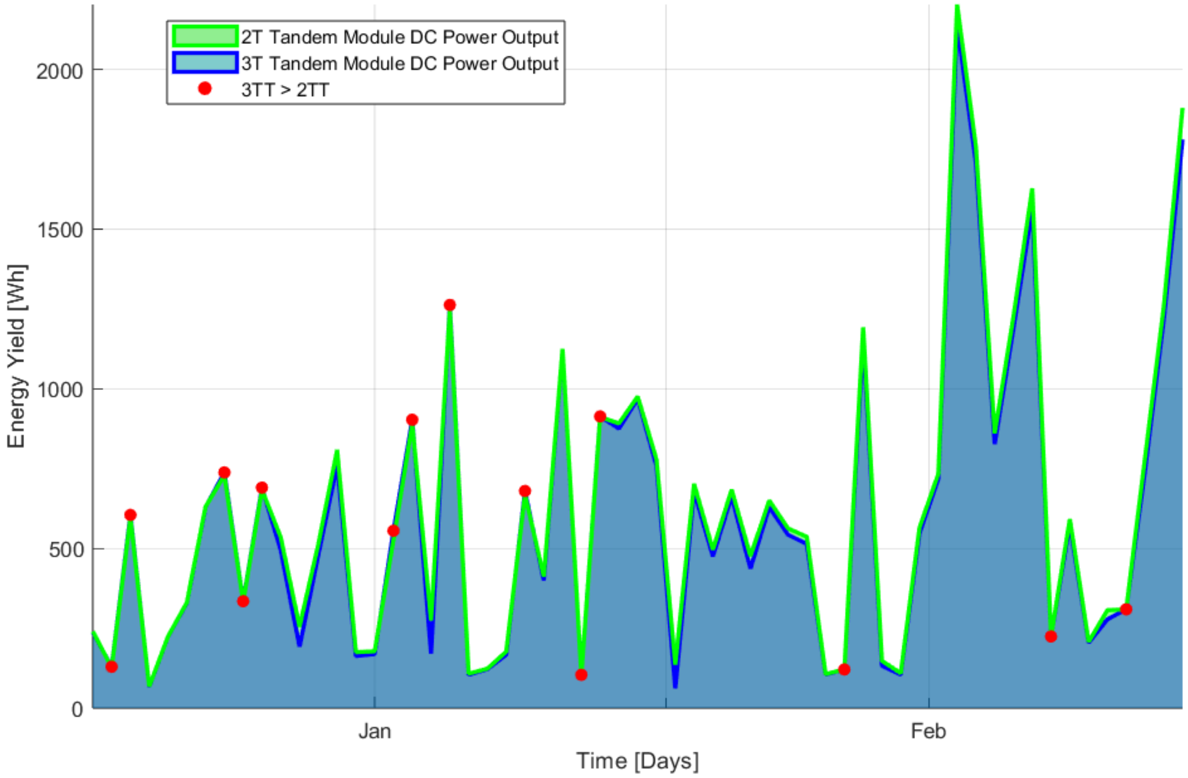

Figure 3.7 Energy yield comparison between 2T and 3T in January and February

The graph compares the daily energy yield (in Wh) of 2T and 3T modules from January to February. The green line represents the energy yield of the 2T module, while the blue line indicates the 3T module's output over 2 months for both. Red dots highlight days when the 3T module outperformed the 2T module. Both modules exhibit significant fluctuations in energy yield, with several peaks. Generally, the 2T and 3T modules show similar performance trends, though the 3T module occasionally produces higher energy yields, as the red dots indicate. The sample of red dots, which shows the hours where 3T yields more power than 2T, is shown by Figure 3.8 below.

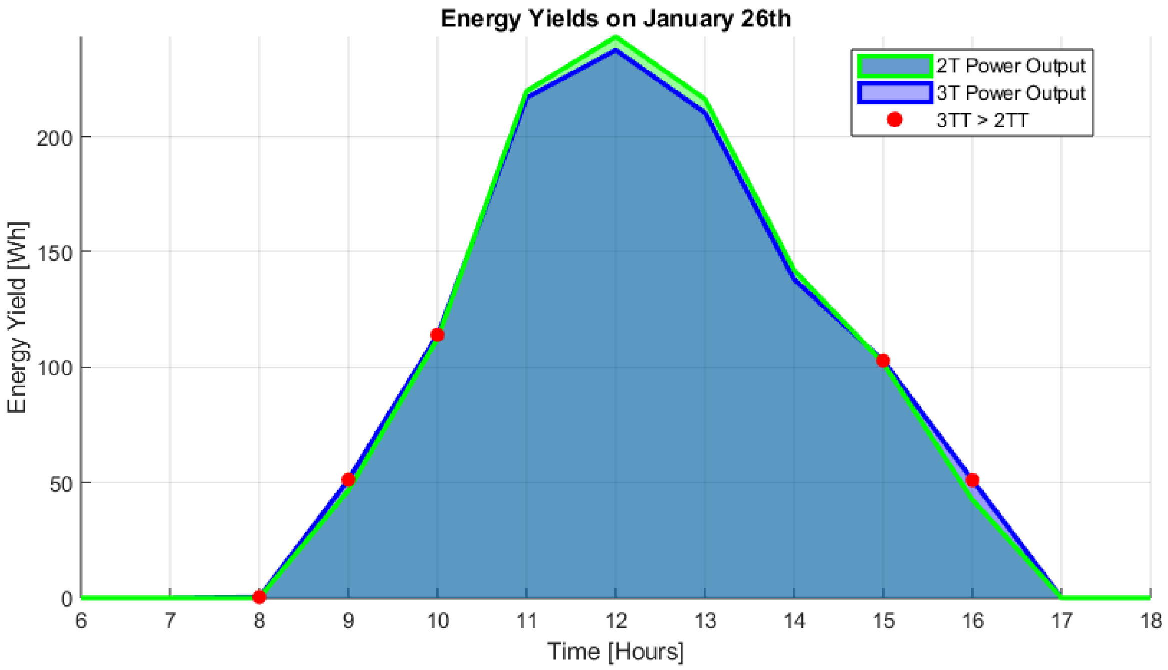

Figure 3.8 Energy yield metrics at 06:00 – 18.00 on January 26th

The graph displays the power outputs of 2T and 3T modules from 06:00 until 18.00 on 26th January. The green-outlined shade blue bar represents the energy yield of the 2T tandem module, while the blue-outlined purple bar represents the 3T tandem module. Both modules perform almost similarly during midday (10:00 to 15:00), with the 2T achieving peak energy yields due to high spectral irradiance and current ratio-matched, making it very efficient. However, in the morning (07:00 to 10:00) and late afternoon (15:00 to 17:00), the 3T module performs better than the 2T module, as indicated by the red dots. This is due to the 2T module's series electrical connection, where the current output is limited by the lowest current cell, leading to inefficiency, especially under low light conditions. The top cell with higher bandgap energy cannot absorb the longer wavelengths of light that occur during these times, which limits the module's output current, even though the bottom cell with lower bandgap energy absorbs more light. This is not the case for 3T, as both subcells can operate at their maximum power point, which makes 3T more efficient at these times.

**Spectral irradiance variation effect**

Spectral irradiance variation plays a crucial role in the performance of tandem solar cells, particularly affecting 2T and 3T configurations. As the spectral distribution of sunlight changes throughout the day and under different cloud conditions, the current generated by the subcells in a tandem configuration can vary significantly. Figure 3.9 below shows the absorbed photons of top and bottom cells on January 26th.

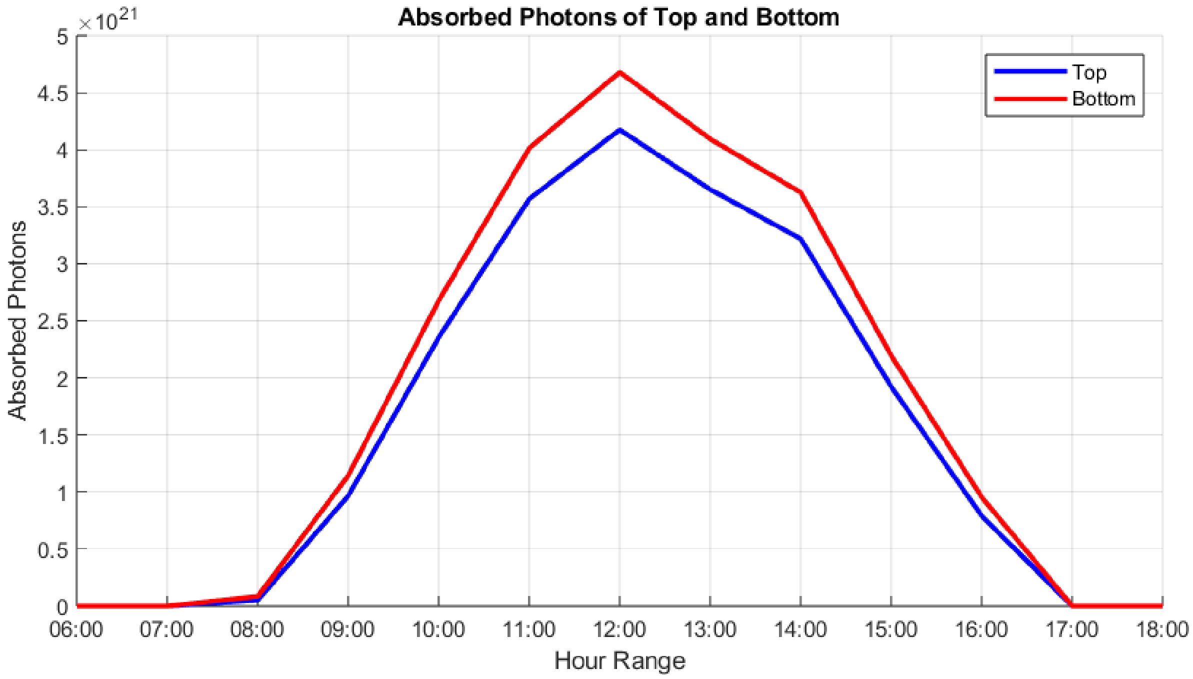

Figure 3.9 Absorbed Photons by Subcells from 06:00 – 18.00 on January 26th

The graph shows the absorbed photons by the top (blue line) and bottom (red line) cells of a tandem module over the hour range from 06:00 to 18:00 on a given day. The y-axis represents the number of absorbed photons/m$^2$. Both cells absorb minimal photons in the early morning (06:00 to 08:00) due to low irradiance as the sun rises. During this time, the sunlight has a higher proportion of longer wavelengths (red and near-infrared) due to atmospheric scattering, which the bottom cell, with its lower bandgap, absorbs more efficiently than the top cell. As the sun rises higher from mid-morning to noon (08:00 to 12:00), the overall irradiance increases and the spectral composition becomes more balanced with higher proportions of shorter wavelengths (blue and green light). The top cell's absorption increases significantly during this period, but the bottom cell continues to absorb more photons overall due to its efficiency in capturing longer wavelengths.

In the afternoon (12:00 to 15:00), as the sun starts to descend, the overall irradiance decreases and the spectral distribution shifts towards longer wavelengths again. The bottom cell maintains its advantage in absorption due to its lower bandgap, although the difference between the cells' absorption rates narrows. In the late afternoon (15:00 to 18:00), the number of absorbed photons drops sharply for both cells as the sun sets and irradiance levels fall. The longer wavelengths dominate the spectral composition, allowing the bottom cell to absorb slightly more photons than the top cell. These spectral shifts and differences potentially introduce current mismatches when top and bottom cells form a tandem module.

**Current mismatch effect on 2T and 3T**

Current mismatch affects the power yield of 2T and 3 T. When there is a large mismatch between currents from the top and bottom cells, the 2T has more losses. However, the 3T has an advantage due to its independent current extraction from the top and bottom cells. Figure 3.10 shows the relation of the current ratio ($I_{top}/I_{bot}$) vs power difference between 3T and 2T ($P3T - P2T$) on January 26th.

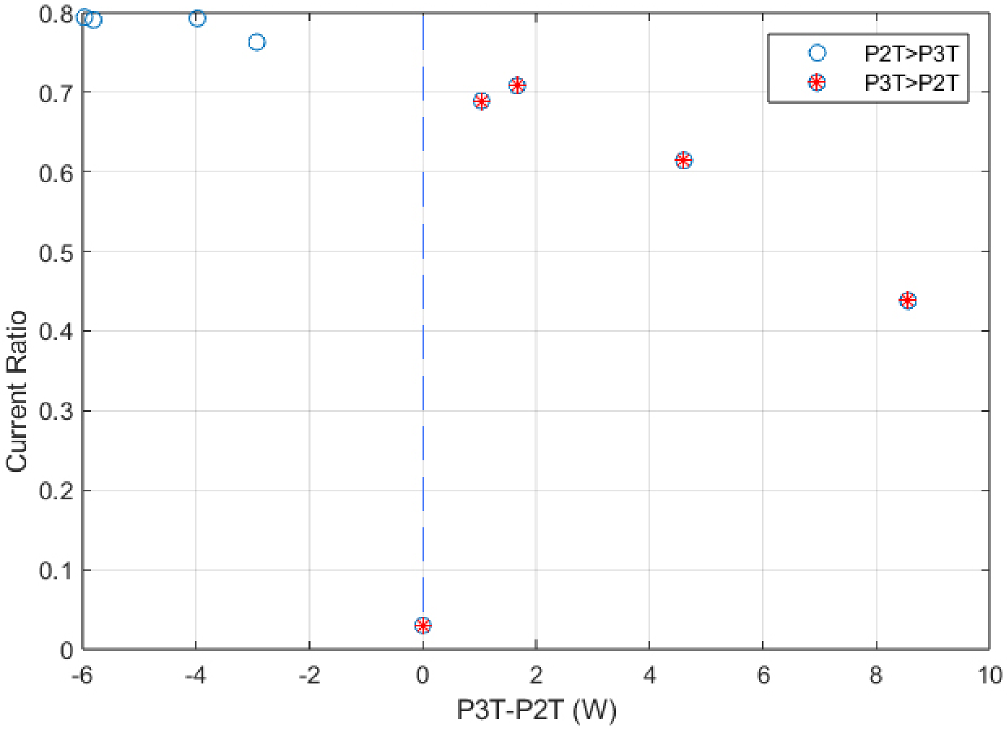

Figure 3.10 Current mismatch ratio vs power difference of 3T and 2T

The graph illustrates the relationship between the current ratio and the power difference between 3T and 2T. The current ratio is plotted on the vertical axis, while the power difference is on the horizontal axis. Two sets of data points are represented: one where $P2T$ produces more power than $P3T$, indicated by blue circles ($P2T > P3T$), and another where $P3T$ produces more power than $P2T$, indicated by blue-circled red stars ($P3T > P2T$). The blue-dashed vertical line at 0 x-axis clearly separates both criteria. The current ratio of 1 indicates that both subcells are perfectly matched, and if it moves away from 1, it introduces a current mismatch. The graph shows that when the current ratio is lower, or it moves away from 1, the power difference tends to favor the 3T configuration, resulting in positive values for $P3T - P2T$. Conversely, when the current ratio is higher or close to 1, the 2T configuration tends to perform better, resulting in negative values for $P3T - P2T$. This suggests that the 3T configuration is better at managing current mismatches, leading to improved power output than the 2T configuration in scenarios with significant mismatches.

**Annual energy yield simulations**

Spectral irradiance variation affects the performance of modules, specifically reducing the efficiency of the 2T module while providing an advantage to the 3T modules. To fully understand this impact, we will investigate the effect of spectral irradiance variation and current mismatch throughout the year or other possible findings. Therefore, the simulation is extended to a year and compared with the incident power to determine when the 3T performs better than 2T. The energy yield vs time graph to compare the incident power and the outputs of 2T and 3T modules is presented in Figure 3.11 below.

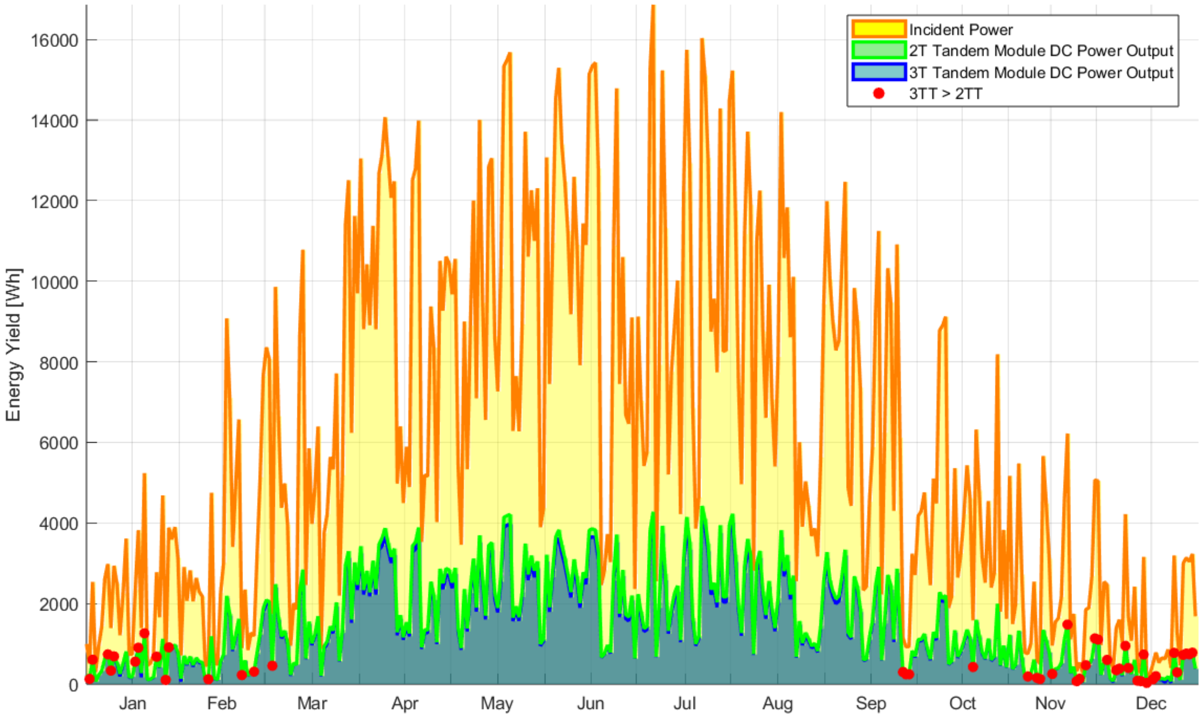

Figure 3.11 Incident energy vs DC power outputs (2T and 3T)

Figure 3.11 illustrates the incident energy and energy yields of both 2T and 3T tandem modules in a year in Delft, the Netherlands. The picture is the extension of Figure 3.7, with the addition of a yellow area and an orange border representing the incident's power. The graph reveals seasonal variations, with lower values during January and February due to the limited solar irradiance typical of the winter months in Delft. However, values start to rise in March as solar irradiance increases with the transition to spring. The 3T module occasionally surpasses the 2T module's output, particularly during the winter months as shown by red dots, indicating its potential advantage in lower irradiance conditions besides its advantage at handling spectral irradiance variation. Ultimately, the 2T still performs better with an annual energy yield of 571 kWh compared to 3T of 544 kWh. However, even though both 2T and 3T simulations use optimized 2T parameters modules with a perovskite bandgap of 1.68 eV and thickness of 575 nm, the 3T module still yields a decent amount of energy with only 4.7% less while occasionally outperforming 2T. These factors show the potential for 3T to yield its optimum power at its own optimized perovskite bandgap energy and thickness.

### 3.3.2 The different climates

The simulations for the annual energy yields were conducted across various climates to evaluate their performance under distinct environmental conditions. Each climate is represented by a specific geographical location, ensuring a comprehensive assessment of the modules' efficiency and reliability. The hourly climate data for these locations was sourced from METEONORM [55], providing accurate and detailed meteorological information. The selected locations and their corresponding climates are:

1. Delft (the Netherlands): This region represents temperate low-irradiance climates characterized by moderate temperatures and relatively lower levels of solar irradiance throughout the year.
2. Lisbon (Portugal): Represents temperate high irradiance climates, where moderate temperatures are combined with high levels of solar irradiance, especially during the summer months.
3. Lagos (Nigeria): Represents tropical high irradiance climates, featuring consistently high temperatures and solar irradiance throughout the year, typical of tropical regions.
4. Shanghai (China): This region represents temperate medium-irradiance climates, which experience moderate temperatures and solar irradiance, with variations between summer and winter months.

The study aims to identify the modules' performance across different environmental conditions by simulating the solar modules in these diverse climates. The simulations will be extended throughout the entire year to comprehensively assess the potential energy yield of the 3T tandem module compared to 2T module. This approach aims to provide a more detailed and rigorous evaluation of the 3T module's performance, particularly in comparison to the 2T module, across varying seasonal and irradiance conditions.

## 3.4 Energy yields comparison

Figure 3.11shows the annual incident energy and the energy yields of the 2T and 3T tandem modules at Delft. Following the analysis of Delft, similar simulations have been conducted for Lagos, Lisbon, and Shanghai. Each location's unique climate characteristics will provide further insights into the performance and potential advantages of the 3T module compared to the 2T module. The full graphs are available in Appendix C.1. The detailed data for these locations are shown in Table 12 below.

Table 12 The energy yield of different locations

| | DELFT | LISBON | LAGOS | SHANGHAI |
|---|---|---|---|---|
| 2T Annual Energy Yield (kWh) | 571 | 979 | 757 | 655 |
| 3T Annual Energy Yield (kWh) | 544 | 931 | 715 | 620 |
| 2T Annual Energy Eff (%) | 20.48 | 19.04 | 20.48 | 21.25 |
| 3T Annual Energy Eff (%) | 19.53 | 18.10 | 19.34 | 20.12 |

The table compares the annual energy yield and efficiency of 2T and 3T tandem modules across Delft, Lisbon, Lagos, and Shanghai, with both modules having similar optimized 2T tandem cell parameters. In all four locations, the 2T module yields around 5% to 6% more energy compared to the 3T module, demonstrating higher annual energy yields and efficiencies. However, from the previous section, it is evident that there are instances, indicated by red dots, where the 3T module yields more power than the 2T module. A detailed explanation will be provided in the next section.

### 3.4.1 Time comparison

This section provides a comparative analysis of the time durations during which the 3T module outperforms the 2T module and vice versa across four locations: Delft, Lisbon, Lagos, and Shanghai. The comparison is based on the number of hours each module configuration shows superior performance over the other throughout the year. The detailed number of hours is shown in Table 13 below.

Table 13 Comparison of 3T and 2T’s dominant hours

| | DELFT | LISBON | LAGOS | SHANGHAI |
|---|---|---|---|---|
| Total Daylight Hours (h) | 4560 | 4562 | 4581 | 4527 |
| Hours 3T>2T (h) | 1183 | 869 | 761 | 820 |
| Hours 2T>3T (h) | 3377 | 3693 | 3820 | 3707 |

Table 13 compares the total annual hours with the hours when 3T outperforms 2T and vice versa across four locations. It shows that 3T yields more power at times in four different locations. This demonstrates that while the 2T module generally performs better, the 3T module has significant potential in certain periods. The comparison when 3T yields more power than 2T is clearer in Figure 3.12 below.

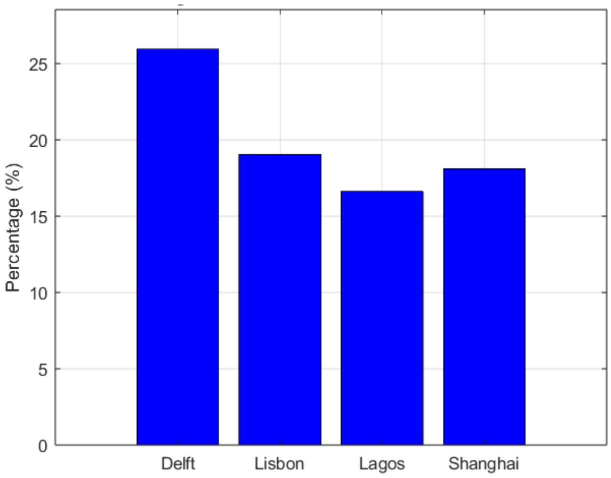

Figure 3.12 Performance Hours of 3T Module at Different Locations

Figure 3.12 highlights that the 3T module outperforms the 2T module for the following percentages of total daylight hours in a year across different locations: Delft (26%), Lisbon (19%), Lagos (17%), and Shanghai (18%). Delft, with its temperate low-irradiance climate, shows the highest percentage, highlighting the 3T module's advantage in moderate temperatures and lower solar irradiance. In Lisbon, a temperate high-irradiance climate, the 3T module performs well during periods of less intense sunlight, despite generally favoring the 2T module. Shanghai's temperate medium-irradiance climate also benefits the 3T module under lower irradiance. Lagos, with its tropical high-irradiance climate, sees the lowest 3T performance. These findings indicate that the 3T module is particularly effective in regions with lower irradiance.

### 3.4.2 Low irradiance

In this simulation, even though the 3T module has optimized 2T parameters with a top cell bandgap of 1.68 eV and 575 nm thickness, it shows significant potential in regions with lower irradiance for several reasons:

- Adaptation to Spectral Variability: Throughout the day, sunlight's spectral composition changes, particularly in low-irradiance environments. The 3T module is designed to optimize the top cell for higher-energy photons and the bottom cell for lower-energy photons. This dual optimization allows the module to better adapt to the varying spectral conditions typically encountered in low-light regions, ensuring more consistent performance.
- Adaptation to Current Mismatch: The 3T configuration allows the top and bottom cells to independently operate closer to their maximum power points. This is particularly advantageous in low irradiance conditions where light intensity is not uniform and may fluctuate throughout the day, which will introduce current mismatches. By independently extracting the currents, the 3T module can more effectively capture and convert available light into electricity, enhancing overall efficiency.

These factors enable the 3T module to perform effectively in lower irradiance regions, demonstrating significant potential by leveraging independent cell optimization, enhanced low-light performance, efficient voltage matching, broad spectral utilization, and resilience to temperature variations.

## 3.5 Conclusion

In Chapter 3, Sub-Objective 2: Analyze and compare the performance of the three-terminal (3T) module with the two-terminal (2T) module has been addressed. The IV curve simulations under Standard Test Conditions (STC) indicated that the 2T module yields higher power due to its optimized tandem cell configuration, achieving a power output of 517.14 W compared to the 3T module's 490.00 W. Under real-world conditions, the 3T module slightly outperformed the 2T module in power output, achieving a power output of 220.75 W compared to the 2T module's 219.10 W at a certain hour. This performance is attributed to the 3T configuration's flexibility in adapting to variations in spectral irradiance and current mismatch, which is crucial for practical applications where real conditions are less than ideal.

Energy yield simulations at four locations over a year highlighted that while the 2T module generally yields 5% to 6% more energy compared to 3T, the 3T module occasionally surpassed it, especially during periods of low irradiance. The spectral irradiance variation and current mismatch effects further supported these findings, showing that the 3T module's ability to handle changes in the spectral distribution of sunlight throughout the day gave it an edge during low light conditions. During midday, the 2T module operated more efficiently due to less current mismatch, but in the early morning and late afternoon, the 3T module performed better by optimizing the output of each subcell individually.

In conclusion, the 2T module demonstrates superior performance under both STC and real-world conditions compared to the 3T module. However, the optimized 2T parameters—specifically, a perovskite bandgap energy of 1.68 eV and thickness of 575 nm—are also applied in the 3T module configuration. Therefore, further optimization is necessary to determine the optimal parameters for the 3T module to enhance its efficiency and reliability across diverse climates and operating conditions, ultimately enabling it to outperform the 2T module.

# CHAPTER 4
# OPTIMIZATION OF 3T MODULE

This chapter addresses Sub-Objective 3: Determine the parameters that optimize the energy yield of the three-terminal (3T) module, as introduced in Section 1.6 Research Gap and Thesis Objectives. By outlining the various optimizations and improvements implemented in the existing PVMD Toolbox and examining their impact on the solar cell's performance. The optimization is done by varying the bandgap and the thickness of the existing tandem cell model-as stated in Section 2.3 Model Validation’s Validation Setup-to get the optimum energy yield of the 3T module.

This chapter details two optimizations: varying the perovskite bandgap energies and changing its thickness. The first section discusses optimizing the module by simulating it at different perovskite bandgap energies to identify the most suitable value for the 3T module. The second section focuses on simulating the module at various perovskite thicknesses to determine the optimal thickness that maximizes the 3T module's performance. Finally, the results of both optimizations are discussed and analyzed to provide comprehensive insights into improving the 3T module's energy yield and efficiency.

## 4.1 Different bandgap energies of the perovskite layer

This section explores optimizing the perovskite bandgap energies for the 3T tandem module. Bandgap energy is a critical factor influencing the absorption spectrum and the solar cell's overall efficiency. By simulating the performance of the 3T module at various bandgap energies, we aim to identify the optimal value that maximizes the energy yield.

### 4.1.1 Simulation setup

The simulation involves adjusting the perovskite bandgap energy within a range typically suitable for tandem solar cells, specifically between 1.5 eV and 1.86 eV. The modules are evaluated based on their energy yield and efficiency to determine the bandgap energy that maximizes the energy yield for both 2T and 3T modules using existing 2T and developed 3T models, respectively. The tandem cell model described in Section 2.3 Model Validation’s Validation Setup is then extended to be a 72-cell module and utilized in this simulation with a perovskite thickness of 500 nm. The location sample of the simulation is Delft, Netherlands, to maintain consistency with the real condition simulations of the previous chapter. The IV curve plotting is also set to be on 26th January. Additionally, the optimum bandgap energy for both 2T and 3T configurations is determined through this analysis.

### 4.1.2 IV curves vs perovskite's bandgap energy

This subsection explains the IV curve of the 72-cell 3T and 2T module simulations at 500 nm at various perovskite bandgap energies at Delft. The IV curves can show the effect of changing the bandgap to the IV curve of the 3T and 2T modules. First, the 2T IV curves are explained in the bandgap range sample of 1.5 eV to 1.7 eV to know the characteristics of the changing bandgap to the power output. IV curves of 2T at different bandgaps at 500 nm thickness are shown in Figure 4.1 below.

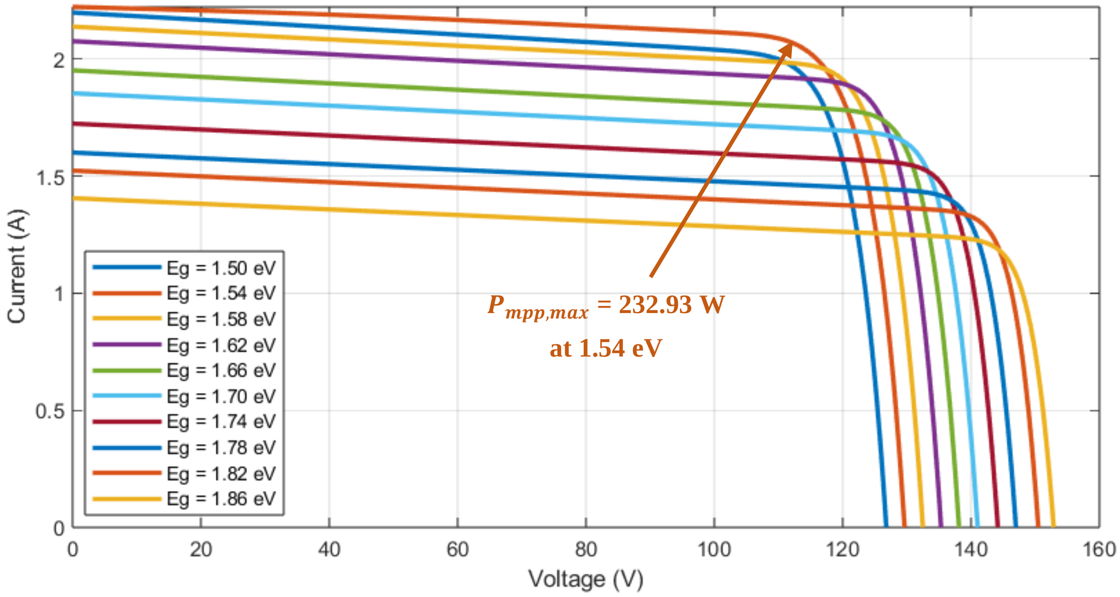

Figure 4.1 2T's IV curves at various bandgaps at 500 nm

The figure above illustrates the IV curves for a 72-cell 2T module at 500 nm, simulated across various perovskite bandgap energies ranging from 1.50 eV to 1.86 eV with a 0.04 eV step. Each colored line in the graph corresponds to a different bandgap energy, showing how the current and voltage output changes with varying bandgap values.

From the IV curves, it is evident that the performance of the tandem cell is highly dependent on the bandgap energy of the perovskite material. As the bandgap increases from 1.50 eV to 1.70 eV, the shape and position of the IV curves shift. Notably, the curve for a bandgap energy of 1.54 eV (dark orange line) achieves the highest $P_{mpp}$ with a value of 232.93 W. Initially, as the bandgap energy increases, the $P_{mpp}$ also increases, reaching its peak at 1.54 eV. Beyond this point, further increases in the bandgap energy led to a decrease in the $P_{mpp}$. This trend suggests that there is an optimal bandgap energy for achieving maximum power output and deviating from this optimal point results in reduced efficiency for the tandem cell module.

Then, the 3T IV curves are detailed in the bandgap range sample of 1.5 eV to 1.86 eV to understand the effect of the changing bandgap on the power output. Figure 4.2 shows the IV curves of the 3T module at this bandgap range and 500 nm thickness.

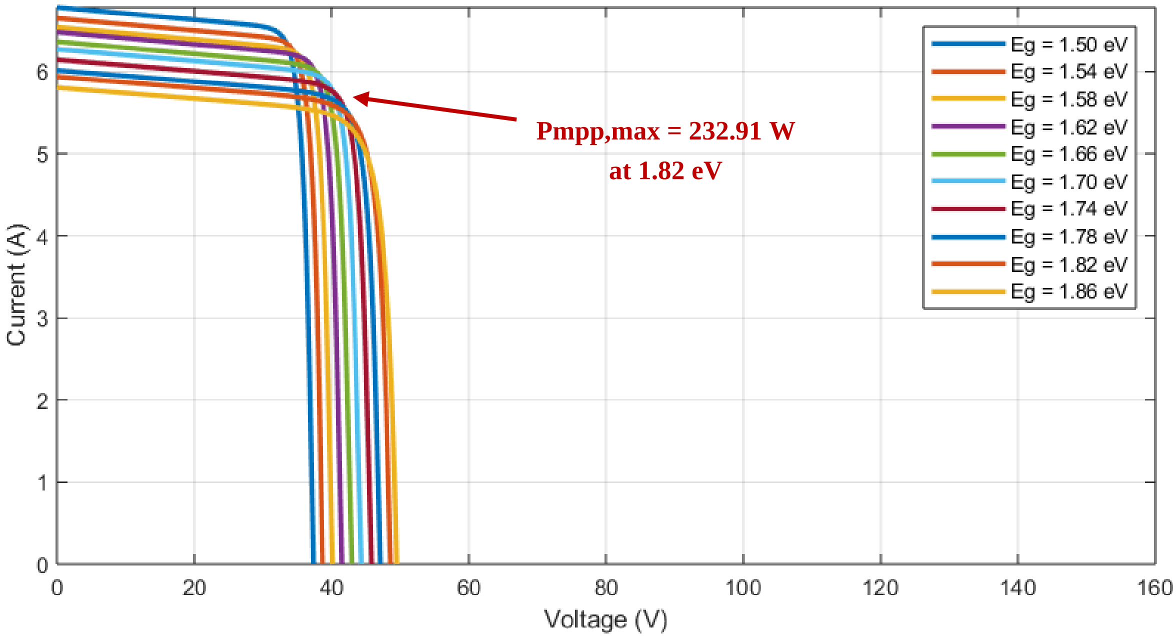

Figure 4.2 3T's IV curves at various bandgaps at 500 nm

Figure 4.2 presents the IV curves for a 72-cell 3T module at 500 nm, simulated for a range of perovskite bandgap energies between 1.50 eV and 1.84 eV with a 0.04 eV gap. Each colored line in the graph corresponds to a specific bandgap energy, demonstrating how the current and voltage characteristics change with different bandgap values. Among the various bandgap energies tested, the curve for a bandgap energy of 1.82 eV (dark red line) achieves the highest $P_{mpp}$, which is 232.91 W. This indicates that at this particular bandgap energy, the 3T module operates at its highest efficiency.

Initially, increasing the bandgap energy leads to an increase in the $P_{mpp}$, reaching a peak at 1.82 eV. Beyond this optimal point, further increases in the bandgap energy result in a decrease in the $P_{mpp}$. This trend highlights the existence of an optimal bandgap energy that yields the maximum power output for the 3T tandem cell module. Deviating from this optimal bandgap, either by increasing or decreasing it, results in a reduction in the module's efficiency and power output.

In both configurations, the analysis highlights the existence of an optimal bandgap energy that maximizes the power output of the tandem cell modules. 2T operates at a lower current but higher voltage and has its optimum at a lower bandgap, while 3T operates at a higher current and lower voltage and has its optimum at a higher bandgap. Deviations from this optimal point, either higher or lower, result in reduced power output.

### 4.1.3 Energy yield vs perovskite's bandgap energy

This subsection expands on the previous simulations of the IV curves by presenting the results for the 72-cell 3T and 2T modules with varying perovskite bandgap energies at 500 nm thickness. The analysis goes beyond the initial IV curves to consider the energy yield over a year, aiming to identify the optimal bandgap that maximizes efficiency and energy yield. Additionally, the 3T configuration is compared with the 2T configuration to highlight improvements in energy yield and efficiency. The comparison of 2T versus 3T energy yield as a function of perovskite bandgap energy is illustrated in Figure 4.3 below.

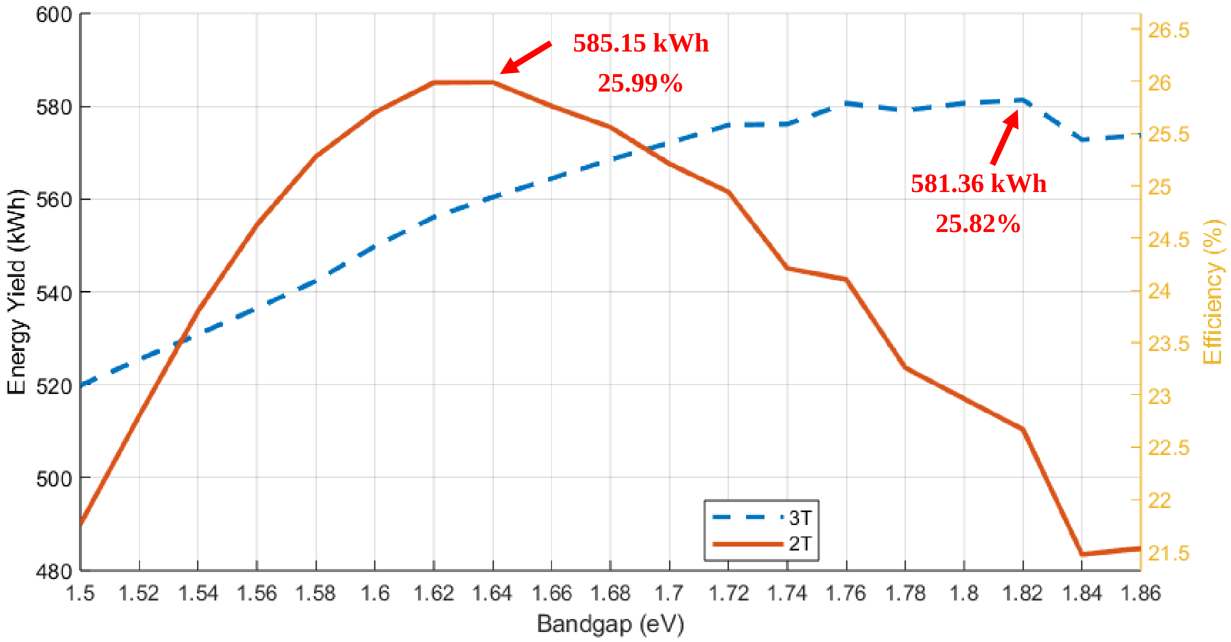

Figure 4.3 Energy Yield vs Perovskite Bandgap Energy

The graph depicts the energy yield of 2T and 3T tandem solar modules as a function of the perovskite layer's bandgap energy (Eg). The x-axis represents the bandgap energy, ranging from 1.5 eV to 1.86 eV, while the y-axis represents the energy yield in kWh. The blue line represents the 2T configuration, and the red line represents the 3T configuration. The arrows and numbers show the peak of each graph.

For the 2T configuration, the energy yield initially increases with the bandgap energy, reaching a peak before declining sharply at higher bandgap values. This indicates that there is an optimal bandgap range for maximizing the energy yield in the 2T configuration, beyond which the performance decreases significantly. The energy yield increases from 578.67 kWh at 1.60 eV to a peak of 585.15 kWh at 1.64 eV, then decreases to 575.43 kWh at 1.68 eV. Therefore, the optimal energy yield is at 1.64 eV, where it reaches its highest value of 585.15 kWh. The optimum bandgap energy of 1.64 eV is different compared to the optimum bandgap of 1.68 eV found by Mariotti [9], because their study was under STC and different thickness of 575 nm.

In contrast, the energy yield for the 3T configuration exhibits a more gradual and consistent increase across the bandgap range, achieving a relatively stable maximum value. The energy yield does not show a significant decline at higher bandgap values, indicating a broader optimal bandgap range for the 3T configuration compared to the 2T configuration. At a bandgap energy of 1.78 eV, the energy yield is 579.04 kWh. As the bandgap increases to 1.80 eV, the energy yield slightly rises to 580.59 kWh. The highest energy yield of 581.36 kWh is achieved at a bandgap energy of 1.82 eV. However, further increasing the bandgap to 1.84 eV results in a decrease in energy yield to 572.80 kWh. This data indicates that the optimal bandgap energy for maximizing the energy yield at this specific thickness is 1.82 eV.

Therefore, the optimum bandgap energy, yield, and efficiency for 2T and 3T tandem solar modules can be compared. For the 2T configuration, the optimum bandgap energy is 1.64 eV, yielding an energy output of 585.15 kWh and achieving an efficiency of 25.99%. In contrast, the 3T configuration reaches its optimum performance at a higher bandgap energy of 1.82 eV, with a slightly lower energy yield of 581.36 kWh and an efficiency of 25.82%. This data suggests that while the 2T configuration is optimized for lower bandgap energy and achieves a marginally higher energy yield, the 3T configuration is nearly as efficient and performs optimally at higher bandgap energy.

## 4.2 Perovskite layer thickness

This section focuses on the impact of the perovskite layer's thickness on the performance of the 72-cell 3T tandem module. The thickness of the perovskite layer affects the absorption of incident light and the recombination losses within the cell. By optimizing the thickness, we can further enhance the module's energy yield.

### 4.2.1 Simulation setup

The perovskite layer's thickness used in the simulation varies from 400 nm to 700 nm with a gap of 100 nm. Each thickness variation is simulated under identical conditions to those used in the bandgap energy optimization. The simulation will be done at the bandgap of 1.64 eV and 1.82 eV, which was mentioned in the previous section as the optimal bandgap of 2T and 3T at 500 nm, respectively. The 72-cell module specifications and the location sample are the same with the simulation setup of different bandgap energies. The simulation's location is Delft, Netherlands, ensuring consistency with the real condition simulations from the previous chapter. The IV curve plotting is specifically set for January 26th. Additionally, this analysis determines the optimal thickness for both 2T and 3T configurations.

### 4.2.2 IV curves vs perovskite's thickness

This subsection explains the IV curve of the simulations of the 72-cell 3T and 2T tandem cell module at 1.64 eV bandgap energy at various perovskite thicknesses as samples. The IV curves can show the effect of changing the thickness to the IV curve of the 3T and 2T modules. First, the 2T IV curves are explained in the thickness range sample of 400 nm to 900 nm to know the characteristics of the changing thickness to the power output. The results of the previous section, which shows the optimum bandgap of 2T is 1.64 eV and 3T is 1.82 eV, will be used in this section to plot the IV curves. Figure 4.4 below is the IV curves of 2T at different thicknesses at 1.64 eV.

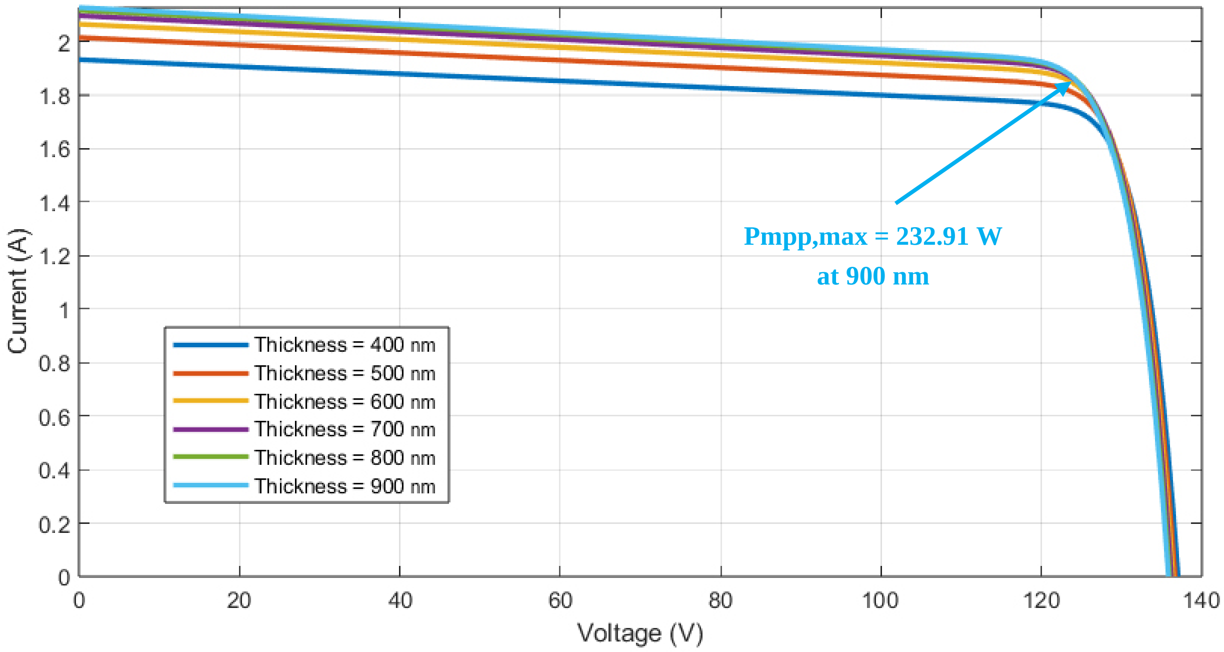

Figure 4.4 2T’s IV curves at various thicknesses at 1.64 eV

Each colored line in the graph represents a different thickness. The IV curves show how the 2T tandem cell module's current and voltage characteristics vary with the perovskite layer's thickness. Notably, the maximum $P_{mpp}$ is achieved at a perovskite thickness of 900 nm, with a value of 232.91 W. This indicates that at this thickness, the module operates at its peak efficiency. This is shown as the perovskite layer thickness increases from 400 nm to 900 nm; the IV curves show improved performance, suggesting that thicker layers enhance the module's ability to generate higher current and voltage, thereby increasing power output. However, further increases may not yield significant improvements beyond an optimal thickness and could reduce efficiency due to material limitations or increased recombination losses.

The IV curves for the 3T module are then examined within a thickness range of 400 nm to 900 nm with a 100 nm gap to analyze the impact of varying bandgap energies on power output. Figure 4.5 displays these IV curves for the 3T module at this specified thickness range and a perovskite bandgap of 1.64 eV.

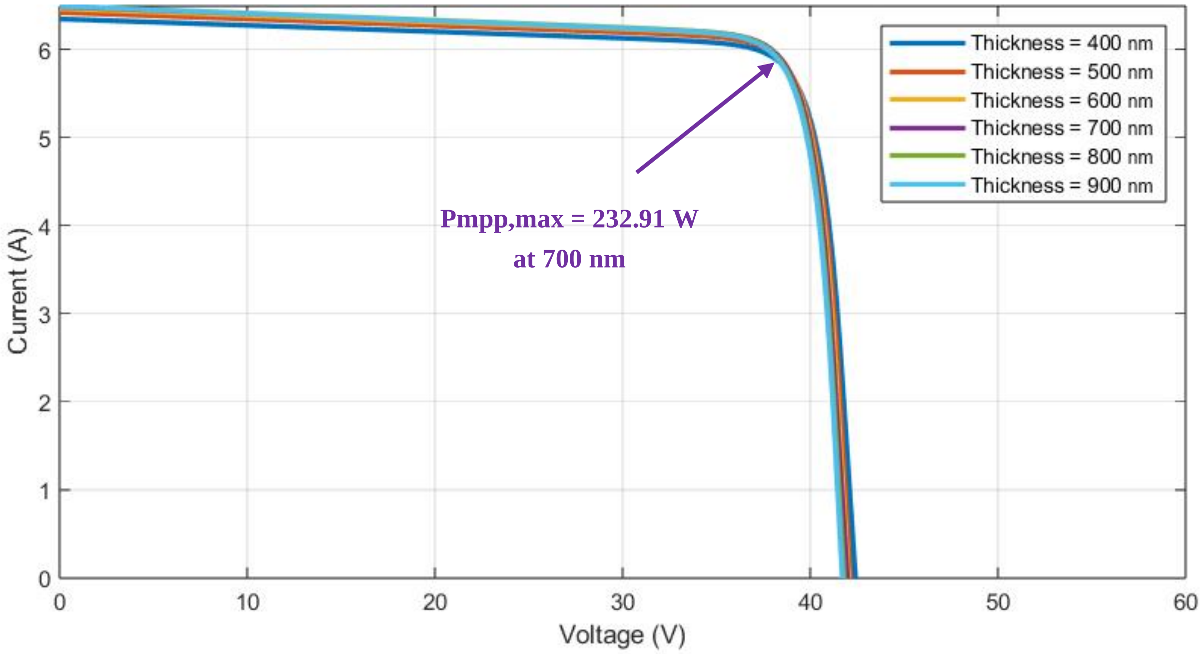

Figure 4.5 3T’s IV curves at various thicknesses at 1.64 eV

Each curve, represented by different colors, shows the variation in current and voltage characteristics with changing perovskite thickness. The data reveals that the maximum power point (Pmpp) is achieved at a perovskite thickness of 700 nm, with a value of 232.91 W. This indicates that at this specific thickness, the 3T tandem cell module operates at its peak efficiency. As the perovskite layer thickness increases from 400 nm to 700 nm, the IV curves show an improvement in performance, suggesting that thicker layers enhance the module's ability to generate higher current and voltage, thereby increasing the power output. However, beyond the 700 nm thickness, the performance does not exhibit significant improvement. This implies that there is an optimal thickness for maximum efficiency, and further increases in thickness beyond this point may not provide additional benefits.

A similar process was also done to plot the IV curves of both configurations at a perovskite bandgap energy of 1.82 eV. The results also show that a certain optimum thickness maximizes the energy yield and efficiency, with higher and lower thickness resulting in lower power.

In summary of this IV curves analysis, both 2T and 3T tandem cell modules have an optimal perovskite layer thickness that maximizes power output at the perovskite bandgap energy of 1.64 eV and 1.82 eV. For example, at a bandgap energy of 1.64 eV, the optimal thickness for the 2T module is 900 nm, while for the 3T module, it is 700 nm. Beyond these optimal points, increasing the thickness does not yield significant performance gains and may negatively affect the module's efficiency.

### 4.2.3 Energy yield vs perovskite's thickness

This subsection builds on the previous analysis of the IV curves for both 2T and 3T tandem cell modules, which highlighted the significance of perovskite layer thickness in optimizing power output. The analysis extends beyond the initial IV curves to evaluate the annual energy yield, with the goal of determining the optimal thickness that maximizes efficiency and energy yield. Additionally, the 3T configuration is compared with the 2T configuration to highlight energy yield and efficiency improvements. Figure 4.6 shows the comparison of 2T and 3T energy yield at bandgap energies of 1.64 eV and 1.82 eV

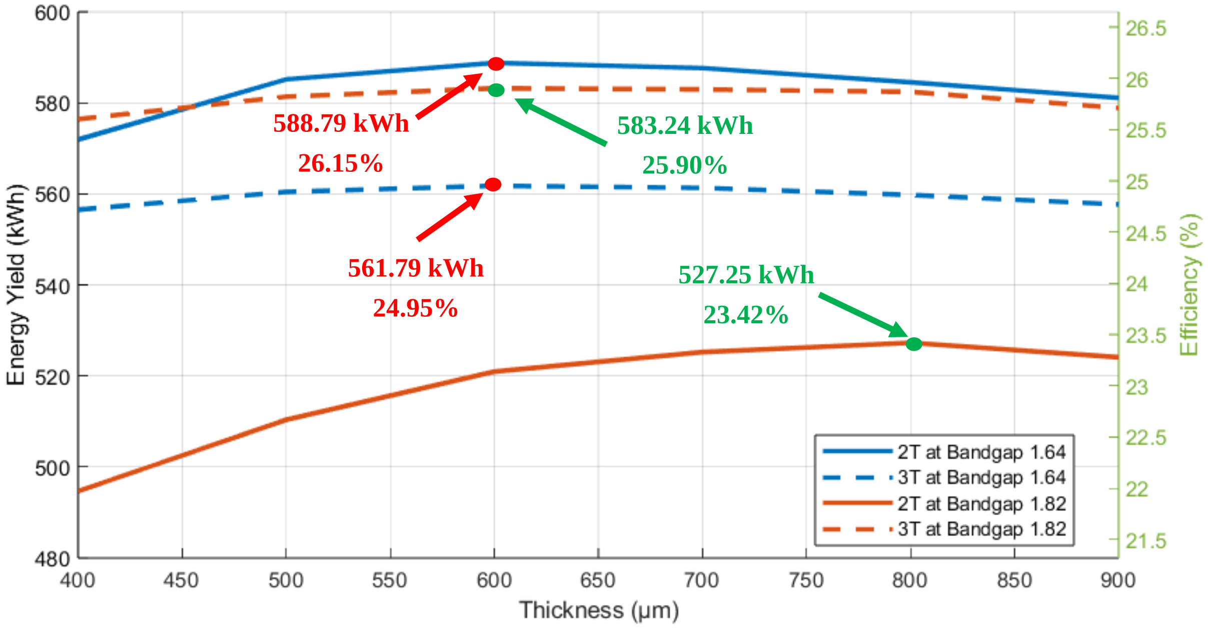

Figure 4.6 Energy yield vs thickness at perovskite bandgap of 1.64 eV

.

The graph illustrates the relationship between energy yield (measured in kWh) and the thickness of the material (measured in nm) for two different bandgap values, 1.64 eV and 1.82 eV, in both 2T and 3T configurations. The data are presented with solid lines for the 2T configurations and dashed lines for the 3T configurations, with each bandgap value represented by blue and orange colors. This visual distinction helps understand each configuration's performance and bandgap value across varying thicknesses.

For the bandgap value of 1.64 eV, the energy yield of 2T is higher than 3T. The red dots on the blue and blue-dashed lines show the peak graphs of both configurations. For the 2T configuration, the highest energy yield is 588.79 kWh at a thickness of 600 nm, which equals an efficiency of 26.15%. In contrast, the 3T configuration achieves its highest energy yield of 561.79 kWh at a thickness of 600 nm as well, resulting in an efficiency of 24.95%. This analysis suggests that the optimal thickness for maximizing energy yield and efficiency is around 600 nm for both the 2T and 3T configurations.

On the other hand, at the bandgap of 1.82 eV, 3T yields more energy than 2T. The green dots on the orange and orange-dashed lines show the peak graphs of both configurations. For the 2T configuration, the energy yield increases to 527.25 kWh at 800 nm, which is equal to an efficiency of 23.42 %. In contrast, the 3T configuration shows an optimum yield of 583.24 kWh, equivalent to 25.90% efficiency at 600 nm, then slightly decreasing. This data highlights that the 3T configuration consistently outperforms the 2T configuration in terms of energy yield and efficiency across all thicknesses at the thickness of 1.82 eV, with the optimal performance observed at 600 nm. The results demonstrate that the optimum thickness for 2T is 800 nm and 3T terminals is 600 nm.

## 4.3 Bandgap energy and thickness: 2T vs 3T

This section compares the combined effects of bandgap energy and thickness on the performance of 2T and 3T tandem modules. This comparison aims to highlight the advantages of the 3T configuration over the traditional 2T design, particularly in terms of optimizing these critical parameters.

### 4.3.1 Simulation setup

Both 2T and 3T modules are simulated with the same 2T optimized parameters tandem cell and geographic location as described in the previous sections. The simulation focuses on the perovskite layer, a critical component influencing the module's overall efficiency. The simulations are conducted over a comprehensive range of bandgaps and thicknesses to investigate the performance characteristics thoroughly. Specifically, the bandgap values will span from 1.50 eV to 1.86 eV, incrementing by 0.02 eV for each step. Concurrently, the thickness of the perovskite layer will vary from 400 nm to 900 nm in steps of 100 nm. These variations allow for a detailed analysis of how different material properties affect the performance of both 2T and 3T designs. By comparing the performance metrics, such as energy yield and efficiency for each configuration, the improvements and advantages of the 3T design over the traditional 2T design will be comprehensively assessed.

### 4.3.2 Energy yield and efficiency vs perovskite’s bandgap energy and thickness

This subsection presents the results from simulations of both 3T and 2T tandem solar module. It focuses on the impact of varying the perovskite layer's bandgap energy and thickness. The primary objective is to identify the optimal combination of bandgap energy and thickness that maximizes the solar modules' efficiency and energy yield. The annual energy yield of Delft over the range of perovskite’s bandgap energy for every thickness sample is presented in Figure 4.7 below.

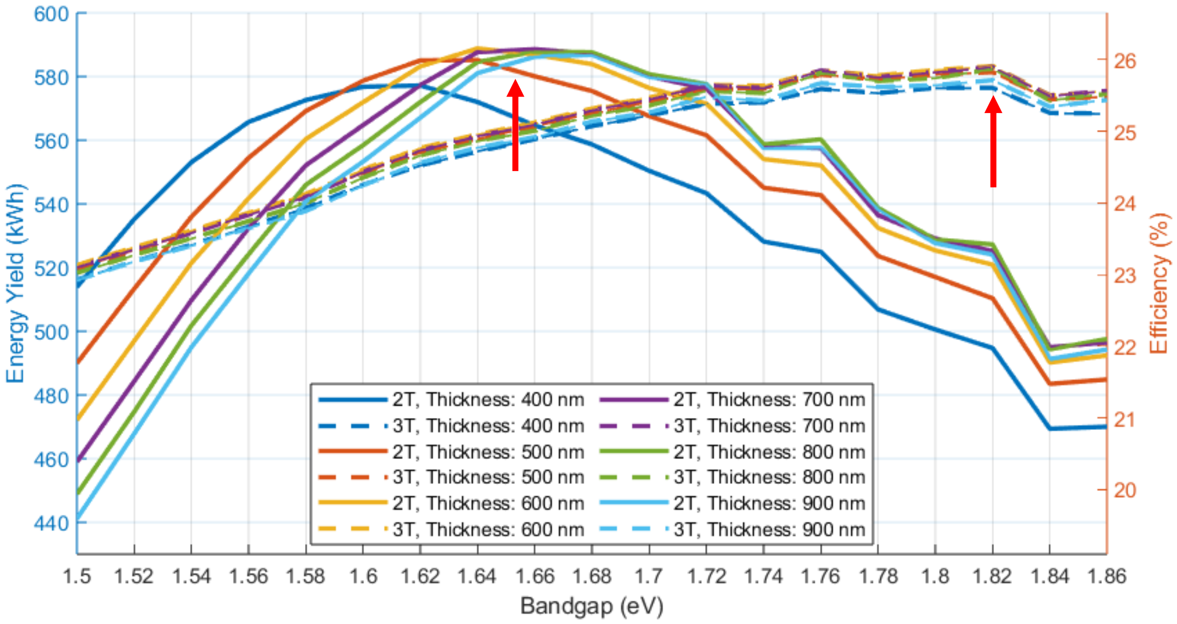

Figure 4.7 Energy yield vs perovskite's bandgap energy at every thickness sample

The graph depicts the relationship between the perovskite layer's bandgap energy (Eg) and the energy yield (in kWh) for both 2T and 3T tandem solar modules with varying perovskite thicknesses. The solid lines represent the energy yield for 2T configurations at thicknesses of 400 nm, 500 nm, 600 nm, 700 nm, 800 nm, and 900 nm with colors blue, red, yellow, purple, green, and light blue respectively, while the dashed lines represent the 3T configurations at the same thicknesses. A detailed examination of the graph reveals that the 3T configuration surpasses the 2T configuration in energy yield, particularly at higher bandgap values.

For each thickness examined, the 3T configuration exhibits an increase in energy yield over the 2T configuration at elevated bandgaps. This trend becomes particularly prominent as the bandgap exceeds approximately 1.68 eV. At these higher bandgap values, the 3T configuration not only yields more power but also shows a more stable performance compared to the 2T configuration, which tends to decline more sharply. Specifically, for a thickness of 400 nm, the energy yield for the 3T configuration becomes noticeably higher than that of the 2T configuration as the bandgap increases beyond 1.68 eV. This pattern is similarly observed for thicknesses from 500 nm to 900 nm, where the 3T configuration maintains a higher energy yield at higher bandgaps. The 3T configuration's superior performance is evident in the bandgap range from approximately 1.70 eV to 1.86 eV, where the energy yield remains higher than the 2T configuration. However, it is difficult to determine the optimum perovskite bandgap energy and thickness for 2T and 3T, which are shown by the red arrows in the above figure.

### 3T optimal bandgap and thickness

Examining the dashed lines shown in Figure 4.7, which correspond to the 3T configurations, reveals that the optimal bandgap energy for achieving the highest energy yield occurs at the peaks of these lines. Specifically, the peaks for the 3T configurations are consistently found at a bandgap energy of approximately 1.82 eV, regardless of the thickness of the solar cells. The purple and yellow dashed lines, representing the 3T configurations for 700 nm and 600 nm thicknesses, respectively, are almost identical at this bandgap energy. This indicates that the energy yields for these two thicknesses are very close to each other. Therefore, the optimum thickness for achieving the maximum energy yield in the 3T configuration lies between these two thicknesses. However, it is difficult to determine which thickness yields a slightly higher energy output just by looking at the graph, as the lines are very closely aligned. Thus, the detailed data in Table 19 below will show the optimum thickness at this bandgap energy.

Table 14 Energy yield at the respective thickness (3T)

| Thickness (nm) | Energy Yield (kWh) |
|---|---|
| 400 | 576.44 |
| 500 | 581.36 |
| 600 | 583.24 |
| 700 | 582.97 |
| 800 | 582.36 |
| 900 | 578.83 |

This table shows that the energy yield increases with thickness, reaching a peak at 600 nm with an energy yield of 583.24 kWh, which accounts for 25.90 % efficiency. At 700 nm, the energy yield is almost identical, slightly lower at 582.97 kWh. This indicates that the optimum thickness for the 3T configuration at a bandgap of 1.82 eV is approximately 600 nm. The energy yield does not significantly increase beyond this point, suggesting that increasing the thickness beyond 600 nm offers negligible improvement. The slight decrease at 700 nm confirms that 600 nm is the optimal thickness to achieve the highest energy yield. Therefore, Delft's optimum combination of bandgap and thickness is 1.82 eV and 600 nm, respectively.

### 2T optimal bandgap and thickness

With the same method used for 3T, the optimal bandgap and thickness for 2T can be obtained. The 2T energy yields are depicted by the solid lines presented in Figure 4.4. The graph shows that the energy yield increases with the bandgap up to a certain point, beyond which it starts to decrease. However, unlike the 3T configuration, which shows the optimal bandgap energy at 1.82 eV, the peak of the 2T configuration is somewhere around 1.64 to 1.68

eV bandgap energies. The peak energy yield at this range of bandgaps corresponds to different thicknesses from 600 nm to 900 nm. For instance, the 2T configuration with a thickness of 600 nm, shown by the solid yellow line, shows a peak energy yield close to 590 kWh at a bandgap of 1.64 eV. Similarly, other thicknesses exhibit their maximum energy yields within this bandgap range. Detailed data on the optimum bandgap and thickness for 2T are presented in Table 20 below.

Table 15 Energy yield at the respective thickness (2T)

| Thickness (nm) | Bandgap Energy (eV) | Energy Yield (kWh) |
|---|---|---|
| 500 | 1.64 | 585.15 |
| 600 | 1.64 | 588.79 |
| 700 | 1.66 | 588.56 |
| 800 | 1.68 | 587.79 |
| 900 | 1.68 | 586.77 |

The table shows that at a thickness of 600 nm, the maximum energy yield is 588.79 kWh, achieved at a bandgap energy of 1.64 eV. This data indicates that Delft's optimal bandgap energy and thickness combination for achieving the highest energy yields in the 2T configuration is 1.64 eV and 600 nm.

**2T vs 3T energy yields comparison**

After the optimum combinations are obtained for 2T and 3T to gain their highest energy yields, they can be compared to evaluate their performance. Table 21 below shows the data comparison.

Table 16 Comparison of 2T vs 3T energy yields and efficiency

| Configuration | Bandgap Energy (eV) | Thickness (nm) | Energy Yield (kWh) | Efficiency (%) |
|---|---|---|---|---|
| 2T | 1.64 | 600 | 588.79 | 26.15 |
| 3T | 1.82 | 600 | 583.24 | 25.90 |

Table 21 compares the energy yields and efficiency between 2T and 3T configurations. The table reveals that the 2T configuration, with a bandgap energy of 1.64 eV and a thickness of 600 nm, achieves an energy yield of 588.79 kWh and an efficiency of 26.15%. The results differ from Marrioti’s work [9] as their study was under STC. On the other hand, the 3T configuration, with a bandgap energy of 1.82 eV and a thickness of 600 nm, produces a slightly lower energy yield of 583.24 kWh and an efficiency of 25.90%. This comparison highlights that the 2T configuration provides a higher energy yield and exhibits better efficiency than the 3T configuration under the given conditions.

**Loss analysis**

The 3T has a higher energy yield than the 2T at higher perovskite bandgap energy due to the lesser losses it produces compared to lower bandgap energy. The power loss due to mismatch and end loss is shown in Table 17 below.

Table 17 Power loss distribution of 2T and 3T

| Bandgap Energy (eV) | Thickness (nm) | Configuration | Energy Mismatch Loss (kWh) | Energy End loss (kWh) | Total Energy Loss (kWh) |
|---|---|---|---|---|---|
| 164 | 600 | 2T | 5.56 | 0 | 5.56 |
| | | 3T | 16.28 | 16.05 | 32.33 |
| 182 | 600 | 2T | 82.82 | 0 | 82.82 |
| | | 3T | 3,67 | 16.67 | 20.34 |

The table shows the power loss distribution of 2T and 3T at their optimum perovskite bandgap energy and thickness. For the bandgap energy of 164 eV, the 2T configuration shows a power mismatch loss of 5.56 kWh, with no power end loss, resulting in a total power loss of 5.56 kWh. In contrast, the 3T configuration at the same bandgap energy incurs a higher power mismatch loss of 16.28 kWh and an additional power end loss of 16.05 kWh, culminating in a higher total power loss of 32.33 kWh.

At a higher bandgap energy of 182 eV, the 2T configuration experiences a significantly larger power mismatch loss of 82.82 kWh with no power end loss, making the total power loss 82.82 kWh. Conversely, the 3T configuration at this bandgap energy has a power mismatch loss of 3.67 kWh and a power end loss of 16.67 kWh, resulting in a less total power loss of 20.34 kWh. This comparison presents that the 3T yields less power loss at higher perovskite bandgap energy compared to the 2T.

## 4.4 Different climates

This section explains the optimum combination of bandgap and thickness that produces the highest energy yield of 2T and 3T modules using existing 2T and developed 3T models for each representative climate. The optimum bandgap and thickness for Delft, which represents a temperate low-irradiance climate, have been determined. The discussion will also identify the optimum values for the other three climates.

The process for obtaining the best combination is similar to the one used in the previous section. To simplify the discussion, the best combination of each location is presented in the Table 18 below.

Table 18 Comparison of 72-cell module energy yields and efficiencies of 2T and 3T

| Location | Configuration | Bandgap Energy (eV) | Thickness (nm) | Energy Yield (kWh) | Efficiency (%) |
|---|---|---|---|---|---|
| Delft | 2T | 1.64 | 600 | 588.79 | 26.15 |
| | 3T | 1.82 | 600 | 583.24 | 25.90 |
| Lisbon | 2T | 1.64 | 600 | 999.69 | 26.31 |
| | 3T | 1.82 | 700 | 993.36 | 26.15 |
| Lagos | 2T | 1.68 | 700 | 757.46 | 25.73 |
| | 3T | 1.82 | 700 | 752.62 | 25.56 |
| Shanghai | 2T | 1.68 | 800 | 665.57 | 26.13 |
| | 3T | 1.82 | 600 | 659.98 | 25.91 |

Table 22 presents a comparison of energy yields and efficiencies for 2T and 3T configurations at different locations: Delft, Lisbon, Lagos, and Shanghai. For each location, the table lists the optimal bandgap energy, thickness, energy yield, and efficiency for both configurations. . In Delft, the 2T configuration with a bandgap of 1.64 eV and thickness of 600 nm slightly outperforms the 3T setup, delivering higher energy yield and efficiency. Lisbon shows a similar trend, where the 2T configuration (1.64 eV, 600 nm) achieves marginally better energy yield and efficiency than the 3T counterpart. In Lagos, the 2T configuration (1.68 eV, 700 nm) also demonstrates higher energy yield and efficiency compared to the 3T configuration. Finally, in Shanghai, the 2T setup with a bandgap of 1.68 eV and a thickness of 800 nm produces a higher energy yield and efficiency than the 3T configuration.

The percentage gap between the 2T and 3T configurations at various locations indicates the relative performance difference in energy yield. In Delft, the 2T configuration yields 0.95% more energy than the 3T configuration, reflecting a slight efficiency advantage for the 2T setup. In Lisbon, the 2T configuration outperforms the 3T by 0.64%, again showing a marginal but notable improvement. Similarly, in Lagos, the 2T configuration yields 0.64% more energy than the 3T configuration, indicating a small, consistent advantage. In Shanghai, the 2T configuration yields 0.85% more energy than the 3T configuration. These consistent gaps, ranging from approximately 0.64% to 0.95%, underscore the 2T configuration's advantage in diverse environmental conditions.

## 4.5 Increased number of cell module

To further investigate the potential of the 3T configuration, we will explore its performance using a larger number of cells, specifically increasing from the previously 72-cell to 144-cell module. Note that the dimensions of a single tandem cell will not be changed. By transitioning to a 144-cell module, we aim to determine if the 3T configuration can surpass the power output of the 2T configuration. The simulation process is similar to the previous 72-cell module; in this case, only the number of cells will be increased. The optimum combination of perovskite's bandgap energy and thickness of the previous section will also be used to present a consistent comparison. To make it simple, the results of this 144-cell module are presented in Table 19 below.

Table 19 Comparison of 144-cell module energy yields and efficiencies of 2T and 3T

| Location | Configuration | Bandgap Energy (eV) | Thickness (nm) | Energy Yield (kWh) | Efficiency (%) |
|---|---|---|---|---|---|
| Delft | 2T | 1.64 | 600 | 1167.29 | 26.25 |
| | 3T | 1.82 | 600 | 1172.03 | 26.36 |
| Lisbon | 2T | 1.64 | 600 | 1991.10 | 26.43 |
| | 3T | 1.82 | 700 | 2006.17 | 26.63 |
| Lagos | 2T | 1.68 | 700 | 1507.03 | 25.83 |
| | 3T | 1.82 | 700 | 1519.08 | 26.04 |
| Shanghai | 2T | 1.68 | 800 | 1322.46 | 26.23 |
| | 3T | 1.82 | 600 | 1330.20 | 26.38 |

The table illustrates the energy yields and efficiencies of 144-cell modules for 2T and 3T configurations across four locations: Delft, Lisbon, Lagos, and Shanghai. With the module expansion to 144 cells, the 3T configuration consistently demonstrates higher energy yields compared to the 2T configuration.

In Delft, the energy yield gap between the 2T and 3T modules is relatively small, with the 3T configuration achieving approximately 0.41% more energy yield than the 2T configuration. In Lisbon, the 3T configuration significantly outperforms the 2T, yielding about 0.76% more energy, showcasing the considerable advantage of the 3T design in this location. In Lagos, the 3T configuration also yields more power, with an energy yield gap of approximately 0.80% over the 2T configuration. Similarly, in Shanghai, the 3T configuration achieves an energy yield gap of about 0.59% higher than the 2T configuration. This consistent trend across different locations indicates that with the increase in cell count to 144, the 3T configuration leverages its potential to yield more power than the 2T configuration, overcoming the inherent advantage of current matching seen in 2T designs.

### Loss analysis

This analysis explains why the 3T can yield more energy than 2T. The power loss from mismatches and end loss are detailed to see whether the losses increase or decrease. The location Delft is chosen as a sample to see this effect. The bandgap of 1.64 eV and 1.82 eV with a thickness of 600 nm, which are the perovskite's optimum bandgap and thickness, are chosen for this analysis. First, the loss analysis of 1.64 eV bandgap energy is detailed at Table 20 below.

Table 20 Comparison of increased cell module’s effect on the power loss at 1.64 eV

| Configuration | Number of cells | Energy mismatch loss (kWh) | Energy end loss (kWh) | Total power loss (kWh) |
|---|---|---|---|---|
| 2T | 72 cells | 5.56 | 0 | 5.56 |
|  | 144 cells | 11.10 | 0 | 11.10 |
| 3T | 72 cells | 16.28 | 16.05 | 32.33 |
|  | 144 cells | 32.26 | 15.92 | 48.18 |

The table shows the effect of increasing the number of cells from 72 to 144 at a perovskite bandgap of 1.64 eV. The mismatch loss is doubled when the number of cells is doubled for 2T and 3T. While for 2T, there is no end loss, for 3T, the end loss is decreased if the number of cells is increased. Then, the loss analysis of 1.82 eV bandgap energy is also presented at Table 21 below.

Table 21 Comparison of increased cell module’s effect on the power loss at 1.82 eV

| Configuration | Number of cells | Energy mismatch loss (kWh) | Energy end loss (kWh) | Total power loss (kWh) |
|---|---|---|---|---|
| 2T | 72 cells | 82.82 | 0 | 82.82 |
|  | 144 cells | 163.54 | 0 | 163.54 |
| 3T | 72 cells | 3.67 | 16.67 | 20.34 |
|  | 144 cells | 7.39 | 16.51 | 23.90 |

The table shows the effect of increasing the number of cells from 72 to 144 at a perovskite bandgap of 1.82 eV. Here, the mismatch loss is also doubled when the number of cells is doubled. However, the mismatch losses in this bandgap are much larger for 2T than those at 1.64 eV. On the contrary, the mismatch loss for 3T at 1.82 eV is smaller than the loss at 1.64 eV, while the mismatch loss is also doubled. For the end loss, the increased number of cells reduces it.

In conclusion, the previous two tables show that increasing the number of cells increases the mismatch loss for 2T and 3T. However, the end loss of 3T is reduced when the number of cells is increased. These results explain why 3T can yield more energy at a larger number of cells.

### IBC integration to the 3T module

The additional cost of integrating IBC into a 3T tandem cell, compared to a traditional 2T tandem cell, appears to be economically unjustifiable when evaluated solely based on the energy yield difference. The IBC, as the third contact, introduces an additional production and manufacturing cost, assumed to be \$0.3/W [56]. The 3T module with an estimated lifetime of 25 years [57] has an average power output of 257 W and yields 4.74 kWh higher energy compared to 2T, as seen in Table 19 at Delft, it translates to \$0.65/kWh gained. This cost far exceeds the Levelized Cost of Electricity (LCoE) for large PV systems, which is between \$0.029/kWh and \$0.073/kWh [58].

The current price of IBC solar cells, estimated at \$0.30/W [56], is expected to decrease further in the future due to several factors. As demand for high-efficiency solar cells grows, manufacturers are scaling up production, which leads to economies of scale and lower costs per unit [59]. Technological advancements are also making the manufacturing process more efficient and less expensive. Increased competition among manufacturers, such as Maxeon and LONGi, is driving innovation and cost reductions [60]. Additionally, the integration of IBC technology with other solar advancements like TOPCon and the "learning curve" effect—where production costs decrease with experience—are expected to contribute to further price reductions [61]. These combined factors suggest that the price of IBC cells will continue to decline, making them more accessible for widespread adoption

## 4.6 Conclusion

This chapter has addressed Sub-objective 3: Determine the parameters that optimize the energy yield of the three-terminal (3T) module. Through detailed simulations, the optimal perovskite bandgap energy and thickness for both the 2T and 3T modules were identified, highlighting the potential for efficiency improvements in the 3T design.

The first optimization involved varying the perovskite bandgap energy. For the 2T configuration, the optimal bandgap energy was determined to be 1.64 eV, yielding an energy output of 585.15 kWh and an efficiency of 25.99%. In contrast, the 3T configuration reached its optimal performance at a higher bandgap energy of 1.82 eV, with a slightly lower energy yield of 581.36 kWh and an efficiency of 25.82%. This suggests that while the 2T configuration is optimized for lower bandgap energy, the 3T configuration performs nearly as efficiently at higher bandgap energies, indicating a broader optimal range.

The second optimization focused on the perovskite layer's thickness. For the 2T module, the optimal thickness was found to be 600 nm, achieving an energy yield of 588.79 kWh and an efficiency of 26.15%. The optimal thickness for the 3T module was also 600 nm, yielding 583.24 kWh and an efficiency of 25.90%. This demonstrates that the optimal thickness for both configurations is similar, although the 3T module consistently benefits from independent cell optimization, resulting in comparable performance despite its higher bandgap energy.

A comparative analysis of 72-cell modules across different climates revealed that the 2T module generally outperforms the 3T module, achieving 0.64% to 0.95% higher energy yields. However, the 3T module showed significant promise, especially when scaled up to a larger number of cells. In simulations with a 144-cell module, the 3T module consistently achieved higher energy yields from 0.4% to 0.8% compared to 2T across all locations, including Delft, Lisbon, Lagos, and Shanghai. This indicates that the 3T module's potential advantages become more pronounced with increased cell count, as it has less end loss, overcoming the inherent limitations of the 2T design.

The additional cost of integrating IBC into the 3T module, estimated at \$0.3/W, is economically unjustifiable based solely on the energy yield difference, as it results in a much higher cost of \$0.65/kWh gained compared to the Levelized Cost of Electricity (LCoE) of around \$0.029/kWh to \$0.073/kWh. However, the price of IBC solar cells is expected to decrease in the future due to economies of scale, technological advancements, increased competition, and the integration of IBC with other solar technologies, making them more cost-effective over time.

In conclusion, the 3T module, with its ability to independently optimize cell performance, presents a compelling alternative to the traditional 2T module. While the 2T module currently demonstrates higher efficiency under optimal conditions, the flexibility and adaptability of the 3T module, particularly in larger-scale applications, suggest that they could surpass the 2T module in real-world conditions. Furthermore, the 3T technology with IBC will also reach a competitive price in the future. These findings underscore the importance of continued optimization and development of the 3T module to fully realize its potential in diverse environmental settings.

# CHAPTER 5
# CONCLUSION AND RECOMMENDATIONS

This final chapter provides the conclusion of the project and offers recommendations for future study. The conclusion will present the most important results, followed by recommendations, which include improvements to the developed model or toolbox, and new topics for future research not covered in this work due to time constraints.

## 5.1 Conclusion

This work presents a new comprehensive model for analyzing the energy yield of three-terminal (3T) perovskite/silicon tandem photovoltaic (PV) modules under various conditions. The model is integrated into the PVMD Toolbox and validated against existing literature and electrical simulation software. The model is used to calculate energy yields for different configurations and conditions, offering insights into optimizing 3T PV modules.

As stated in Section 1.6.2, the main goal of this thesis is:

**Optimization of three-terminal perovskite/silicon tandem module energy yield simulations in real-world conditions**

This goal is divided into three sub-goals, each building on the results of the previous sub-goals to achieve the main objective. Each sub-goal corresponds to a dedicated chapter in the thesis, ensuring a structured approach to tackling the main goal. The chapters are designed to methodically address the sub-goals through a combination of theoretical development, simulation, validation, and optimization processes.

### Sub-goal 1: Implement and validate the developed three-terminal (3T) model

Chapter 2 of the document focuses on implementing and validating a comprehensive three-terminal (3T) model for the PVMD Toolbox. Initially, the chapter discusses the importance of obtaining the IV curve and energy yield, which is crucial for evaluating the performance of photovoltaic cells. The chapter explains the theoretical background of the 3T configuration, highlighting its formula. This theoretical foundation is necessary to implement the developed 3T model, which aims to improve efficiency by addressing issues such as current matching and optical losses seen in 2T and 4T configurations.

The 3T configuration integrates a perovskite top cell with an interdigitated back contact (IBC) silicon bottom cell, allowing each sub-cell to operate independently without additional ITO layers. This setup mitigates current matching and optical loss issues, enhancing overall efficiency. Thus, this idea is formulated into equations to be implemented into the new developed 3T model. The chapter also explains how the 3T module's IV curves are obtained and further validated against existing literature and simulations using LTSpice.

Validation of the 3T model involves comparing the IV curves of individual top and bottom cells and a full 72-cell 3T module between the simulation results of developed 3T MATLAB and LTSpice models. The validation showed high accuracy, with an RMSE of 0.10146 W, meaning the errors were only about 0.02%. These numbers demonstrate that the MATLAB model accurately replicates the behavior predicted by LTSpice, confirming its reliability for further analysis and development. This successful validation addresses the initial sub-objective of the project, instilling confidence in the predictive capabilities of the new 3T model and setting a solid foundation for optimizing tandem solar cell technology

**Sub-objective 2: Analyze and compare the performance of the three-terminal (3T) module with the two-terminal (2T) module**

Chapter 3 of this thesis provides a comprehensive analysis of the simulation results for the developed three-terminal (3T) module, comparing its performance with the two-terminal (2T) module. The chapter begins by detailing the IV curve simulations under standard test conditions (STC), which include a light intensity of 1000 W/m², a cell temperature of 25°C, and an air mass of 1.5. These conditions are used to establish a benchmark for the performance of the 2T module, facilitating a direct comparison with the 3T module. The 2T module, which is simulated using the existing 2T model, serves as a foundational benchmark, with its performance metrics established through simulations that highlight its current and voltage characteristics. The 3T module with the same optimized 2T parameters is then simulated using the developed 3T model to ensure consistency and reliability in the comparison. The key findings indicate that the 2T module shows a higher power output of 517.14 W due to its optimized design, compared to the 3T module’s output of 490 W with 2T optimized parameters.

The chapter progresses to a detailed comparison of the 2T and 3T modules under real-world conditions, specifically analyzing their performance on January 20th at 15:00 in Delft, the Netherlands. These simulations account for lower solar irradiance typical of winter, providing a realistic assessment of the modules' effectiveness. The results indicate that at this sample hour, the 3T module operates more efficiently, producing 220.75 W with higher current and lower voltage, compared to the 2T module, which produces 219.10 W with higher voltage but lower current. This is further corroborated by the loss analysis, which shows that the 3T module, despite its end and mismatch losses, can potentially surpass the 2T module in real-world conditions. The 3T module's ability to optimize each cell independently allows for better performance in lower irradiance environments, demonstrating significant potential for real-world applications.

Finally, the chapter delved into energy yield simulations over an extended period, comparing the annual energy production of the 2T and 3T modules across various climates. The simulations included data from locations with different irradiance levels, such as Delft, Lisbon, Lagos, and Shanghai. The results showed that while the 2T module generally produces 5% to 6% higher annual energy yields, the 3T module has potential. The 3T module's independent cell optimization, combined with its ability to handle spectral irradiance variations and current mismatch, makes it a promising alternative for photovoltaic systems, especially in regions with fluctuating conditions.

Ultimately, the 2T module outperforms the 3T module under both STC and real-world conditions. However, the 3T module currently uses the 2T's optimized parameters (perovskite bandgap energy of 1.68 eV and 575 nm thickness), indicating that further optimization is needed for the 3T module to enhance its performance.

**Sub-objective 3: Determine the parameters that optimize the energy yield of the three-terminal (3T) module**

Chapter 4 of the thesis focuses on optimizing a three-terminal (3T) tandem solar cell module using a developed 3T model within the PVMD Toolbox to maximize energy yield. This involves varying the perovskite bandgap energies and the thickness of the layers. The chapter begins by discussing the simulation of different perovskite bandgap energies, ranging from 1.5 eV to 1.86 eV, to find the optimum value for the 3T module. It was found that for the 3T configuration, the energy yield remained stable and high over a broader range of bandgap energies compared to the two-terminal (2T) configuration, which peaked at 1.64 eV. The optimal bandgap energy for the 3T module was identified as 1.82 eV, yielding an energy output of 581.36 kWh with 25.82% efficiency.

The next part of the chapter examines the effect of varying the thickness of the perovskite layer, between 400 nm and 900 nm, on the performance of the 3T tandem module. Simulations showed that for a perovskite bandgap of 1.82 eV, the optimal thickness for maximum energy yield and efficiency in the 3T configuration was 600 nm. This thickness achieved an energy yield of 583.24 kWh with 25.90% efficiency, demonstrating that increasing the thickness beyond this point offers negligible improvements and can even lead to a slight decrease in performance. The optimal thickness for the 2T configuration was also identified as 600 nm at a bandgap of 1.64 eV, yielding 588.79 kWh and an efficiency of 26.15%.

The chapter concludes by comparing the performance of 2T and 3T modules in different climates and with a larger number of cell modules. In four locations, including Delft, Lisbon, Lagos, and Shanghai, the 2T module outperformed the 3T module, achieving 0.64% to 0.95% higher energy yield. However, when increasing the cell number to 144 cells, the 3T module consistently demonstrated higher energy yields of around 0.4% to 0.8% compared to the 2T module across all locations. This indicates that the 3T design's advantages become more significant with larger cell modules, potentially overcoming the inherent current-matching limitations of 2T designs. The additional \$0.3/W cost of integrating IBC into the 3T module is economically unjustifiable, as it leads to a higher cost of \$0.65/kWh gained, significantly exceeding the Levelized Cost of Electricity (LCoE) of \$0.029/kWh to \$0.073/kWh. However, future cost reductions in IBC solar cells are expected due to economies of scale, technological advancements, and increased competition, potentially making them more economically viable. This comprehensive analysis underscores the potential of the 3T module in optimizing solar cell performance, especially in larger-scale applications and in future development.

## 5.2 Recommendations

This section provides a series of recommendations based on the findings and analyses presented in this study. It will explain the most important recommendations for further developing the tandem cell model. First, the recommendations for the developed model will be explored. Second, the recommendations for the simulations will be explained.

### 5.2.1 Recommendations for the developed model

While the chapter outlines validations with existing literature and LTSpice simulations, incorporating real-world data from field tests would significantly strengthen the model's reliability. Real-world data would help verify the model's accuracy under practical operating conditions and provide insights into its performance over time.

Moreover, solar cells, especially perovskite cells, face degradation over time due to environmental factors. Integrating degradation models that predict performance decline over years would make the 3T model more robust and provide realistic long-term efficiency projections. Including degradation effects can help in designing maintenance schedules and forecasting the economic viability of the solar modules over their entire operational life.

Next recommendation is to integrate a detailed sensitivity analysis to understand how variations in key parameters (e.g., perovskite bandgap energy, cell thickness, temperature, irradiance) affect the overall performance. This will help in pinpointing the most critical factors influencing energy yield and guiding future optimizations. Sensitivity analysis can reveal potential areas for improvement and highlight the robustness of the model under different conditions.

Finally, explore the integration of the 3T model with smart grid technologies. This includes assessing how the model can support grid stability, load balancing, and integration with energy storage systems. Smart grid compatibility will enhance the model's appeal to modern energy systems that require flexible and reliable power sources.

### 5.2.2 Recommendations for simulations

To conduct simulations effectively, it is crucial that the tandem cell or any other photovoltaic technology is accurately represented by a detailed model. A more intricate solar cell model can simulate the complexities and nuances of advanced solar cell technology with greater precision. Such a model should account for various factors that influence the cell's performance, including material properties, layer thicknesses, and the electrical and optical behaviors of each layer.

Simulating complex models like the 3T configuration requires substantial computational power. Using high-performance computing (HPC) resources can significantly reduce simulation time and increase the resolution of the simulations. HPC allows for running multiple simulations in parallel, which is particularly useful for parameter sweeps and sensitivity analyses. This can lead to a more thorough exploration of the parameter space and identification of optimal configurations.

Regularly validate simulation results with experimental data to ensure accuracy. This involves comparing simulated IV curves, efficiency metrics, and thermal behavior with measurements from real-world prototypes. Validation builds confidence in the simulation model and helps in identifying any discrepancies that need to be addressed.

Detail the loss analysis of the 3T. The current study assumes that the module has no interconnection resistance. By incorporating thorough loss analysis, the optimal parameters for 3T can be determined accurately.

While the 3T solar technology offers promising energy yield and efficiency, its increased complexity leads to significant economic challenges. The need for additional electrical connections and a third contact raises material and manufacturing costs, requiring more sophisticated and costly production processes. The use of advanced technologies like IBC cells, crucial for optimizing 3T performance, further escalates costs due to their intricate design. A detailed economic analysis is needed to assess the financial viability of 3T technology, considering both upfront costs and potential long-term savings from technological advancements and economies of scale.

# APPENDIX

## A.1 IV curve and energy yield calculations

The IV curve is generated using the Lambert (W) function that solves Equation A.1.

$$W \cdot e^{W} = \mathrm{z} \tag{A.1}$$

Where z is a complex number [62] the current and voltage can be explicitly expressed using the W-function as follows (, 2016):

$$I(V) = -\frac{V}{R_s + R_{sh}} - \frac{n \cdot V_{th} \cdot W}{R_s}\left(\frac{R_s \cdot I_o \cdot R_{sh} \cdot e^{\left(\frac{R_{sh}\left(R_S \cdot I_{ph+} R_S \cdot I_{o+V}\right)}{n \cdot V_{th}\left(R_{S+} R_{sh}\right)}\right)}}{n \cdot V_{th}\left(R_{s+} R_{sh}\right)}\right) + \frac{R_{sh}\left(I_{ph+} I_{o\cdot}\right)}{R_{s+} R_{sh}} \tag{A.2}$$

And,

$$V(I) = -I \cdot R_s - I \cdot R_{sh} + I_{ph} \cdot R_{sh} - n \cdot V_{th} \cdot W\left(\frac{I_o \cdot R_{sh} \cdot e^{\left(\frac{R_{sh}\left(-I + I_{ph+} I_o\right)}{n \cdot V_{th}}\right)}}{n \cdot V_{th}}\right) + I_o \cdot R_{sh} \tag{A.3}$$

After the values of currents and voltages are obtained, the output power can be expressed explicitly as follows:

$$P = V \cdot I \tag{A.4}$$

Furthermore, the maximum power ($P_{mpp}$) output can be obtained by getting the maximum power point current ($I_{mpp}$) and the maximum power point voltage ($V_{mpp}$). Equation A.5 below shows the equation to obtain both parameters.

$$I_{mpp} = \frac{\partial P}{\partial I} \quad ; \quad V_{mpp} = \frac{\partial P}{\partial V} \tag{A.5}$$

The energy yield (E) can be obtained by multiplying each power output (P) by its respective hours (t), as shown by Equation A.6 below.

$$E(t) = \int P(t) \cdot dt \tag{A.6}$$

## A.2 Different tandem cell configurations

Solar cells are often represented by equivalent circuits, as shown in Figure 1.4, due to their electrical behavior. However, to make the explanation simpler, a single cell will be represented by a single diode. A diode representation can be seen in Figure A.0.1 below.

Figure A.0.1 Diode representation of a single-cell

### 2T Configuration

In a 2T tandem cell configuration, two or more sub-cells are connected in series within the same encapsulation. The 2T configuration can be seen in Figure A.0.2 below.

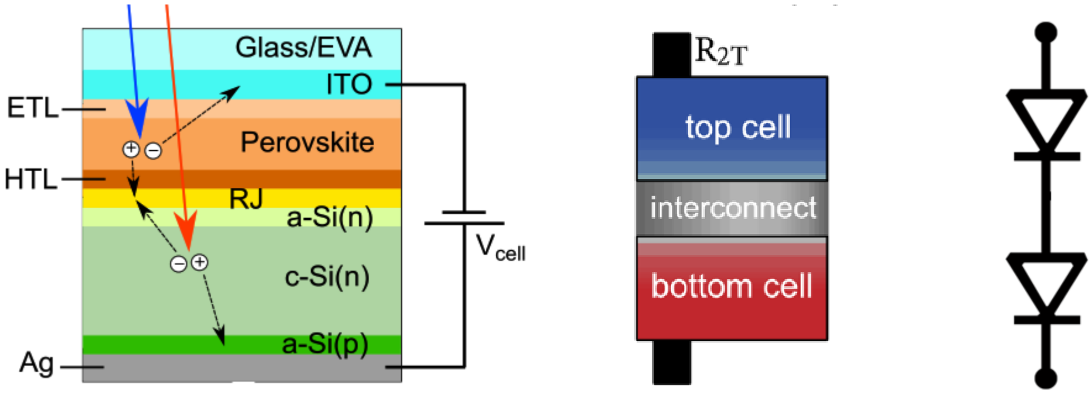

(a) (b) (c)

Figure A.0.2 2T configuration (a) schematic cross-section [13](b) schematic illustration [46] (c) diode representation

Figure A.0.2 illustrates the 2T solar cell configuration through three representations. Figure A.2(a) shows a schematic cross-section detailing the layers, including the Glass/EVA, ITO, ETL, HTL, Perovskite, recombination junction, amorphous and crystalline silicon layers, and the Ag back contact [13].To understand this configuration, this schematic cross-section is translated into a simplified schematic illustration, presented in Figure A.2(b), highlighting the top cell, interconnect or junction, and bottom cell [46].

This tandem cell is then connected with the other tandem cells to form a tandem module. The 2T tandem module example, which consists of three tandem cells, is depicted in Figure A.0.3 below.

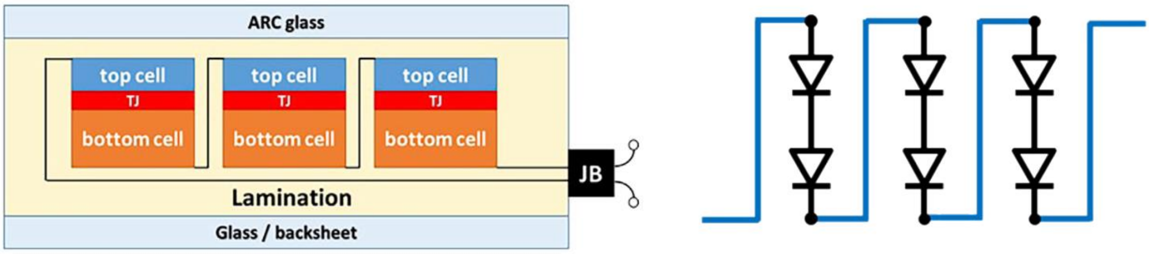

(a) (b)

Figure A.0.3 2T Tandem Module (a) schematic illustration [48] (b) diode representation [49]

To calculate the voltage and current outputs of this module, Equation A.8 explains them.

$$I_{module} = I_{out} = I_{min} \qquad ; \qquad V_{module} = n_{cell\cdot}\left(V_{top} + V_{bot}\right) \tag{A.8}$$

## B.1 Equivalent circuit of 3T tandem cell

The equivalent circuit of 3T is shown Figure B.1 below.

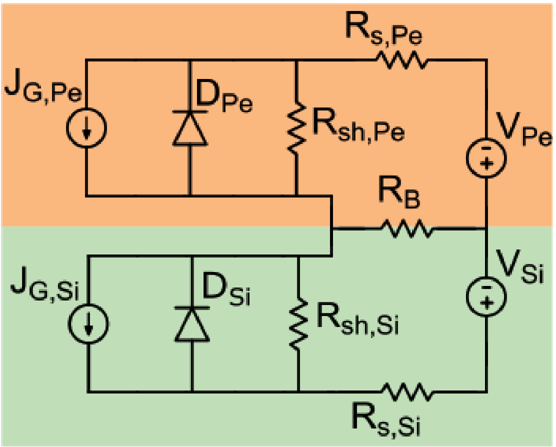

Figure B.1 Equivalent Circuit of 3T configuration [13]

Figure B. depicts an equivalent circuit model of a 3T tandem cell, consisting of a perovskite top cell and a silicon bottom cell. Each cell is represented by a current source ($J_G$), a diode ($D$), a shunt resistance ($R_{sh}$), and a series resistance ($R_s$). Additionally, there is resistance ($R_B$) between the two-subcells, often representing a shared junction or interface resistance and the voltage output ($V$) of each subcell with both cells sharing a common terminal. Based on this equivalent circuit by [13] the model for the LTSpice can be built. Figure B. below is the building of the equivalent circuit of the LTSpice.

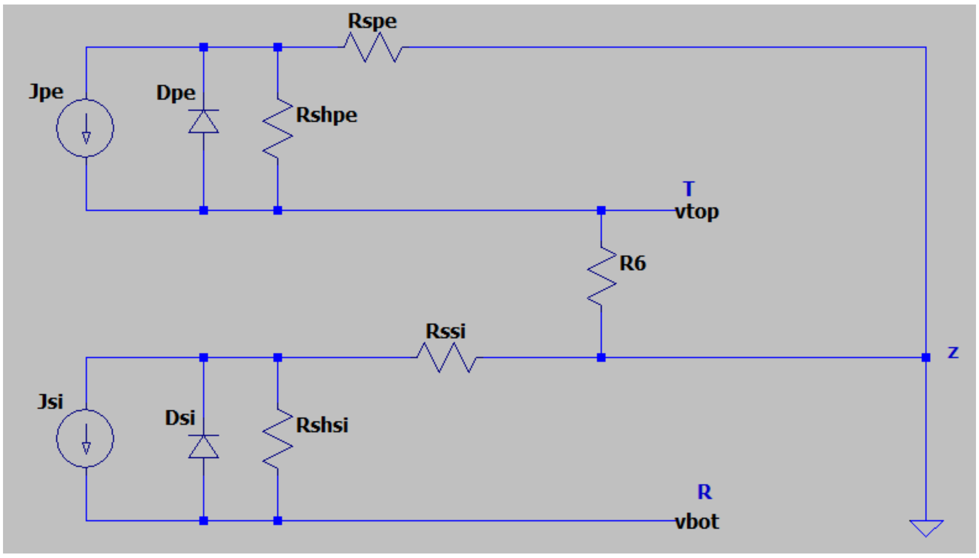

Figure B.2 LTspice model for 3T tandem cell

## C.1 Annual energy yields for different locations

Figures C. 1, C. 2, and C. 3 below show the annual energy yields at the other 3 locations. Each location has its own incident power, 2T and 3T energy yields as represented by yellow red-lined, green lined, and blue lined areas, respectively. The times when 3T yields more energy than 2T are shown by the red dot.

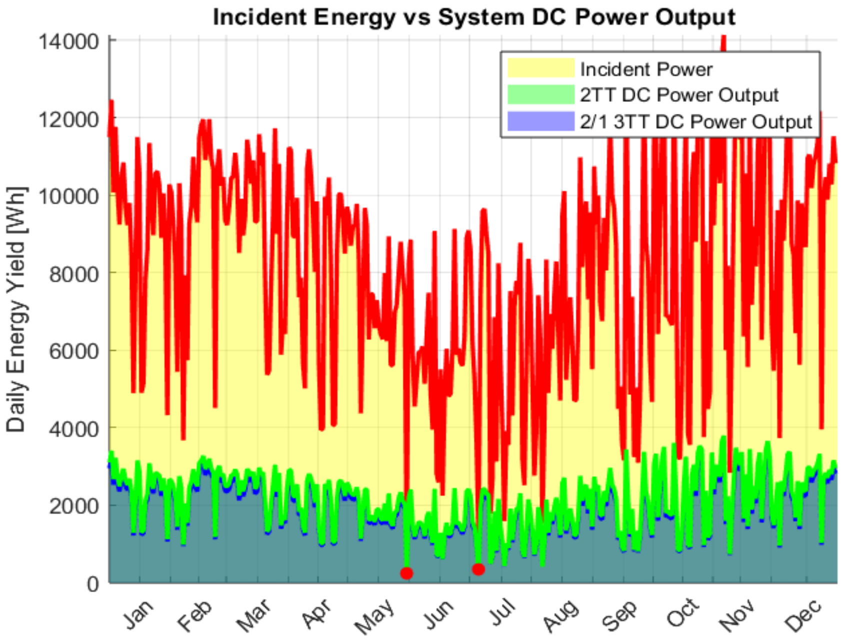

Figure C.1 Incident energy vs DC power outputs (2T and 3T) at Lagos

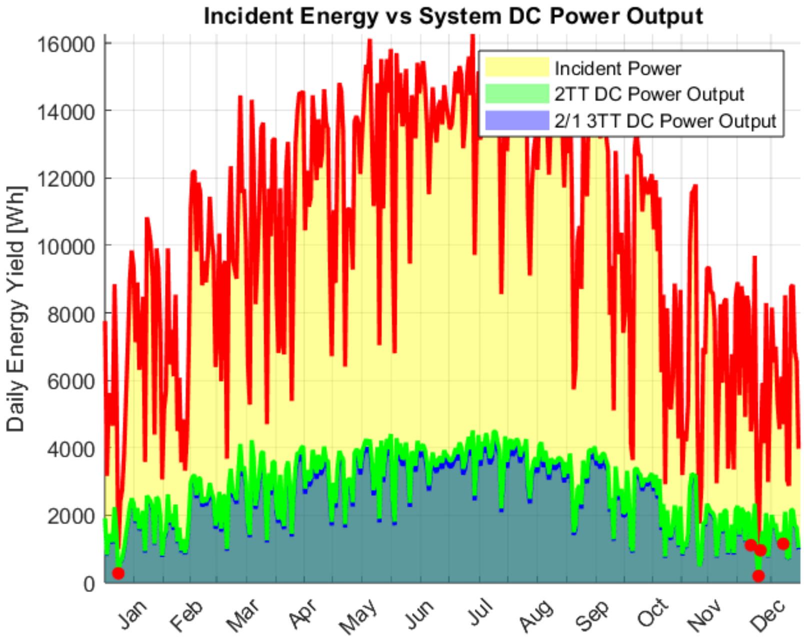

Figure C.2 Incident energy vs DC power outputs (2T and 3T) at Lisbon

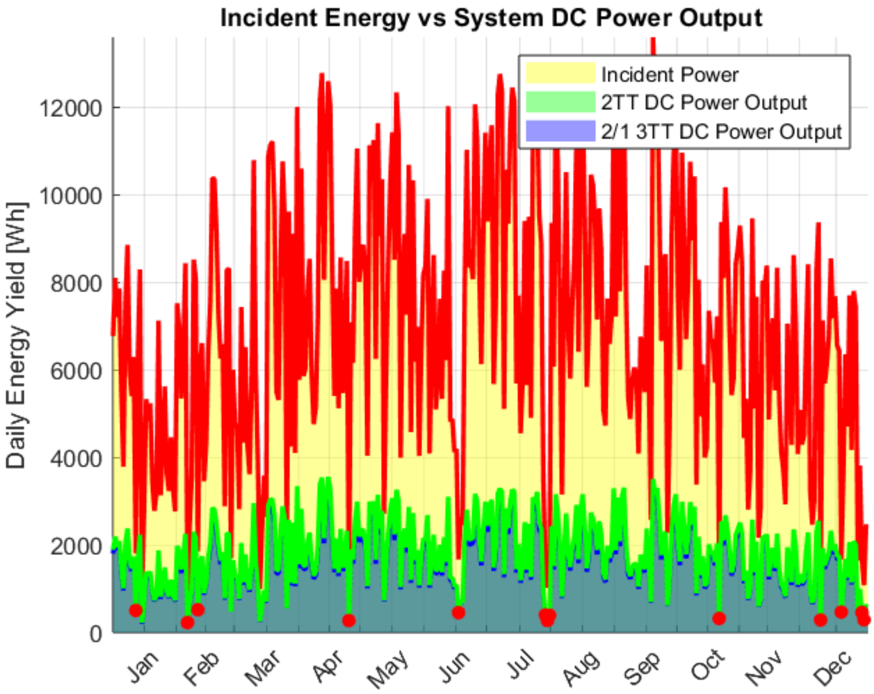

Figure C.3 Incident energy vs DC power outputs (2T and 3T) at Shanghai

## D.1 Energy yield vs perovskite bandgap energy

The annual energy yield plots of the other three locations over the range of perovskite's bandgap energy for all thickness samples are presented in Figure 4.7 D.1 to D.3 below.

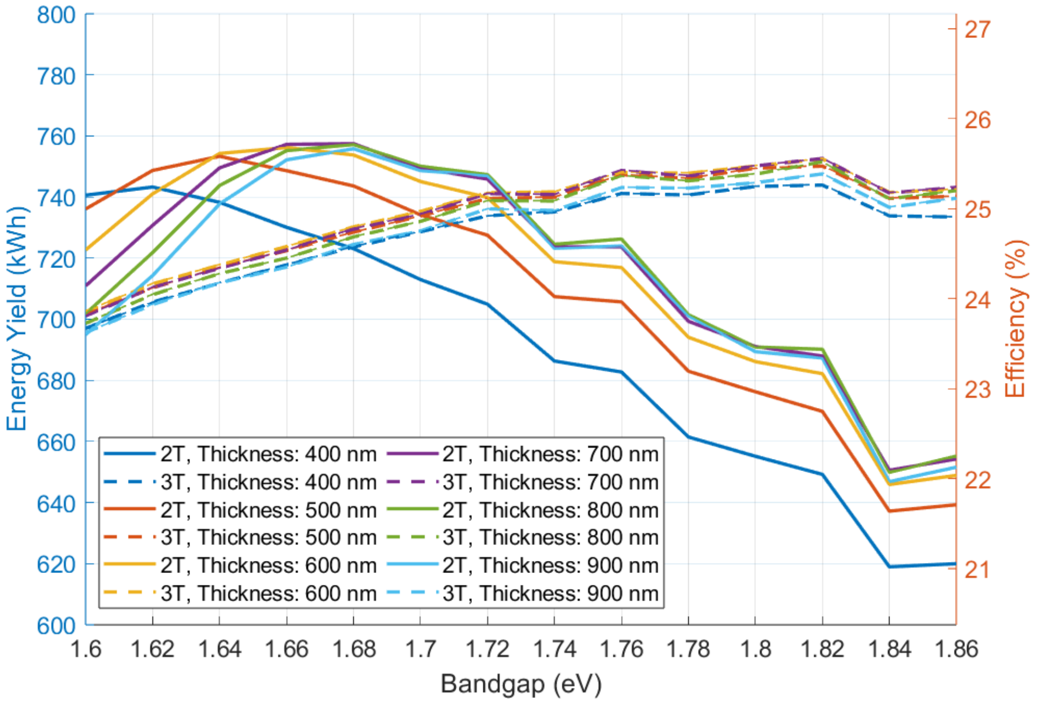

Figure D.1 Energy yield vs perovskite's bandgap energy at Shanghai

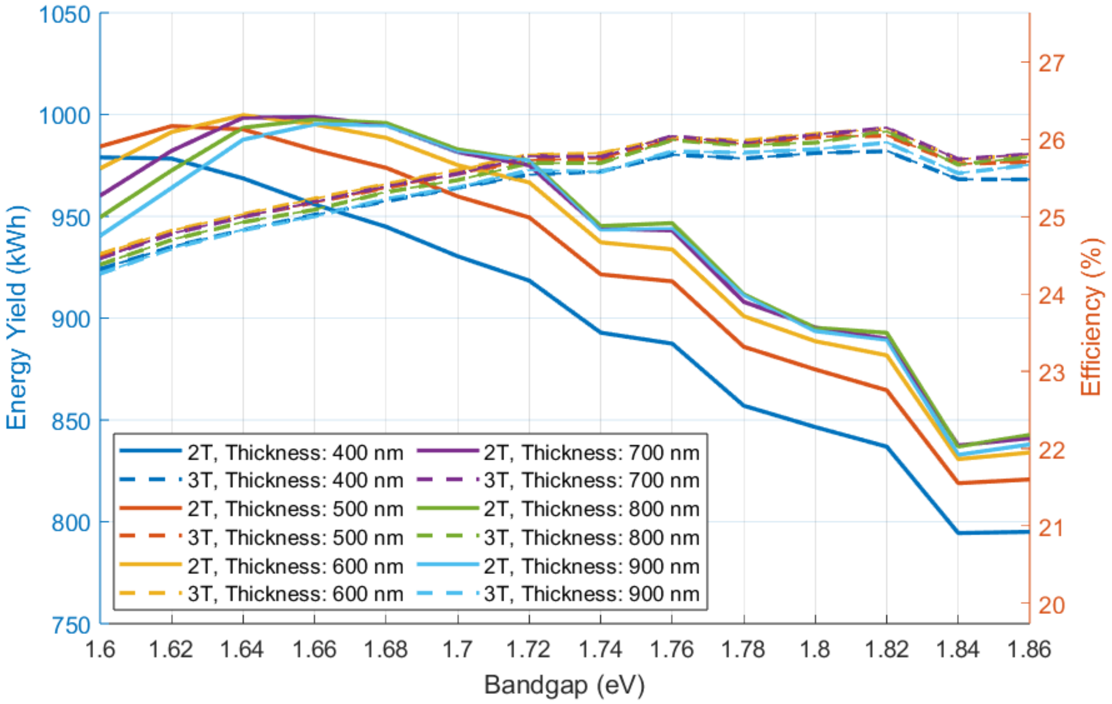

Figure D.2 Energy yield vs perovskite's bandgap energy at Lisbon

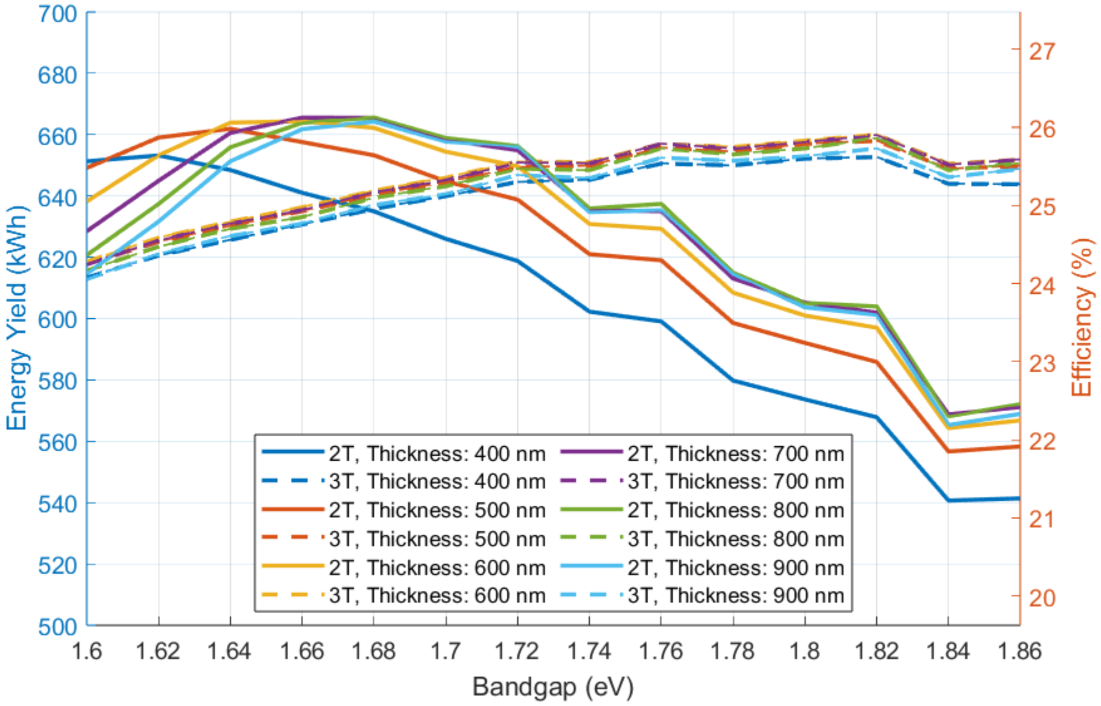

Figure D.3 Energy yield vs perovskite’s bandgap energy at Lisbon

## E.1 Flowchart of the 3T model implementation

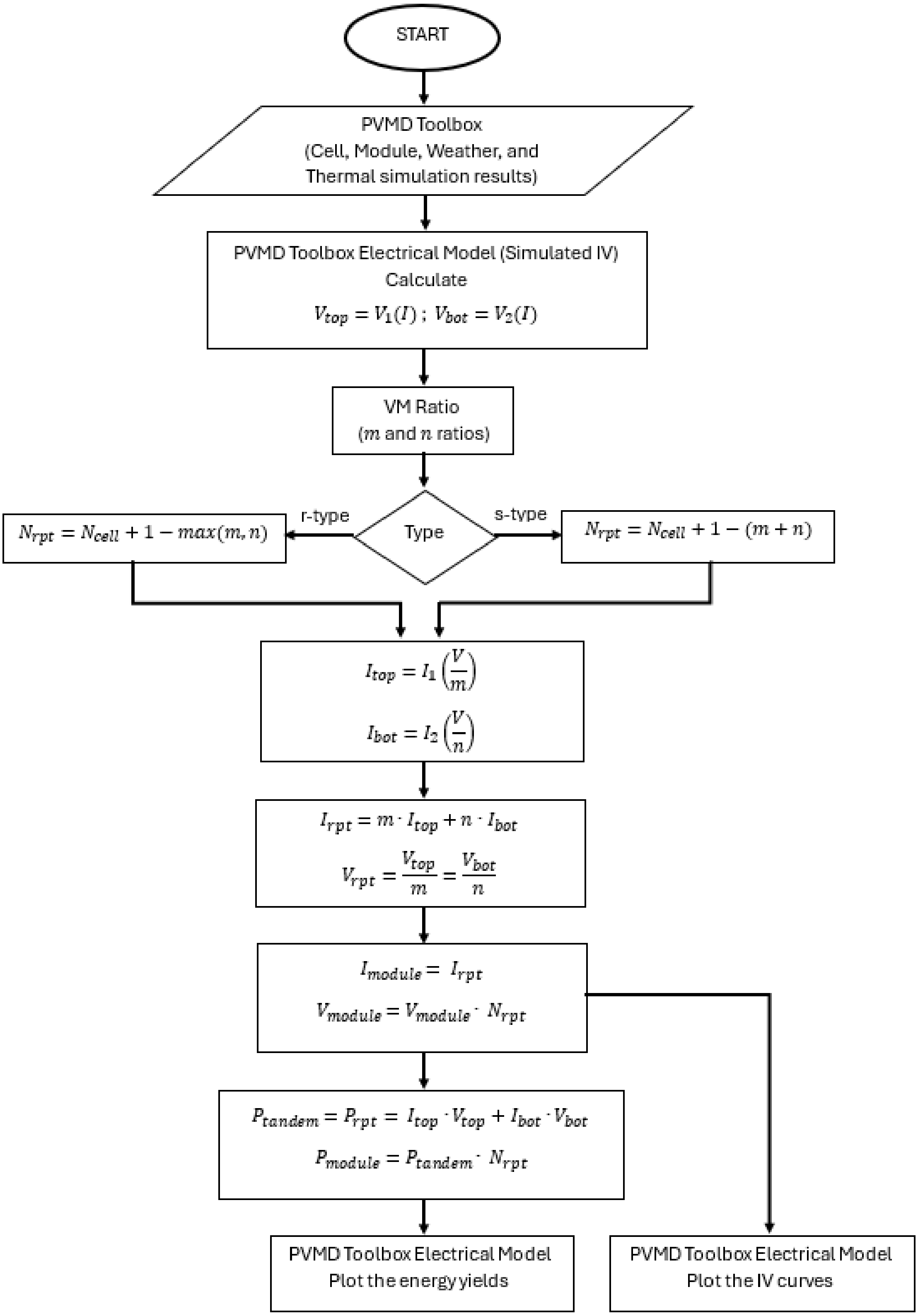

Figure E.1 New developed 3T model flowchart

# REFERENCES

[1] B. McCarthy, L. Eagle, and A. Osmond, “Electricity consumers in regional Australia: Social acceptance of coal-fired power and renewable energy,” *Soc. Bus.*, vol. 8, no. 3, pp. 253–275, Nov. 2018, doi: 10.1362/204440818X15434305418605.

[2] C.-F. Schleussner *et al.*, “Differential climate impacts for policy-relevant limits to global warming: the case of 1.5 °C and 2 °C,” *Earth Syst. Dyn.*, vol. 7, no. 2, pp. 327–351, Apr. 2016, doi: 10.5194/esd-7-327-2016.

[3] S. A. R. Khan, Y. Zhang, A. Kumar, E. Zavadskas, and D. Streimikiene, “Measuring the impact of renewable energy, public health expenditure, logistics, and environmental performance on sustainable economic growth,” *Sustain. Dev.*, vol. 28, no. 4, pp. 833–843, Jul. 2020, doi: 10.1002/sd.2034.

[4] S. Yekinni, I. Asiata, O. Hakeem, and L. Mubarak, “Solar Photovoltaic Energy System,” in *Nanogenerators and Self-Powered Systems*, B. Dudem, V. Venkateswaran, and A. Chandrasekhar, Eds., IntechOpen, 2023. doi: 10.5772/intechopen.108958.

[5] A. Richter, M. Hermle, and S. W. Glunz, “Reassessment of the Limiting Efficiency for Crystalline Silicon Solar Cells,” *IEEE J. Photovolt.*, vol. 3, no. 4, pp. 1184–1191, Oct. 2013, doi: 10.1109/JPHOTOV.2013.2270351.

[6] J. Werner *et al.*, “Efficient Monolithic Perovskite/Silicon Tandem Solar Cell with Cell Area >1 cm $^2$,” *J. Phys. Chem. Lett.*, vol. 7, no. 1, pp. 161–166, Jan. 2016, doi: 10.1021/acs.jpclett.5b02686.

[7] E. Aydin *et al.*, “Interplay between temperature and bandgap energies on the outdoor performance of perovskite/silicon tandem solar cells,” *Nat. Energy*, vol. 5, no. 11, pp. 851–859, Sep. 2020, doi: 10.1038/s41560-020-00687-4.

[8] L. Mao *et al.*, “Fully Textured, Production-Line Compatible Monolithic Perovskite/Silicon Tandem Solar Cells Approaching 29% Efficiency,” *Adv. Mater.*, vol. 34, no. 40, p. 2206193, Oct. 2022, doi: 10.1002/adma.202206193.

[9] S. Mariotti *et al.*, “Interface engineering for high-performance, triple-halide perovskite–silicon tandem solar cells,” *Science*, vol. 381, no. 6653, pp. 63–69, Jul. 2023, doi: 10.1126/science.adf5872.

[10] M. Rienacker, E. L. Warren, T. F. Wietler, P. Stradins, A. C. Tamboli, and R. Peibst, “Three-Terminal Bipolar Junction Bottom Cell as Simple as PERC: Towards Lean Tandem Cell Processing,” in *2019 IEEE 46th Photovoltaic Specialists Conference (PVSC)*, Chicago, IL, USA: IEEE, Jun. 2019, pp. 2169–2175. doi: 10.1109/PVSC40753.2019.8980645.

[11] R. Santbergen, H. Uzu, K. Yamamoto, and M. Zeman, “Optimization of Three-Terminal Perovskite/Silicon Tandem Solar Cells,” *IEEE J. Photovolt.*, vol. 9, no. 2, pp. 446–451, Mar. 2019, doi: 10.1109/JPHOTOV.2018.2888832.

[12] E. L. Warren *et al.*, “A Taxonomy for Three-Terminal Tandem Solar Cells,” *ACS Energy Lett.*, vol. 5, no. 4, pp. 1233–1242, Apr. 2020, doi: 10.1021/acsenergylett.0c00068.

[13] F. Gota, M. Langenhorst, R. Schmager, J. Lehr, and U. W. Paetzold, “Energy Yield Advantages of Three-Terminal Perovskite-Silicon Tandem Photovoltaics,” *Joule*, vol. 4, no. 11, pp. 2387–2403, Nov. 2020, doi: 10.1016/j.joule.2020.08.021.

[14] R. Eke, T. R. Betts, and R. Gottschalg, “Spectral irradiance effects on the outdoor performance of photovoltaic modules,” *Renew. Sustain. Energy Rev.*, vol. 69, pp. 429–434, Mar. 2017, doi: 10.1016/j.rser.2016.10.062.

[15] M. De Bastiani *et al.*, “Efficient bifacial monolithic perovskite/silicon tandem solar cells via bandgap engineering,” *Nat. Energy*, vol. 6, no. 2, pp. 167–175, Jan. 2021, doi: 10.1038/s41560-020-00756-8.

[16] G. M. Wilson *et al.*, “The 2020 photovoltaic technologies roadmap,” *J. Phys. Appl. Phys.*, vol. 53, no. 49, p. 493001, Dec. 2020, doi: 10.1088/1361-6463/ab9c6a.

[17] M. R. Vogt *et al.*, “Introducing a comprehensive physics-based modelling framework for tandem and other PV systems,” *Sol. Energy Mater. Sol. Cells*, vol. 247, p. 111944, Oct. 2022, doi: 10.1016/j.solmat.2022.111944.

[18] S. Ashok, “solar energy,” *Encyclopedia Britannica*. Accessed: Jul. 27, 2024. [Online]. Available: https://www.britannica.com/science/solar-energy

[19] F. Creutzig, P. Agoston, J. C. Goldschmidt, G. Luderer, G. Nemet, and R. C. Pietzcker, “The underestimated potential of solar energy to mitigate climate change,” *Nat. Energy*, vol. 2, no. 9, p. 17140, Aug. 2017, doi: 10.1038/nenergy.2017.140.

[20] B. F. Towler, “Solar Power,” in *The Future of Energy*, Elsevier, 2014, pp. 161–185. doi: 10.1016/B978-0-12-801027-3.00008-7.

[21] “Global primary energy consumption 2023,” Statista. Accessed: Jul. 28, 2024. [Online]. Available: https://www.statista.com/statistics/265598/consumption-of-primary-energy-worldwide/

[22] “Reference Air Mass 1.5 Spectra.” Accessed: Jul. 28, 2024. [Online]. Available: https://www.nrel.gov/grid/solar-resource/spectra-am1.5.html

[23] Y. Blom, “Energy loss analysis of tandem PV modules under realistic operating conditions,” Delft University of Technology, 2022. [Online]. Available: https://repository.tudelft.nl/record/uuid:92c54633-57d0-4aee-9a53-794159484500

[24] A. Smets, K. Jäger, O. Isabella, R. van Swaaij, and M. Zeman, *Solar Energy: The Physics and Engineering of Photovoltaic Conversion, Technologies and Systems*. Cambridge: UIT Cambridge Ltd, 2016.

[25] D. A. Neamen, *Semiconductor physics and devices: basic principles*, 4th ed. New York, NY: McGraw-Hill, 2012.

[26] “How a Solar Cell Works,” American Chemical Society. Accessed: Jul. 28, 2024. [Online]. Available: https://www.acs.org/education/resources/highschool/chemmatters/past-issues/archive-2013-2014/how-a-solar-cell-works.html

[27] Lindholm, J. G. Fossum, and E. L. Burgess, “Application of the superposition principle to solar-cell analysis,” *IEEE Trans. Electron Devices*, vol. 26, pp. 165–171, 1979.

[28] Alexis De Vos, “The fill factor of a solar cell from a mathematical point of view,” *Sol. Cells*, vol. 8, no. 3, pp. 283–296, Apr. 1983, doi: 10.1016/0379-6787(83)90067-4.

[29] J. Cubas, S. Pindado, and C. De Manuel, “Explicit Expressions for Solar Panel Equivalent Circuit Parameters Based on Analytical Formulation and the Lambert W-Function,” *Energies*, vol. 7, no. 7, pp. 4098–4115, Jun. 2014, doi: 10.3390/en7074098.

[30] A. Al-Ashouri *et al.*, “Monolithic perovskite/silicon tandem solar cell with >29% efficiency by enhanced hole extraction,” *Science*, vol. 370, no. 6522, pp. 1300–1309, Dec. 2020, doi: 10.1126/science.abd4016.

[31] F. Sahli *et al.*, “Fully textured monolithic perovskite/silicon tandem solar cells with 25.2% power conversion efficiency,” *Nat. Mater.*, vol. 17, no. 9, pp. 820–826, Sep. 2018, doi: 10.1038/s41563-018-0115-4.

[32] Y. Cheng and L. Ding, “Perovskite/Si tandem solar cells: Fundamentals, advances, challenges, and novel applications,” *SusMat*, vol. 1, no. 3, pp. 324–344, Sep. 2021, doi: 10.1002/sus2.25.

[33] C. Ashworth, “Interrogating the interphase,” *Nat. Rev. Mater.*, vol. 3, no. 5, pp. 1–1, Apr. 2018, doi: 10.1038/s41578-018-0013-z.

[34] B. Chen *et al.*, “Grain Engineering for Perovskite/Silicon Monolithic Tandem Solar Cells with Efficiency of 25.4%,” *Joule*, vol. 3, no. 1, pp. 177–190, Jan. 2019, doi: 10.1016/j.joule.2018.10.003.

[35] E. Köhnen *et al.*, “Highly efficient monolithic perovskite silicon tandem solar cells: analyzing the influence of current mismatch on device performance,” *Sustain. Energy Fuels*, vol. 3, no. 8, pp. 1995–2005, 2019, doi: 10.1039/C9SE00120D.

[36] S. Han *et al.*, “Integration of Subcells in III-V//Si Tandem Solar Cells,” *Trans. Electr. Electron. Mater.*, vol. 24, no. 2, pp. 132–139, Apr. 2023, doi: 10.1007/s42341-023-00430-2.

[37] E. Warren *et al.*, “Operating principles of three-terminal solar cells,” in *2018 IEEE 7th World Conference on Photovoltaic Energy Conversion (WCPEC) (A Joint Conference of 45th IEEE PVSC, 28th PVSEC & 34th EU PVSEC)*, Waikoloa Village, HI: IEEE, Jun. 2018, pp. 2648–2650. doi: 10.1109/PVSC.2018.8547611.

[38] R. Santbergen, T. Meguro, T. Suezaki, G. Koizumi, K. Yamamoto, and M. Zeman, “GenPro4 Optical Model for Solar Cell Simulation and Its Application to Multijunction Solar Cells,” *IEEE J. Photovolt.*, vol. 7, no. 3, pp. 919–926, May 2017, doi: 10.1109/JPHOTOV.2017.2669640.

[39] R. Siegel, “Net radiation method for transmission through partially transparent plates,” *Sol. Energy*, vol. 15, no. 3, pp. 273–276, 1973, doi: 10.1016/0038-092X(73)90090-X.

[40] A. Calcabrini, H. Ziar, O. Isabella, and M. Zeman, “A simplified skyline-based method for estimating the annual solar energy potential in urban environments,” *Nat. Energy*, vol. 4, no. 3, pp. 206–215, Feb. 2019, doi: 10.1038/s41560-018-0318-6.

[41] R. Perez, R. Seals, and J. Michalsky, “All-weather model for sky luminance distribution—Preliminary configuration and validation,” *Sol. Energy*, vol. 50, no. 3, pp. 235–245, Mar. 1993, doi: 10.1016/0038-092X(93)90017-I.

[42] P. Ricchiazzi, S. Yang, C. Gautier, and D. Sowle, “SBDART: A Research and Teaching Software Tool for Plane-Parallel Radiative Transfer in the Earth’s Atmosphere,” *Bull. Am. Meteorol. Soc.*, vol. 79, no. 10, pp. 2101–2114, Oct. 1998, doi: 10.1175/1520-0477(1998)079<2101:SARATS>2.0.CO;2.

[43] W. Yang *et al.*, “Observation of the spectrally invariant properties of clouds in cloudy-to-clear transition zones during the MAGIC field campaign,” *Atmospheric Res.*, vol. 182, pp. 294–301, Dec. 2016, doi: 10.1016/j.atmosres.2016.08.004.

[44] G. Alexandri, A. K. Georgoulias, and D. Balis, “Effect of Aerosols, Tropospheric NO2 and Clouds on Surface Solar Radiation over the Eastern Mediterranean (Greece),” *Remote Sens.*, vol. 13, no. 13, p. 2587, Jul. 2021, doi: 10.3390/rs13132587.

[45] M. K. Fuentes, “A Simplified Thermal Model for Flat-Plate Photovoltaic Arrays,” 1987.

[46] W. E. McMahon, J. F. Geisz, J. Buencuerpo, and E. L. Warren, “A framework for comparing the energy production of photovoltaic modules using 2-, 3-, and 4-terminal tandem cells,” *Sustain. Energy Fuels*, vol. 7, no. 2, pp. 461–470, 2023, doi: 10.1039/D2SE01167K.

[47] W. McMahon *et al.*, “Homogenous Voltage-Matched Strings Using Three-Terminal Tandem Solar Cells: Fundamentals and End Losses,” *IEEE J. Photovolt.*, vol. 11, no. 4, pp. 1078–1086, Jul. 2021, doi: 10.1109/JPHOTOV.2021.3068325.

[48] H. Liu, C. D. Rodríguez-Gallegos, Z. Liu, T. Buonassisi, T. Reindl, and I. M. Peters, “A Worldwide Theoretical Comparison of Outdoor Potential for Various Silicon-Based Tandem Module Architecture,” *Cell Rep. Phys. Sci.*, vol. 1, no. 4, p. 100037, Apr. 2020, doi: 10.1016/j.xcrp.2020.100037.

[49] H. Schulte-Huxel, R. Witteck, S. Blankemeyer, and M. Köntges, “Optimal interconnection of three-terminal tandem solar cells,” *Prog. Photovolt. Res. Appl.*, vol. 31, no. 12, pp. 1350–1359, Dec. 2023, doi: 10.1002/pip.3643.

[50] R. Babajans *et al.*, “Impact of the Chaotic Synchronization’s Stability on the Performance of QCPSK Communication System,” *Electronics*, vol. 10, no. 6, p. 640, Mar. 2021, doi: 10.3390/electronics10060640.

[51] A. F. Rigosi *et al.*, “Atypical quantized resistances in millimeter-scale epitaxial graphene p-n junctions,” *Carbon*, vol. 154, pp. 230–237, Dec. 2019, doi: 10.1016/j.carbon.2019.08.002.

[52] A. Toprak, “Measurement and Simulation of Mosfet Device Parameters,” in *Proceedings of the 8th International conference on Research in Engineering, Science and Technology*, Acavent, Nov. 2018. doi: 10.33422/8rest.2018.11.38.

[53] B. Septian, Irwan, and Md. Misbahuddin, “Accuracy Improvement of Low-Cost GPS Receivers Using Decision Tree Algorithm,” in *2022 IEEE 8th International Conference on Smart Instrumentation, Measurement and Applications (ICSIMA)*, Melaka, Malaysia: IEEE, Sep. 2022, pp. 101–105. doi: 10.1109/ICSIMA55652.2022.9928953.

[54] D. N. Moriasi, J. G. Arnold, M. W. Van Liew, R. L. Bingner, R. D. Harmel, and T. L. Veith, “Model Evaluation Guidelines for Systematic Quantification of Accuracy in Watershed Simulations,” *Trans. ASABE*, vol. 50, no. 3, pp. 885–900, 2007, doi: 10.13031/2013.23153.

[55] “Meteonorm Version 8,” Meteonorm (de). Accessed: Aug. 14, 2024. [Online]. Available: https://meteonorm.com/meteonorm-version-8

[56] “IBC Solar Cells: Definition, Benefits, vs. Similar Techs,” Solar Magazine. Accessed: Aug. 18, 2024. [Online]. Available: https://solarmagazine.com/solar-panels/ibc-solar-cells/

[57] “How long do residential solar panels last?,” pv magazine International. Accessed: Aug. 19, 2024. [Online]. Available: https://www.pv-magazine.com/2024/07/23/how-long-do-residential-solar-panels-last-2/

[58] VDMA, “ITRPV 15th Edition.pdf.” VDMA, May 2024. [Online]. Available: https://www.vdma.org/international-technology-roadmap-photovoltaic

[59] “Global IBC Solar Cells Supply, Demand and Key Producers, 2024-2030--GlobalInfoResearch.” Accessed: Aug. 18, 2024. [Online]. Available: https://www.globalinforesearch.com/reports/894708/ibc-solar-cells

[60] “Solar cell prices fall for 3rd consecutive week,” pv magazine International. Accessed: Aug. 18, 2024. [Online]. Available: https://www.pv-magazine.com/2024/04/12/solar-cell-prices-fall-for-3rd-consecutive-week/

[61] J. T. Jacobo, “‘My belief is that IBC technology will win eventually,’ says Martin Green,” PV Tech. Accessed: Aug. 18, 2024. [Online]. Available: https://www.pv-tech.org/my-belief-is-that-ibc-technology-will-win-eventually-says-martin-green/

[62] S. R. Valluri, D. J. Jeffrey, and R. M. Corless, “Some applications of the Lambert W function to physics”.